

NORTHWESTERN UNIVERSITY

Fluorides and Oxyfluorides: Synthesis, Structural Characteristics, and Properties

A DISSERTATION

SUBMITTED TO THE GRADUATE SCHOOL
IN PARTIAL FULFILLMENT OF THE REQUIREMENTS

for the degree

DOCTOR OF PHILOSOPHY

Field of Chemistry

By

Jacqueline Renee Cantwell

EVANSTON, ILLINOIS

June 2018

© Copyright by Jacqueline Cantwell 2018

All Rights Reserved

Abstract

Fluorides and Oxyfluorides: Synthesis, Structural Characteristics, and Properties

Jacqueline Renee Cantwell

Noncentrosymmetry (NCS) is a requirement for many properties such as piezoelectricity, pyroelectricity, and nonlinear optical activity like second harmonic generation which are desirable for a variety of commercial applications. One method which has been employed to successfully synthesize NCS compounds utilizes acentric anionic groups, such as oxyfluoride metal complexes, as basic building units (BBUs) for a NCS structure. However, the presence of acentric BBUs in a structure is not always enough to ensure overall asymmetry; NCS packing is also required to achieve the desired properties.

The role of hydrogen bonding in the NCS packing of lambda-shaped dimers in $\text{CuVOF}_4(\text{H}_2\text{O})_7$ is explored. The difficulty of determining the hydrogen positions by x-ray diffraction has left many questions about the strengths and roles of hydrogen bonds in this structure. Previous work had emphasized the intra-dimer hydrogen bonding. A co-refinement of single crystal x-ray and neutron diffraction provided accurate hydrogen atom positions and hydrogen bonding distances, leading to a better understanding of how the hydrogen bonding interactions affect the structure.

$\text{CuMnF}_5(\text{H}_2\text{O})_7$ is a centrosymmetric structure composed of two different BBUs. A structural solution for this compound is presented for the first time. While it has similar BBUs to the centrosymmetric heterotypes of $\text{CuVOF}_4(\text{H}_2\text{O})_7$, the BBUs follow a different arrangement. The ionic octahedra are connected by a network of hydrogen bonding, but it is not enough to

create NCS packing. $\text{CuMnF}_5(\text{H}_2\text{O})_7$ exhibits strong pleochroism, changing from red to green when the direction of polarized light is changed. This property is also exhibited by KNaMnF_5 , a novel compound whose structure and properties are described, which changes from orange to red.

The NCS phase of KNaNbOF_5 is examined in a series of single crystal x-ray diffraction studies over a range of temperatures. Though the structure as a whole has positive thermal expansion, that is not necessarily true of all its constituent parts. The K–ligand bond lengths increase with rising temperature, as expected, but the Nb–ligand bond lengths show a slight decrease. These results are not conclusive but indicate a promising direction for future studies in this area.

Thesis Advisor, Kenneth R. Poeppelmeier

Acknowledgments

I started graduate school in September 2013 and in the five intervening years there have been many people who have helped me along the way. It would not be possible to express my gratitude to each and every individual who has made my path easier or more pleasant without consuming a disproportionate amount of space in this thesis. I hope that these words of thanks will suffice.

First and foremost I would like to thank my advisor, Ken Poeppelmeier. You have been an invaluable mentor throughout my project, and your support and advice on everything from writing grant proposals to teaching strategies to trouble-shooting experiments has been instrumental to my success. You have shaped not only my research but also who I am as a scientist, and I am grateful for your example.

The entire Poeppelmeier group deserves recognition for their contributions to my research, and I would like to highlight a few people in particular. Dr. Martin Donakowski, Dr. Kelvin Chang, Dr. Michael Holland, and Dr. Karl Rickert all trained me and introduced me to the world of oxyfluorides, hydrothermal chemistry, and crystal growth when I arrived, and for continuing to help me throughout my project through invaluable discussions. The other members of the oxyfluoride subgroup have also been helpful to my work: Jaye Harada, Matthew Nisbet, Chi Zhang, and Anita Chen. In addition, I want to thank Dr. Robert Kennedy, Dr. Dan Fowler, Dr. Michael Vermeer, Dr. Alex Dolgonos, Dr. Jared Incorvati, Dr. James McCarthy, Dr. Michael Yeung, Allison Wustrow, Ryan Paull, Justin Hancock, Steven Flynn, and Zachary Mansley. Thanks for being my labmates, for commiserating and trouble-shooting, for trivia, game nights, and cheap lunches, and most importantly for being my friends. To ships!

Special thanks to Tom Purcell; our weekly lunches over the past five years have kept me much saner than I would otherwise have ended up. Thanks for being there.

Many collaborators have been involved in this research. Dr. Huibo Cao of Oak Ridge National Laboratory was very helpful throughout the neutron diffraction experiment. Dr. Helge Rosner (IFW-Dresden) provided expertise with DFT which made it possible to look at $\text{CuVOF}_4(\text{H}_2\text{O})_7$ from another angle. Thank you to Emma Vander Ende and Dr. Richard Van Duyne for resurrecting an old set-up to measure optical absorption. Dr. Weiguo Zhang, Dr. Hongwei Yu, Dr. Hongping Wu, Dr. Shilie Pan, and Dr. P. Shiv Halasyamani provided the samples used in the rocking curve experiments. Thank you to Charlotte Stern, Dr. Amy Sarjeant, Dr. Christos Malliakas, and Jerry Carsello for endless help and advice with diffraction and crystallography questions.

Thank you to the many administrators who I have worked with during graduate school. To Ken's personal assistants, Mara Martini and Jake Thornberry, I hope you realize we are all grateful to you for keeping our little world running. It wouldn't be possible to overstate how important your work is. Jonathan Maendel, thank you for being an amazing graduate program assistant. Literally none of us would have anything turned in on time, or be registered for classes, without you. Similarly, thank you to Sam Ritchey for all the work you do as undergraduate program assistant. As a teaching assistant, you made my job easier, and I'm grateful. Thank you to everyone in the Chemistry Business Office for helping with purchase orders, randomly delayed payments, and reimbursements. You keep our department working and that is not a small job.

I would also like to thank my fiancé Nick Mahoney. Your support and love means the world to me and has kept me going through even the most difficult parts of graduate school. I can't wait to spend the rest of our lives together.

My parents, sister, and extended family have been my biggest cheerleaders throughout this process. You may not have understood everything I tried to tell you about, but you have been very good at smiling and nodding at the right moments. Your persistent desire to try to remember (if not understand) what I do is proof enough of your support.

I thank the National Science Foundation (DMR-1307698 and DMR-1608218) for funding this research. This work made use of the IMSERC at Northwestern University, which has received support from the Soft and Hybrid Nanotechnology Experimental (SHyNE) Resource (NSF ECCS-1542205); the State of Illinois and International Institute for Nanotechnology (IIN). Use of the J.B.Cohen X-Ray Diffraction Facility was supported by the MRSEC program of the National Science Foundation (DMR-1720139) at the Materials Research Center of Northwestern University and the Soft and Hybrid Nanotechnology Experimental (SHyNE) Resource (NSF ECCS-1542205). In addition, this work used resources at the High Flux Isotope Reactor, a DOE Office of Science User Facility operated by the Oak Ridge National Laboratory.

Table of Contents

List of Figures		12
List of Tables		16
Chapter 1	Introduction	17
1.1	Noncentrosymmetry	17
1.2	Oxyfluorides	21
1.3	Hydrogen Bonding	25
1.4	Hydrothermal Chemistry	31
1.5	Hydrofluoric acid and the precautions used	33
1.6	An overview of this work	35
Chapter 2	Hydrogen Bonding in $\text{CuVOF}_4(\text{H}_2\text{O})_7$	36
2.1	Abstract	36
2.2	Introduction	36
2.3	Experimental methods	39
2.3.1	Sample Preparation	39
2.3.2	Single crystal x-ray diffraction	40
2.3.3	Single crystal neutron diffraction	40
2.3.4	Co-refinement	41
2.3.5	Density Functional Theory	41
2.4	Results and Discussion	41
2.5	Conclusions	47

Chapter 3	Synthesis, Structure, and Pleochroism of $\text{CuMnF}_5(\text{H}_2\text{O})_7$	49
3.1	Abstract	49
3.2	Introduction	49
3.3	Experimental	50
3.3.1	Sample Preparation	50
3.3.2	Single crystal x-ray diffraction	51
3.3.3	Optical Absorption Measurements	51
3.4	Results and Discussion	52
3.5	Conclusions	59
Chapter 4	Crystal Structure and Properties of KNaMnF_5	60
4.1	Abstract	60
4.2	Introduction	60
4.3	Experimental	61
4.3.1	Sample preparation	61
4.3.2	Single crystallography	61
4.3.3	Optical absorption measurements	62
4.4	Results and Discussion	62
4.5	Conclusions	70

Chapter 5	Thermocrystallography of KNaNbOF_5	71
5.1	Introduction	71
5.1.1	Review of previous studies on KNaNbOF_5	71
5.1.2	Thermal Expansion	76
5.2	Experimental	78
5.2.1	Single crystal x-ray diffraction	78
5.2.2	Powder x-ray diffraction	78
5.3	Results and Discussion	78
5.4	Future Directions	91
5.5	Conclusions	92
Chapter 6	Rubidium Copper Chalcogenides	93
6.1	Source	93
6.2	Background	93
6.3	Experimental	96
6.3.1	Synthesis	96
6.3.2	Single crystal x-ray diffraction	97
6.4	Structures	98
6.5	Discussion	100
6.6	Summary	103

Chapter 7	Rocking Curves of Large Single Crystals	104
7.1	Preface	104
7.2	Introduction	104
7.3	Instrument Details	108
7.4	Instructions for rocking curve measurement	109
7.5	Results	111
7.6	Summary	116
Chapter 8	Conclusions	117
References		121
Appendix	Curriculum Vitae	136

List of Figures

Chapter 1

- Figure 1:** Graphical representation of the 21 acentric crystal classes and their relationships to the four symmetry-dependent NCS properties.....18
- Figure 2:** The V^{5+} bimetallic BBU is linear and centrosymmetric whereas the Nb^{5+} , Mo^{6+} bimetallic BBU is Λ -shaped owing to the out-of-center distortion. The smaller ions distort to more closely coordinate to nearby cations in the structure.....20
- Figure 3:** In a) all the dipoles are aligned, leading to a net polarity of the structure. In b) the dipoles are aligned against one another, but because the polar units are not the same, they do not completely cancel out, leading to a polar structure.....21
- Figure 4:** A comparison of the number of reported oxide and mixed-anion compounds in the Inorganic Crystal Structure Database (ICSD) as of 5 October 2017.....22
- Figure 5:** The three different primary distortions undergone by $[MO_xF_{6-x}]^{n-}$ ($x = 1, n = 2, M = V^{5+}, Nb^{5+}, Ta^{5+}; x = 2, n = 2, M = Mo^{6+}, W^{6+}; x = 3, n = 3, M = Mo^{6+}$) anions.....23
- Figure 6:** Neutron scattering lengths by element. Hydrogen has a scattering length of -3.739 fm, whereas vanadium, a much larger atom, has a scattering length of -0.3824 fm.....29
- Figure 7:** The solid reagents and desired solvent are placed in pouches made of Teflon film. Up to six pouches can be placed in single autoclave. Following the heating of the vessel, the pouches are removed and the crystals are separated using vacuum filtration.33

Chapter 2

- Figure 1:** $CuVOF_4(H_2O)_7$ unit cell as viewed along the c axis. The structure is composed of bent dimers whose shape favors noncentrosymmetrical packing.37
- Figure 2:** The structures with the hydrogen atoms determined by x-ray and by co-refinement with neutron diffraction data are shown above. Below is a comparison of the key hydrogen bonding distances.43
- Figure 3:** The dimer is shown with an overlay of the hydrogen atoms from each of the three methods of determination; the light blue are from the co-refined structure, the light green are from the x-ray only structure, and the bright red are from the DFT determination. Hydrogen bonding interactions are not shown for simplicity.44

Chapter 3

- Figure 1:** Unit cell of $\text{CuMnF}_5(\text{H}_2\text{O})_7$. The octahedral ionic units are in offset rows, alternating in an *aabb* pattern.52
- Figure 2:** The octahedral BBUs of $\text{CuMnF}_5(\text{H}_2\text{O})_7$ are arranged in alternating double lines, though they are not connected into chains.....53
- Figure 3:** Illustration of $[\text{Cu}(\text{H}_2\text{O})_7]^{2+}$ and $[\text{MnF}_5(\text{H}_2\text{O})]^{2-}$ ions. In conjunction with the bond distances in Table 2, it can be seen that both octahedra exhibit a Jahn Teller distortion.54
- Figure 4:** Comparison of the structures of $\text{CoAlF}_5(\text{H}_2\text{O})_7$, $\text{CuMnF}_5(\text{H}_2\text{O})_7$, $\text{CoVOF}_4(\text{H}_2\text{O})_7$, and $\text{CuVOF}_4(\text{H}_2\text{O})_7$. $\text{CuMnF}_5(\text{H}_2\text{O})_7$ was originally thought to be a related structure to $\text{CoAlF}_5(\text{H}_2\text{O})_7$ but it is actually more similar to a version of the $\text{CuVOF}_4(\text{H}_2\text{O})_7$ without the bridging oxygen. The heterotypic $\text{CoVOF}_4(\text{H}_2\text{O})_7$ is a better match for the $\text{CoAlF}_5(\text{H}_2\text{O})_7$ structure.....57
- Figure 5:** Pictures of $\text{CuMnF}_5(\text{H}_2\text{O})_7$ crystals under a polarized light source. When the light is rotated 90° the color changes from red to green (or vice versa).....58
- Figure 6:** Absorbance spectrum of the $\text{CuMnF}_5(\text{H}_2\text{O})_7$ (0 $\bar{1}$ 0) face. Two separate absorption peaks are visible, alternating with every 90° of polarization. This matches well with the visible color change.....58

Chapter 4

- Figure 1:** Structure of KNaMnF_5 shown down the b axis. Chains of $[\text{MnF}_6]^{2-}$ octahedra run along the a axis and are separated by K and Na cations.....64
- Figure 2:** Crystal structure of KNaMnF_5 along the a axis (top) and c axis (bottom). The pictures illustrate the nature of the packing of the manganese fluoride chains. The chains pack together such that the octahedra are offset from their nearest neighbors.....65
- Figure 3:** Manganese fluoride octahedra are connected by vertices in chains. The octahedra exhibit the Jahn Teller distortion that is typical of Mn^{III} complexes.....66
- Figure 4:** KNaMnF_5 crystal at 8x magnification. The crystal changes from red (left) to orange (right) when a polarized light is rotated.....67
- Figure 5:** Absorbance spectrum of KNaMnF_5 (001) face. The polarization is linear, and the rotation of colors is seen by the change in absorbance every 90°68

Figure 6: Absorbance spectrum of the KNaMnF_5 ($\bar{1}00$) face. The (001) and ($\bar{1}00$) show similar spectra, indicating that the pleochroism does not greatly differ between these two faces.68

Figure 7: Absorbance spectrum of the KNaMnF_5 (010) face. The absorbance peaks are aligned here, rather than offset. This may imply an overlap of the optical activity, another optical axis entirely, or there may be other effects of the crystal on the absorbance.....69

Chapter 5

Figure 1: The structure of the NCS polymorph of KNaNbOF_5 is composed of layers of $[\text{NaNbOF}_7]_\infty$ which stack to form channels that run parallel to the c axis. K^+ ions are located in these channels. Figure adapted from reference72

Figure 2: The CS polymorph of KNaNbOF_5 is a rock salt double perovskite. The Na and Nb atoms occupy the B-sites in distorted octahedra. The A-site alternates between layers of K^+ cations and vacancies, which results in the ordering of the oxide and fluoride positions. Figure adapted from reference.....74

Figure 3: The lattice constants are graphed against temperature. Measurements of the unit cells were made using both single crystal (SCXRD) and powder (PXRD) diffraction techniques. The b and c lattice constants show upward trends, but a is inconclusive. All three show much greater variation than expected.....82

Figure 4: Comparison of lattice parameters measured using single crystal and powder x-ray diffraction (SCXRD and PXRD respectively).....83

Figure 5: Unit cell volume (from the SCXRD measurements) is graphed against temperature. An upward trend is seen, though with large variation.....84

Figure 6: Shifts in atomic position in the ab plane. are shown through the change in the x and y values for each data set compared to those of the 110K data (adjusted to account for changes in lattice size). Because there is no crystallographic zero in the z direction, shifts in z are much less reliable and are not compared. The data has been mirrored across all four quadrants so as to better compare the trends.....86

Figure 7: Selected potassium-anion distances as a function of temperature. The positive trends of the data show that these bonds experience PTE.....88

Figure 8: The changes in Niobium – ligand bond length as a function of temperature. In all cases there is a negative slope, indicating NTE for the $[\text{NbOF}_5]$ unit, in spite of the PTE of the structure as a whole.....89

Chapter 6

- Figure 1.** Pie chart illustrating the proportion of 8-electron ABX compounds that are known, unknown and unstable, and unknown and stable. Approximately 30% of the unknown compounds were predicted to have stable structures.....95
- Figure 2.** A chart of selected I-I-VI ABX compounds and the results of the theoretical modeling. Checkmarks denote compounds already documented in the literature.....96
- Figure 3.** Experimental structure of RbCuS.....98
- Figure 4.** Experimental structure of RbCuSe.....98
- Figure 5.** The structure of RbCuTe. There are double chains rather than the single chains seen in the S and Se compounds. The chains are also not parallel but are alternately perpendicular to each other.....102

Chapter 7

- Figure 1** Mosaic model of a crystal. The tilting of the mosaic domains is exaggerated for clarity.....105
- Figure 2:** Schematic of rocking curve measurement.....106
- Figure 3:** Diagram of ATX-G optical system.....108
- Figure 4** Rocking curves of large single crystal NLO materials with FWHMs labelled.....112
- Figure 5:** Rocking curve of Si(111) crystal.....115

List of Tables

Chapter 2

Table 1: Crystallographic data 42

Table 2: Selected O-H Bond Lengths 46

Chapter 3

Table 1: Crystallographic information of $\text{CuMnF}_5(\text{H}_2\text{O})_7$ 53

Table 2: Selected Bond Distances 55

Table 3: Selected Bond Angles 55

Chapter 4

Table 1: Crystallographic information for KNaMnF_5 63

Table 2: Selected bond distances and angles 67

Chapter 5

Table 1: Refinement Parameters of the Single Crystal Data Sets 79

Chapter 6

Table 1: Crystallographic information for RbCuS and RbCuSe 99

Table 2: Copper-chalcogen bond distances and angles 100

Chapter 7

Table 1: Rocking curve measurements: comparison of NLO samples 114

Chapter 1: Introduction

1.1 Noncentrosymmetry

Designing crystal structures that have specific physical properties remains an elusive but tantalizing goal. Ideally, an engineer would simply give a chemist a list of the properties desired for a particular application and receive in return a short time later an easily scalable, optimized synthetic procedure for a cheap, non-toxic chemical matching the given description. Inorganic chemistry has not yet progressed to such a point. The relationships between structural characteristics and physical properties are still being investigated and studied. The toolbox of crystal design is growing however, and it has a few established cornerstones on which to build. Noncentrosymmetry is one such structural characteristic.

Noncentrosymmetric (NCS) compounds are those whose structure lacks a center of symmetry or inversion center. NCS is a requirement for the properties of enantiomorphism, circular dichroism, piezoelectricity, and pyroelectricity, all of which are highly sought after for commercial applications.¹ Of the 32 crystal classes, 21 are NCS; despite this, NCS materials are far less common than centrosymmetric ones.² The 21 acentric (noncentrosymmetric) crystal classes and their relationships to the NCS properties are shown in Figure 1. Nonlinear optical (NLO) activity, such as second harmonic generation (SHG), shares the same symmetry requirements as piezoelectricity. SHG, also known as frequency doubling, has garnered particular interest for its use in controlling laser frequencies, with applications in spectroscopy, optical communications, and many other technologies. SHG occurs when an incident light wave in a noncentrosymmetric material produces a nonlinear polarization wave, which has a frequency

double that of the original light wave.³ Phase matching occurs when there is constructive interference between the electric field of the light and the induced polarization of the electric charges within the material.³ Phase matchability is necessary for an SHG material to be efficient, as non-phase matchable materials show an inverse relationship between SHG efficiency and crystal size.⁴

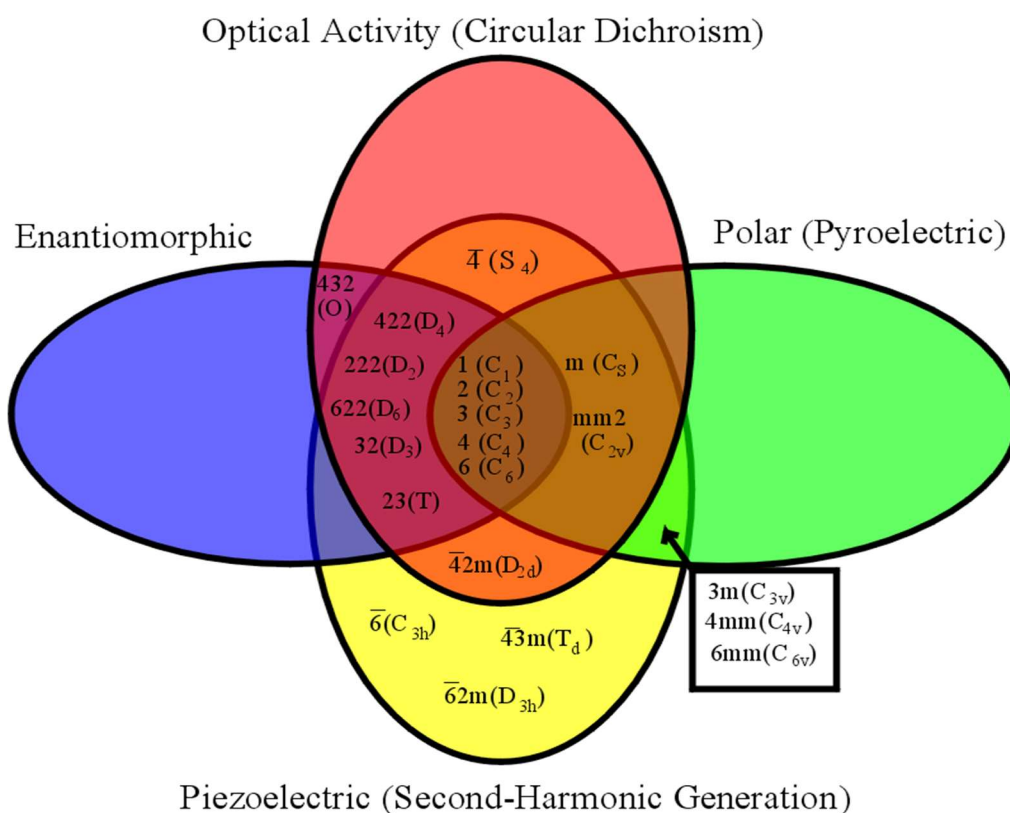


Figure 1. Graphical representation of the 21 acentric crystal classes and their relationships to the four symmetry-dependent NCS properties.¹

Chen's anionic group theory is a methodology for evaluating the spatial arrangement of anionic groups within a crystal lattice for its potential SHG efficiency.⁵ It provides structural

criteria, tested on a survey of nonlinear optical materials, by which it has found that frequently in high-performance NLO materials the polar moments of the anionic units are fully aligned.⁵ The search for optimal NLO and SHG materials then begins with finding ways to make basic building units (BBUs) that are favored by Chen's anionic group theory; these BBUs may be molecular or ionic species within the structure depending on the compound. Early transition metal oxyfluoride anions are good candidates for NCS BBUs because they satisfy the precepts of Chen's anionic group theory.

Multiple types of distortions can affect the structure; one of which is the 'out-of-center-distortion. Disparity between an ion's radius and the volume of its site causes a spontaneous distortion in the structure. An ion occupying a site too large for its size will undergo an out-of-center distortion in order to be in closer coordination to nearby counter-ions. Li^+ ions exhibit this distortion in LiNbO_3 , which contributes to the material's polarity.⁶ This is also seen in the series of compounds $\text{K}_{10}(\text{M}_2\text{O}_n\text{F}_{11-n})_3\text{X}$ ($\text{M} = \text{V}^{5+}$, Nb^{5+} , $n = 2$; $\text{M} = \text{Mo}^{6+}$, $n = 4$; $\text{X} = (\text{F}_2\text{Cl})_{1/3}$, Cl , Br , $([\text{Br}_3][\text{Br}])_{1/2}$, and $([\text{I}_3][\text{I}])_{1/2}$).⁷ As seen in Figure 2, the larger V^{5+} ions "fit" well in the site, the bimetallic BBU is linear, and the structure is centrosymmetric. The larger Nb^{5+} and Mo^{6+} cations have a greater disparity between their radius and the volume of the occupied site, leading to an out-of-center distortion. This breaks the inversion symmetry and creates a NCS structure.

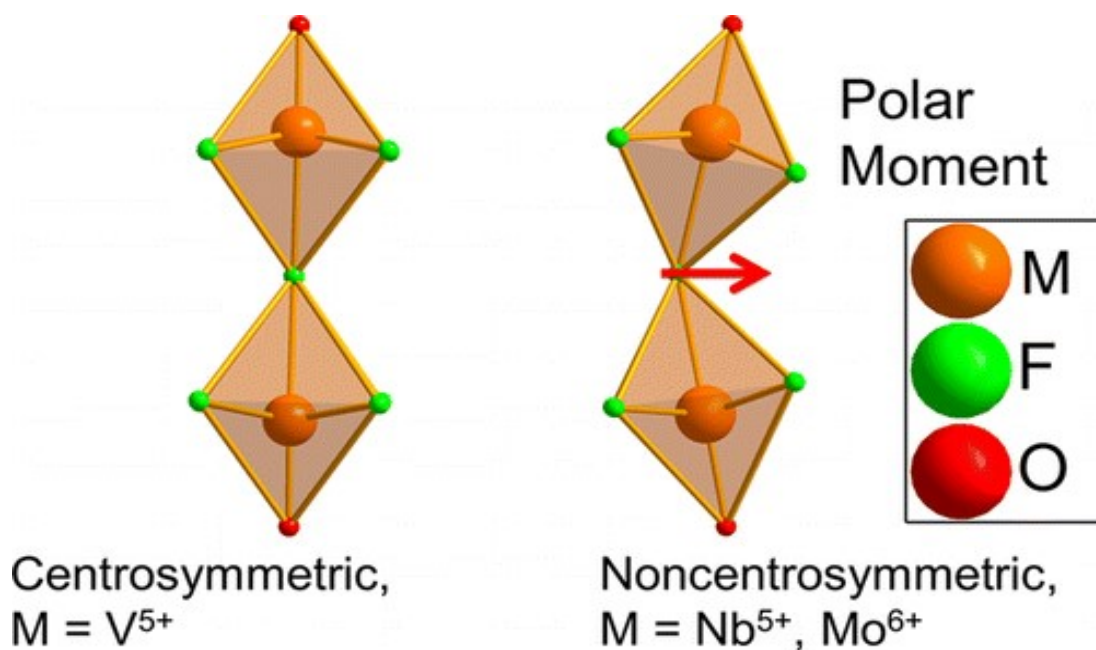


Figure 2. The V⁵⁺ bimetallic BBU is linear and centrosymmetric whereas the Nb⁵⁺, Mo⁶⁺ bimetallic BBU is Λ -shaped owing to the out-of-center distortion. The smaller ions distort to more closely coordinate to nearby cations in the structure.^{a6}

It should be noted that acentric units do not always lead to NCS structures. The structure of MVOF₄(H₂O)₇ (M = Co, Ni, Zn) is composed of [M(H₂O)₆]²⁺ cations and [VOF₄(H₂O)]²⁻ anions, and while the anionic groups are acentric, the structures as a whole are centrosymmetric.⁸ The ions form a distorted CsCl type structure in which the [VOF₄(H₂O)]²⁻ are organized into antiparallel chains connected by hydrogen bond networks. This antiparallel alignment cancels out the polar moments of the acentric anions resulting in no net polarity. Polar anions do not necessarily ensure overall polar symmetry, but they do increase the likelihood of forming a polar structure, compared to nonpolar units.⁹⁻¹¹ The presence of two different polar units still further increases the probability of producing a crystal with net polarity. In a structure with one type of polar unit, the dipoles are either aligned together, aligned such that they cancel each other out, or they are not aligned at all. Only when they are aligned together is there a net dipole moment. If

there is more than one type of polar unit, there is an additional possibility: the dipoles may be aligned such that the destructive interference of the two dipole moments does not completely cancel out. An illustration of this is shown in Figure 3.

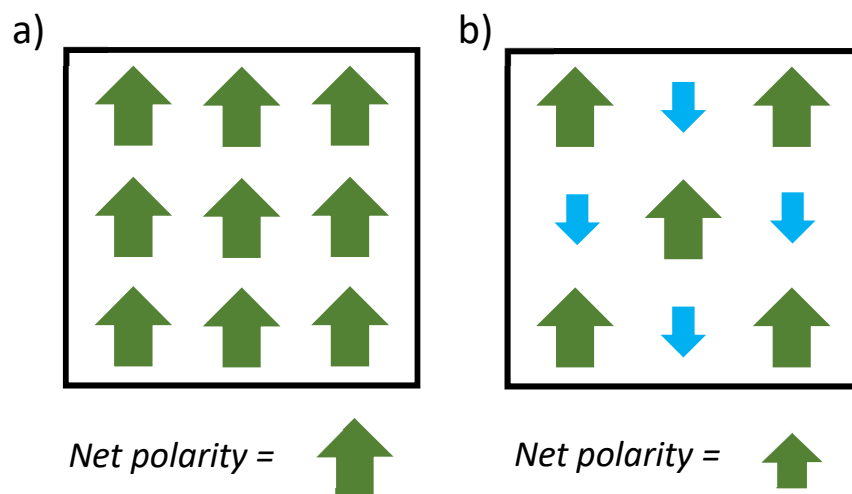


Figure 3. In a) all the dipoles are aligned, leading to a net polarity of the structure. In b) the dipoles are aligned against one another, but because the polar units are not the same, they do not completely cancel out, leading to a polar structure.

1.2 Oxyfluorides

Mixed-anion compounds are solid state materials with more than one anionic species in a single phase. Most of the known mixed-anion compounds are oxide based, such as oxyfluorides, oxynitrides, and oxychalcogenides, but pnictohalides and pnictochalcogenides have also been reported.¹²⁻¹⁵ Oxides are much more common than multi-anion materials, both in nature and in synthesis, which has allowed a vast knowledge base to develop on their structures and properties that is lacking for the oxyfluorides, for now. Figure 4 shows a comparison of the relative

frequency of oxide compounds and multi-anion compounds reported in the Inorganic Crystal Structure Database (ICSD); for reference at the same time of retrieval there were 2978 fluorides reported.¹² Oxides are overwhelmingly dominant in the literature, thanks to research that may soon pass from merely extensive to positively exhaustive.

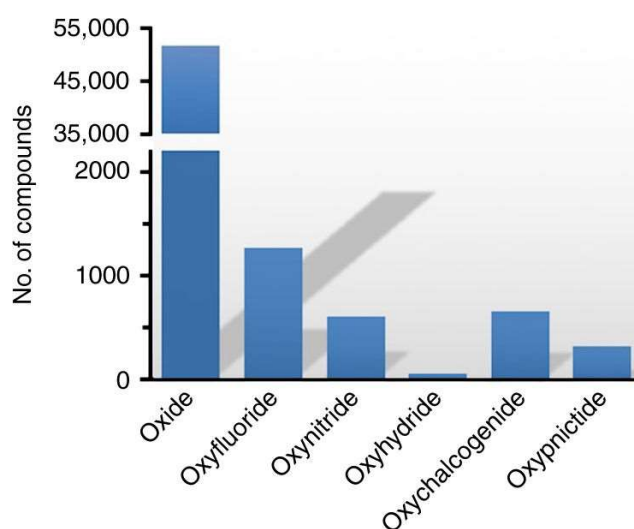


Figure 4. A comparison of the number of reported oxide and mixed-anion compounds in the Inorganic Crystal Structure Database (ICSD) as of 5 October 2017.¹²

Beyond offering the potential of a largely unexplored phase space, mixed-anion materials have structural differences from single-anion compounds that change the possible physical properties. As previously discussed, acentric BBUs are key to making NCS structures. A mixture of oxide and fluoride ligands around a metal center can break the local symmetry of the anion. Inherent differences between metal-oxide and metal-fluoride bonds as well as electrostatic interactions between the anions and the extended structure lead to distortions of the metal ion

polyhedra. While the extended structure interactions do not usually result in large distortions on their own, they do contribute to the ordering of the structure. The stronger distortion is the second-order Jahn-Teller distortion. This distortion is caused by the mixing of the valence d orbital of the early transition metal cation and the $2p$ valence orbitals of the oxide and fluoride ligands, which results in an electronic configuration with degenerate states. The degeneracy is removed by a spontaneous distortion. In early transition metal octahedra of the formula $[\text{MO}_x\text{F}_{6-x}]^{2-}$, the transition metal d orbitals mix more strongly with the $2p$ orbitals of the oxide ligands than those of the fluoride ligands, because the fluoride valence orbitals are much lower in energy. Figure 5 illustrates how the number of oxygen atoms in the anionic unit affects the resulting distortion. Depending on whether there are one, two, or three oxide ligands, the metal atom will distort towards a vertex, edge, or face of the octahedron, respectively.⁸ Mixed oxide-fluoride anionic octahedra are therefore very good acentric BBUs.

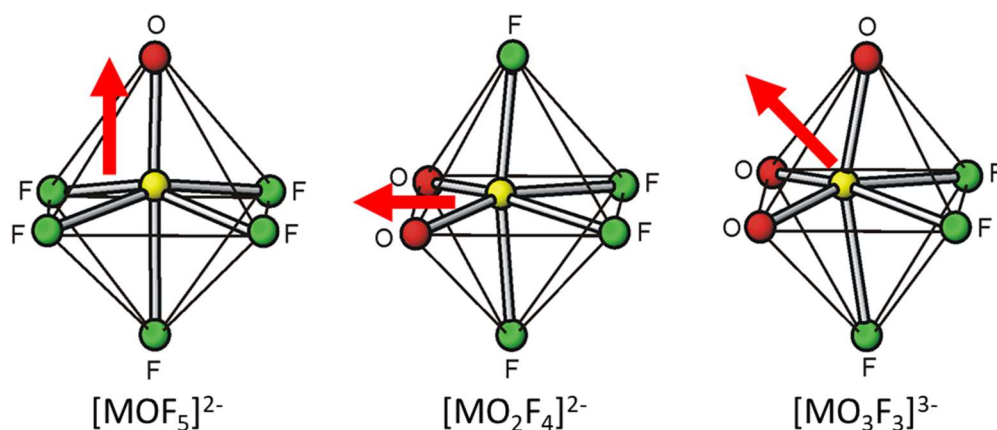


Figure 5. The three different primary distortions undergone by $[\text{MO}_x\text{F}_{6-x}]^{n-}$ ($x = 1, n = 2, \text{M} = \text{V}^{5+}, \text{Nb}^{5+}, \text{Ta}^{5+}$; $x = 2, n = 2, \text{M} = \text{Mo}^{6+}, \text{W}^{6+}$; $x = 3, n = 3, \text{M} = \text{Mo}^{6+}$) anions.⁹

It is important to point out at this point that not all mixed-anion compounds contain transition metal BBUs with heteroleptic coordination geometry. Heteroleptic complexes are those in which the ligands coordinated to the metal differ, whereas homoleptic complexes contain only one kind of ligand. Many structures have layers or BBUs of different homoleptic coordination complexes. For example, $\text{Sr}_2\text{MnO}_2\text{Cu}_{1.5}\text{S}_2$ has alternating layers of Sr_2MnO_2 and $\text{Cu}_{1.5}\text{S}_2$.¹⁶ Just as acentric BBUs are no guarantee of a NCS structure, mixed-anions do not necessarily lead to acentric heteroleptic BBUs.

The synthesis of ordered oxyfluoride materials is particularly significant as disorder of the oxide and fluoride ligands cancels out the desirable physical properties associated with the out-of-center distortions and NLO susceptibilities. Historically this has been a challenge. Some of the strategies that have been successfully employed to avoid disordered oxygen/fluorine sites include using helical compounds, forming bent or Λ -shaped BBUs, and having two distinct polar anions in the compound.^{8,17,18} Hard and Soft Acids and Bases (HSAB) chemistry also works in favor of ordered NCS oxyfluorides. HSAB theory was first described by R. G. Pearson.¹⁹ Hard anions bond more strongly with hard cations, and soft anions bond more strongly with soft cations.²⁰ Hardness and softness are correlated with the Z_{eff} of an ion, and therefore its electronegativity. Fluoride is harder than oxide, which means that when an oxyfluoride BBU has more than one type of cation in its coordination environment, hard-soft interactions can lead to ordering of the oxide and fluoride ligands. This effect is more pronounced on structures synthesized from solution than from solid state methods.¹⁹ $\text{AgNa}(\text{VO}_2\text{F}_2)_2$ (SSVOF) is a double-wolframite structure which exhibits ordering caused by HSAB interactions.²¹ SSVOF contains layers of interconnected vanadium oxyfluoride octahedra which are alternately separated by

silver and sodium cations. The softer oxide ligands preferentially coordinate with the softer silver cations whereas the harder fluoride ligands preferentially coordinate with the harder sodium cations.

Determining whether an oxyfluoride structure is disordered can present its own challenges. Because oxygen and fluorine have such similar sizes, disordered site occupancy is not uncommon. For the same reason their x-ray scattering lengths are very similar, and identifying oxide ligands versus fluoride ligands in the structure based solely on x-ray contrast may or may not be feasible depending on the structure. It is possible for many cases, especially given the continuing improvements to x-ray diffraction instruments, when there are not heavy metals in the structure. In such cases where heavy metals make distinguishing the oxygen and fluorine atoms impossible by x-ray refinement, neutron diffraction may be useful. First and second row transition metals are not generally heavy enough to pose a problem for identifying oxygen vs. fluorine, so for a majority of inorganic structures x-ray diffraction is all that is necessary. Furthermore, evidence of ordered sites can be seen in distinct bond lengths or in differing coordination environments. Of course, many structures contain a mixture of ordered and occupancy-disordered sites, and even among disordered sites, the probability of one anion ligand over another occupying the site may vary.

1.3 Hydrogen Bonding

Hydrogen forms bonds easily with anions, but the discussion of a “hydrogen bond” often refers to an entirely separate phenomenon. Hydrogen bonding was first described in 1920 by Latimer and Rodebush.²² While many definitions have since been used, the one provided by

Hamilton and Ibers is simple and practical: “a hydrogen bond exists when a hydrogen atom is bonded to two or more other atoms”.²³ To put it another way, hydrogen bonding occurs when a hydrogen bonded to one atom forms another bond with a nearby anion. Hydrogen bonding is weaker than covalent bonding (and considerably weaker than ionic bonding), but stronger than van der Waals forces. Defining a cut-off line of bond distance for hydrogen bonding seems rather like trying to define, based on size or orbit, which objects in the solar system should be considered planets: rife with exceptions. It is more useful to focus on the chemical requirements of the hydrogen bond. The hydrogen atom needs to be attached to an electronegative donor atom which withdraws electrons making the hydrogen atom acidic. A nearby acceptor atom with a high electron density interacts strongly with the acidic hydrogen forming a “hydrogen bond”.²³ Fluorine, oxygen, and nitrogen are all common donor atoms due to their high electronegativity. The second row elements of these groups can also be involved in hydrogen bonding, but these hydrogen bonds are much weaker.²³ Hydrocarbon cations can also be donor groups, but carbon rarely acts as an acceptor (though there are of course exceptions²⁴). Nitrogen, oxygen, and fluorine are all good acceptors, along with the halogen ions.

Hydrogen bonding has been shown many times over to be central to the formation and stabilization of chemical structures. From an organic perspective, the known geometries of N–H...O hydrogen bonds led to Franklin, Watson, and Crick’s understanding of the structure of DNA.²³ In addition, hydrogen bonds are enormously important to the structures of amino acids and proteins. Hydrogen bonding also plays a vital role in inorganic structures, particularly hydrates. Oxygen’s ability to act as both a donor and acceptor atom in hydrogen bonding means that any compound containing water, either as a ligand or as a free molecule, possesses the

potential for hydrogen bonding to impact the structure. In oxyfluoride structures this is especially true as the structure may contain multiple possible acceptor ligands for hydrogen bonds. This will be explored in more detail when discussing the structure of $\text{CuVOF}_4(\text{H}_2\text{O})_7$, but it will suffice to say for now that hydrogen bonding is capable of stabilizing acentric BBUs. These effects are important to understand if they can be used to guide the materials discovery process.

Determining the positions of hydrogen atoms in the structure has traditionally presented a challenge to crystallographers owing to hydrogen's weak x-ray scattering. X-ray diffraction depends on the electron cloud of an atom scattering the x-rays. In a cloud of one, the scattering is weak by definition. In compounds consisting only of lighter elements, such as organic materials, hydrogen atoms can be seen against the background. However, once heavier elements like metals are introduced, the hydrogen atoms are effectively masked by the bigger peaks of the larger atoms. In some cases, the hydrogen atoms are geometrically constrained so that their positions are easily determined and their bond lengths inferred based on decades' of measurements. However, in other cases, such as the $\text{CuVOF}_4(\text{H}_2\text{O})_7$ structure that will be explored in depth in this thesis, the hydrogens have greater freedom of motion and cannot be found merely by using steric considerations. Even among structures where x-ray diffraction is insufficient to accurately determine the positions of hydrogen atoms, it is often not a concern for the structure as a whole and so the hydrogens are approximated using crystallography software.

Recently in *Chemical and Engineering News*, Hodgkinson and Widdifield posed the question, "How reliable are the structures deposited in crystallographic databases?"²⁵ It is not shocking to consider that there are probably structures with errors, but how many has been a question lurking in the shadows of the databases. In a survey of the Cambridge Structure

Database (CSD), they found that among repeat structures, the non-hydrogen atom positions are very consistent whereas the hydrogen atoms often showed structural differences.²⁵ In most cases, these differences were easily resolved by DFT or were chemically uninteresting. 1% of cases did not have differences that could be optimized away by DFT. These cases are, perhaps unsurprisingly, those where the hydrogens are involved in hydrogen bonding.

As noted earlier, hydrogen bonding plays an important role in many structures.

Therefore, determining the positions of hydrogens within the structure takes on a special interest beyond mere thoroughness. The most common methods for solving this problem are x-ray and neutron diffraction. Though the obstacles to using x-ray diffraction have already been discussed, it has, and probably will, remain the most widely used crystallography method owing to the ease of access to high quality instruments and relatively low cost. Where x-ray diffraction involves the scattering of particles by the electron cloud, electron diffraction can be thought of as the scattering of electrons by the electrostatic potential of an atom.²³ Because of this, electron diffraction scattering amplitudes follow similar trends to x-ray diffraction. Thus, electron diffraction offers no real benefit for the determination of hydrogen positions. The neutron beam, however, is mainly scattered by the atomic nucleus, and unlike x-ray or electron diffraction the scattering length does not increase linearly with atomic number.²³ Figure 6 shows the periodic table with the neutron scattering lengths of each element.²⁶ Hydrogen has an average scattering length, whereas vanadium which is much larger is one of the weakest neutron scatterers.

Vanadium is often used as a container for neutron diffraction experiments for this reason. The sign of the amplitude is merely used to convey whether the scattered wave is in or out of phase with the incident beam. A positive sign indicates that the scattered wave is 180° out of phase,

whereas a negative sign indicates that the scattered and incident waves are in phase.²³ Because neutron diffraction can easily identify hydrogen atoms in the structure, it has long been the gold standard for their placement. The great disadvantage of neutron diffraction is that it requires the use of large national or international neutron source facilities, which is both inconvenient and costly.

Neutron coherent scattering lengths

Bound coherent scattering length, unit: fm

H																				He	
-3.739																					3.26
Li	Be											B	C	N	O	F	Ne				
-1.9	7.79											5.3	6.646	9.36	5.803	5.654	4.566				
Na	Mg											Al	Si	P	S	Cl	Ar				
3.63	5.375											3.449	4.1491	5.13	2.847	9.577	1.909				
K	Ca	Sc	Ti	V	Cr	Mn	Fe	Co	Ni	Cu	Zn	Ga	Ge	As	Se	Br	Kr				
3.67	4.7	12.29	-3.438	-0.3824	3.635	-3.73	9.45	2.49	10.3	7.718	5.68	7.288	8.185	6.58	7.97	6.795	7.81				
Rb	Sr	Y	Zr	Nb	Mo	Tc	Ru	Rh	Pd	Ag	Cd	In	Sn	Sb	Te	I	Xe				
7.09	7.02	7.75	7.16	7.054	6.715	--	7.03	5.88	5.91	5.922	4.87	4.065	6.225	5.57	5.8	5.28	4.92				
Cs	Ba		Hf	Ta	W	Re	Os	Ir	Pt	Au	Hg	Tl	Pb	Bi	Po	At	Rn				
5.42	5.07		7.7	6.91	4.86	9.2	10.7	10.6	9.6	7.63	12.692	8.776	9.405	8.532	--	--	--				
Fr	Ra																				
--	--																				
		La	Ce	Pr	Nd	Pm	Sm	Eu	Gd	Tb	Dy	Ho	Er	Tm	Yb	Lu					
		8.24	4.84	4.58	7.69	--	0.8	7.22	6.5	7.38	16.9	8.01	7.79	7.07	12.43	7.21					
		Ac	Th	Pa	U	Np	Pu	Am	Cm												
		--	10.31	--	8.417	--	--	--	--												

Figure 6. Neutron scattering lengths by element. Hydrogen has a scattering length of -3.739 fm, whereas vanadium, a much larger atom, has a scattering length of -0.3824 fm.²⁶

Other techniques for hydrogen atom placement have also recently gained momentum.

Nuclear magnetic resonance (NMR) crystallography has developed out of improvements to solid-state NMR and density functional theory (DFT).²⁵ Fast sample spinning to obtain ^1H NMR

spectra has allowed researchers to distinguish between two structures which differed by only a single hydrogen of a hydroxide group.²⁵ DFT itself has also shown potential as a means of placing hydrogen atoms within a structure, either as a way of verifying empirical results or even independently.^{27,28}

Recently, Woinska et al reported on the use of Hirshfeld atom refinement (HAR) to determine hydrogen atom positions using only x-ray crystallography.²⁹ While their title “Hydrogen atoms can be located accurately and precisely by x-ray crystallography” is technically not at fault, it is both an over-promising description of HAR’s abilities and an injustice to the literature of hydrogen atom crystallography. As already pointed out, the location of hydrogen atoms using x-rays has been possible for some time – provided a few caveats. For a small organic molecule containing no heavier metals, in which all the hydrogen atoms positions are geometrically constrained to specific angles, it is often easy to identify and freely refine hydrogen atoms within the structure. Obviously, quite a large portion of structures are inorganic and contain metallic atoms, and therein lies the difficulty. If the hydrogens have any freedom of motion at all, geometry alone will not be able to determine their spatial location, which is not improved by the HAR. Hydrogen bond lengths are well known and documented, and crystallography software generally draws on databases to assign bond distances for hydrogen atoms. HAR does show closer bond distances to neutron diffraction lengths than does x-ray diffraction; however, it does not address the unreliability of the hydrogen atoms’ positions within the structure.²⁹ In addition, the authors themselves admit that the HAR method is only possible for small molecules, not extended networks, disordered structures, or molecular biology. While HAR has some promise for the future as a supplement to current crystallography software,

without more fully addressing the hydrogen atoms' spatial positions, it will be unlikely to see broader use in the immediate future.

1.4 Hydrothermal Chemistry

Hydrothermal chemistry is the primary means of synthesis throughout this thesis. Solvothermal synthesis is a synthetic method in which the reaction occurs in solution inside a sealed vessel at temperature near the solution's boiling point and at pressures above atmospheric pressure.³⁰ Hydrothermal synthesis is simply solvothermal synthesis in which the solvent is water. The reactants undergo liquid-phase transport which allows for rapid nucleation and then growth of single crystal products. Compared to traditional solid state reactions, the "heat and beat" method, which often require temperatures in the range of 700 °C to 1700 °C (or more), hydrothermal is a relatively mild synthetic method. It also requires much less time, on the order of days rather than weeks. Particularly helpful for research of oxyfluoride compounds, hydrothermal synthesis increases the likelihood of forming mixed-anion phases which are frequently disfavored at higher temperatures where other phases dominate.¹² Additionally, the differing volatilities of oxides and fluorides is an obstacle to making oxyfluoride compounds through traditional solid state methods.¹² Hydrothermal synthesis also has a strong history of producing NCS compounds.³¹

The following is an outline of the synthetic method used throughout this thesis, with greater detail than is typically given in a paper, in the hopes that it may clarify the process. A schematic of the process is shown in Figure 7. Each reaction is placed inside a pouch of fluorinated ethylene propylene (FEP) Teflon film, following a method adapted from that of the

Stucky group.³² To produce these pouches, we use .005" FEP Type A Teflon from DuPont, folded and sealed on two edges using a pedal-operated double heat sealer from Packco Inc (model MP-12DS). After the solid reagents and desired solvent (hydrofluoric acid and/or water) have been added to the pouch, it is sealed on the third side, closing it. Up to six of these pouches can be placed into a single 125 mL polytetrafluoroethylene (PTFE) Teflon liner. Deionized water (approximately 40-50 mL) is added to the liner as a backfill.

It should be noted that the Teflon pouches are semi-permeable to water and solvents such as hydrofluoric acid, though not to solid reagents or larger ions/molecules. Thus, reactions involving different metal oxides may be run together, but any experiments involving differing acidity should be done in separate autoclaves. The liner itself is mainly chemically inert, though over time, hydrofluoric acid will leech into the liner, as will some heavy metals. For this reason, reactions involving either of these should be limited to liners dedicated for the purpose to reduce the safety hazard to others.

Once filled, the liner is capped and placed into the autoclave. The "autoclaves" used are Parr Acid Digestion Vessels (4748 Large Capacity). Detailed information about the safe use of the liners and autoclaves is available in the manual published by the manufacturer.³⁶ The FEP Teflon pouches will melt at 260 °C, providing one practical limit to temperature, but the PTFE Teflon liners will also begin to distort at these temperatures. The autoclaves themselves are also not recommended for use above 250 °C.³⁶ Pressure in the autoclaves, the key to hydrothermal synthesis, is generated autogenously from the water vapor produced on heating. The autoclaves can handle pressures up to 1900 psig, but using water at the above temperatures will only reach 576 psig.³⁶

The autoclaves are heated in traditional box furnaces, usually dwelling at peak temperature (typically between 150 °C and 250 °C) for 24 to 48 hours before cooling. Slow cooling is often used to aid the crystallization process. In addition, the pouches are frequently left to sit undisturbed for 48 more hours so as to not interrupt the crystallization process. This has often lead to visibly larger crystals. For some compounds, such as $\text{CuVOF}_4(\text{H}_2\text{O})_7$, this step is vital to the formation of crystals.⁸ Different reaction mechanisms may cause different times required for crystallization. Separation of the crystals from solution is done by vacuum filtration in air.

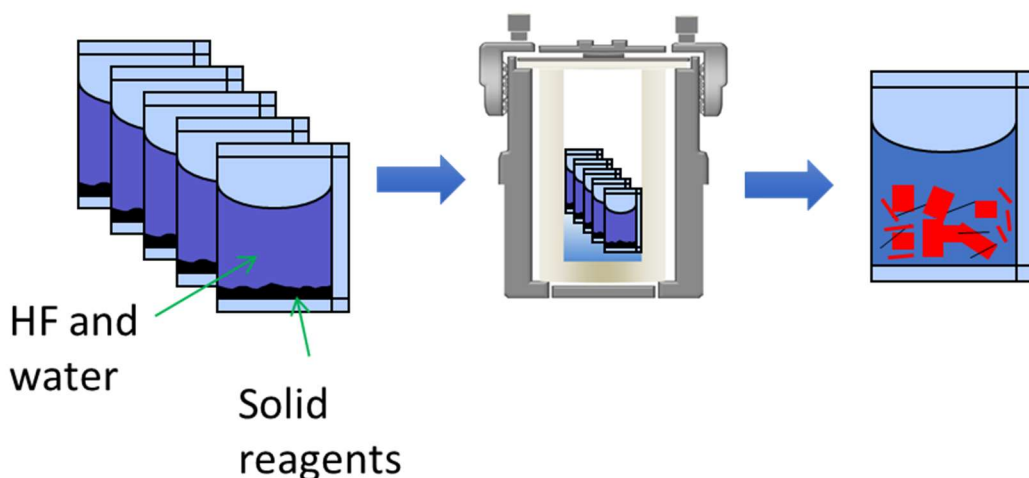


Figure 7. The solid reagents and desired solvent are placed in pouches made of Teflon film. Up to six pouches can be placed in single autoclave. Following the heating of the vessel, the pouches are removed and the crystals are separated using vacuum filtration.

1.5 Hydrofluoric acid and the precautions used

As hydrofluoric acid is used in almost all the reactions presented in this work, its inherent dangers should be addressed. Hydrofluoric acid is a toxic and corrosive acid and proper training,

protective gear, and precautions to protect others are necessary.³³⁻³⁵ Given the deserved infamy of hydrofluoric acid, it may occur to some that perhaps it would be better to not use it at all. Many compounds have been synthesized hydrothermally using other sources of fluorine, such as fluoride salts, but this is not always successful. While solid state methods have also been used to synthesize fluorides and oxyfluorides, the hazards of using fluorine gas as a controlled atmosphere or of producing fluorine gas as a by-product make this reaction method undesirable. It is not often that one uses the word “safe” in conjunction with “hydrofluoric acid”, but it is preferable to many of the alternatives. Furthermore, hydrofluoric acid is not used merely as a fluorine source, but also as a mineralizer and a source of acidity. Also, hydrofluoric acid is used to dissolve otherwise inert metal oxides.

There has never been an incident in the Poepelmeier lab involving hydrofluoric acid. All the members of our group are trained in how to use it safely and how to respond to an emergency involving hydrofluoric acid, regardless of whether that individual uses it for their research. In addition to normal personal protective equipment (i.e. lab coat, safety glasses, etc) while working with hydrofluoric acid an additional pair of Silver Shield gloves (rated for chemical protection against hydrofluoric acid) is worn, along with a lab apron, and a breathing mask rated for nuisance levels of hydrofluoric acid. On top of this, all experiments involving hydrofluoric acid are performed in a pre-determined, labelled area of the lab to minimize the risk to others. Reactions with hydrofluoric acid are heated only in furnaces placed inside a hood, so that in the event of an autoclave failure, the fumes would be exhausted away from the lab space.

1.6 An overview of this work

The projects described in this work investigate the relationships between the BBUs and the larger structures of several fluorides and oxyfluorides, in particular how the BBUs affect the properties observed. The key questions of this research are how are NCS BBUs formed with the aid of hydrogen bonding, how does the arrangement of NCS BBUs relate different structures, how does the arrangement of NCS BBUs affect the properties of the material, and how do the local thermal expansion properties of BBUs differ from the overall structure. While complete answers to any one of these questions are possibly beyond the scope of many lifetimes of work, the research presented here attempts to add to the available knowledge of the field. In $\text{CuVOF}_4(\text{H}_2\text{O})_7$, the structure is NCS because the shape of the BBUs causes preferential stacking. The hydrogen bonding in this material is examined to better understand how it affects the formation and stabilization of the BBU. $\text{CuMnF}_5(\text{H}_2\text{O})_7$, a previously unknown material with a related structure, is centrosymmetric despite containing acentric BBUs; in addition it is pleochroic. This property is also seen in the compound KNaMnF_5 , another centrosymmetric structure with NCS BBUs. The effect of thermal changes on the BBUs of KNaNbOF_5 are studied to better understand how the local thermal properties relate to those of the unit cell as a whole. In addition, an overview of the synthesis and characterization, particularly the x-ray crystallography, of RbCuS and RbCuSe is provided as a supplement to previously published papers. Finally, the rocking curve measurements of several large single crystal samples are discussed in-depth as this research was scattered across many articles.

Chapter 2: Hydrogen Bonding in $\text{CuVOF}_4(\text{H}_2\text{O})_7$

2.1 Abstract

A co-refinement of single crystal x-ray and neutron diffraction data has been used to accurately locate the hydrogen atoms within the structure of $\text{CuVOF}_4(\text{H}_2\text{O})_7$. X-ray crystallography alone was insufficient to determine the hydrogen positions within this structure as they are not geometrically or chemically constrained, as is the case in many inorganic materials. $\text{CuVOF}_4(\text{H}_2\text{O})_7$ presents an additional obstacle in that vanadium is a weak neutron scatterer. The two diffraction methods are combined to take advantage of the strengths of each. The hydrogen bonding distances as well as the hydrogen atom positions in the unit cell are markedly different from those previously reported for this compound. The intra-dimer hydrogen bond is actually weaker than the hydrogen bonds between the dimer and the free water molecule in the structure. The water-dimer hydrogen bonds may be more significant in the formation and stabilization of the distorted shape of the dimer than was previously realized.

2.2 Introduction

This paper presents a study of the hydrogen bonding in the noncentrosymmetric (NCS) structure of $\text{CuVOF}_4(\text{H}_2\text{O})_7$ using a combination of single crystal x-ray and neutron diffraction, as well as a look at the hydrogen positions found through density functional theory. NCS structures are of considerable academic and commercial interest owing to the variety of properties they exhibit including nonlinear optical properties such as second harmonic

generation.¹⁻³ Understanding these structure-property relationships adds to our library of tools for application-driven crystal design.

$\text{CuVOF}_4(\text{H}_2\text{O})_7$ was first discovered by Donakowski et al in conjunction with the centrosymmetric heterotypes $\text{MVOF}_4(\text{H}_2\text{O})_7$ ($\text{M}^{\text{II}} = \text{Co}, \text{Ni}, \text{Zn}$) with which it offers an interesting comparison.⁴ The $\text{CuVOF}_4(\text{H}_2\text{O})_7$ structure is comprised of bent dimers and a free water molecule as seen in Figure 1, whereas in the centrosymmetric structure the polyhedra do not share any atoms and there is no free water molecule. The bent shape of dimer in $\text{CuVOF}_4(\text{H}_2\text{O})_7$ causes NCS packing, maintaining the polarity of the bulk crystal; conversely the polyhedra of the heterotypic structures pack centrosymmetrically, with no net polarity.

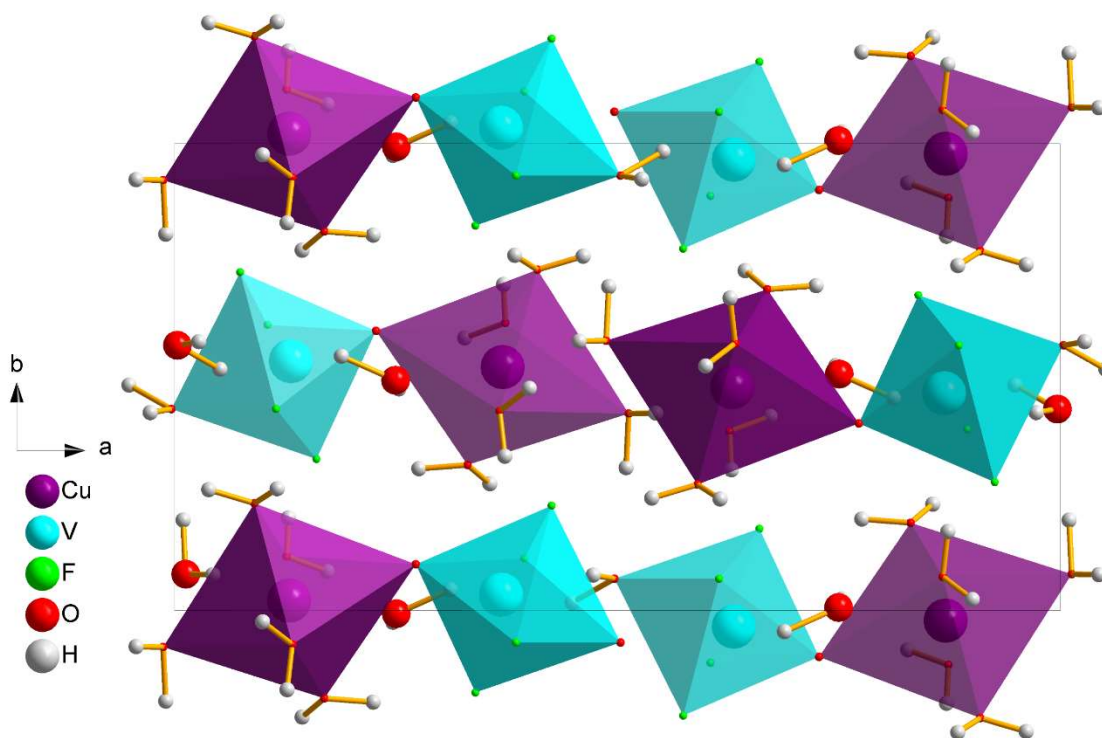


Figure 1. $\text{CuVOF}_4(\text{H}_2\text{O})_7$ unit cell as viewed along the c axis. The structure is composed of bent dimers whose shape favors noncentrosymmetrical packing. Figure based on data from reference⁴

Donakowski et al attribute the bent “lambda”-shaped dimer of $\text{CuVOF}_4(\text{H}_2\text{O})_7$ to the (First Order) Jahn-Teller distortion of the Cu^{II} cation, which makes possible the bimetallic unit, and intra-dimer interactions, specifically the intra-dimer hydrogen bond. This investigation focuses on how the hydrogen bonding between the free water molecule and the dimer factors into the stabilization of the bent shape.

In order to understand the ways that hydrogen bonding contributes to the structure, accurate placement of the hydrogen atoms is necessary; however, x-ray diffraction cannot always provide specific knowledge of the positions of the hydrogen atoms or the lengths of the hydrogen bonds. For many compounds, x-ray diffraction may easily determine the hydrogen atom positions. Within organic structures, or when the hydrogens are part of organic ligands, the hydrogen atoms can often be freely refined, especially when geometric and structural limitations are taken into account. Furthermore, if the structure does not contain heavier elements, the peaks from hydrogen atoms are more easily differentiated from the background. With many inorganic structures, the hydrogen atoms are all but invisible in comparison to the heavier atoms that are usually present. For inorganic compounds, hydrogen positions are normally approximated by crystallography software using average values for bond length based on the literature and then treated as “riding” on a parent atom and not freely refined. If its position in the structure isn't determined by the geometry of the atom the hydrogen is bonded to, the software may incorrectly choose the position. In addition, the built-in assumptions for hydrogen bond length may not be accurate for all structures since hydrogen bonding is not often considered. Even when the hydrogen positions can be reasonably assumed, most software does not freely refine the hydrogen positions or the bond lengths which leaves their accuracy in question.

The two most reached-for solutions to the problem of hydrogen positions are neutron diffraction and density functional theory (DFT). Neutron diffraction has been the standard for accurately determining the atomic positions of hydrogens because hydrogen is a much stronger neutron scatterer than it is an x-ray diffractor. However, vanadium atoms are all but invisible to neutron diffraction (a scattering length of -0.3824 fm compared to hydrogen's -3.7390 fm)⁵; it is often used as a low-background container for neutron studies for this reason. Because $\text{CuVOF}_4(\text{H}_2\text{O})_7$ contains both hydrogen and vanadium, using either neutron or x-ray diffraction alone would be insufficient to fully understand this structure. The solution used for this compound is a co-refinement of single crystal x-ray and single crystal neutron diffraction, which provides an accurate determination of the hydrogen positions in the context of the other atoms in the structure.

In addition, the experimental data is compared to DFT-determined hydrogen positions. Using DFT to optimize or even locate hydrogen positions has grown increasingly common over the last decade, especially among molecular crystals.^{6,7} DFT has become a useful complement to experimental crystallography, with good overall agreement between structures determined by neutron diffraction and by DFT optimization, as well as providing more in-depth analyses of the interactions involved.⁸⁻¹⁰

2.3 Experimental Methods

2.3.1 Sample preparation

Single crystals of $\text{CuVOF}_4(\text{H}_2\text{O})_7$ were prepared using the hydrothermal method as previously reported⁴, with the following adjustment to the heating profile. In the original synthesis, the acid

digestion vessel was heated to 150 °C for 24 h, cooled at a rate of 0.1 °C/min to 25 °C and then allowed to sit undisturbed for 48 h. In order to obtain larger crystals for single crystal neutron diffraction, the vessel was left undisturbed an additional 48 h to allow yet still further crystallization.

2.3.2 Single crystal x-ray diffraction

Single crystal x-ray diffraction data were collected at 100 K with a Bruker Kappa APEX 2 CCD diffractometer with monochromated Mo K α radiation ($\lambda = 0.71073 \text{ \AA}$). The crystal-to-detector distance was 60 mm. The data were integrated using the SAINT-V7.23A program.¹¹ A numerical absorption correction was applied in the program XPREP.¹² The structure was determined by direct methods with Fourier difference syntheses with XS and refined with XL within the WinGX suite.¹³⁻¹⁵ The flack parameter was determined to be -0.007(7) in the WinGX suite using XL; the negative parameter is probably owing to the small anomalous dispersion effect of the atoms of this compound. This structure agrees well with the previously reported structure.⁴

2.3.3 Single crystal neutron diffraction

Single crystal neutron diffraction data were obtained at Oak Ridge National Laboratory using the HB-3A Four-Circle Diffractometer on the High Flux Isotope Reactor. The detector is a scintillator-based 2D Anger Camera and a multilayer-[110]-wafer silicon monochromator is used at an angle of 47.5 °. The principle incident wavelength used was 1.54056 Å. The collection temperature was 100 K. The neutron diffraction data were refined using FullProf v.2.0.1.^{16,17}

2.3.4 Co-refinement

Both sets of diffraction data were collected on the same single crystal and at the same temperature. The x-ray structure was used as a basis structure in FullProf for the neutron data, which was used exclusively to refine the hydrogen positions, while the heavier atoms were held constant. Once the hydrogen positions were determined, they were manually added to the x-ray cif-format file. SHELX automatically adds the AFIX7 constraint to hydrogen atoms, which allows them to “ride” on a parent atom (the principle atom to which the hydrogen is attached), at a fixed distance, and to not be freely refined. This constraint was replaced with the DFIX restraint, which allowed SHELX to refine the hydrogen bond distance determined by neutron diffraction within a provided standard deviation; in this case, $\text{esd} = 0.001$. The positions were not restricted, but the isotropic displacement parameters were set at 1.5x that of the parent atom.

2.3.5 Density Functional Theory

DFT calculations were done by Helge Rosner (IFW-Dresden) using the co-refined crystallographic information file as a starting point. The resulting ‘relaxed’ positions of the hydrogen atoms are shown for comparison and to illustrate the potential of DFT as a supplement to x-ray crystallography.

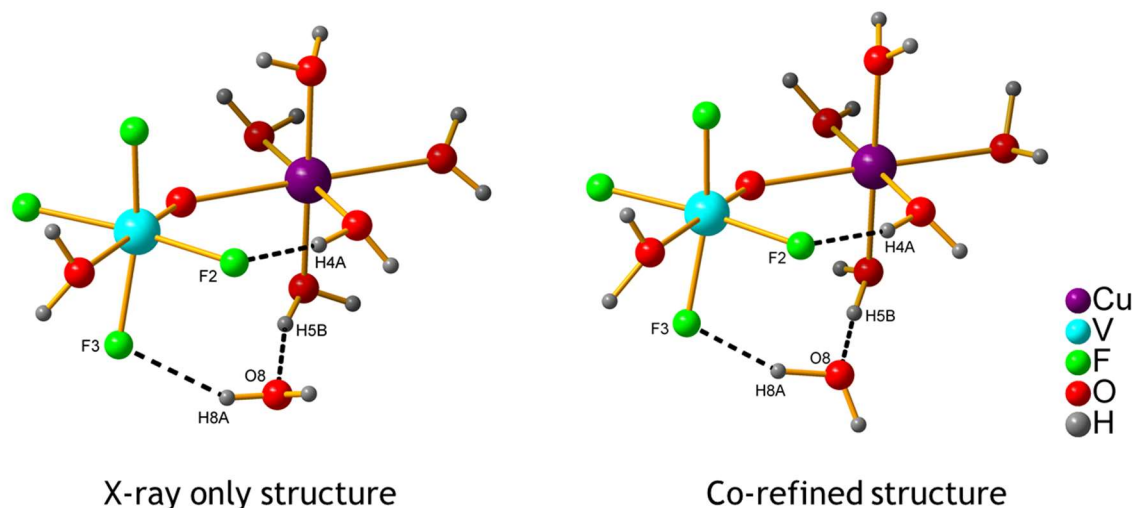
2.4 Results and discussion

From the co-refinement of the single crystal x-ray and neutron diffraction data, we are able to determine the hydrogen positions within the $\text{CuVOF}_4(\text{H}_2\text{O})_7$ structure, the crystallographic parameters of which are shown in Table 1.

Table 1: Crystallographic data

	CuVOF ₄ (H ₂ O) ₇
Crystal System	Orthorhombic
Space Group	<i>Pna2₁</i>
a (Å)	15.6094(4)
b (Å)	8.2085(2)
c (Å)	7.3563(2)
α (°)	90
V (Å ³)	942.56(4)
Z	4
Crystal Size (mm ³)	0.117x0.084x0.073
Independent Reflections	2543 [R _{int} = 0.0422]
ρ _{calc} (g/cm ³)	2.3436
R1	0.0172
wR2	0.0438
GooF	1.030
Flack	-0.007(6)

A comparison of the co-refined structure and the structure with the hydrogen positions as determined solely using x-ray diffraction is shown in Figure 2. For our purposes, the comparison is made to the x-ray data collected for this work rather than the originally reported structure⁴; even though the data agrees well, using the data collected on the same crystal avoids differences from thermal factors and other conditions.



H-bonds (A...H-O)		Distance (Å)		
A	H	X-ray only	Co-Refined	DFT
F2	H4A	1.7848(17)	1.8178(75)	1.6947
F3	H8A	2.0752(19)	1.8327(225)	1.7500
O8	H5B	1.7337(24)	1.6576(210)	1.5824

Figure 2: The structures with the hydrogen atoms determined by x-ray and by co-refinement with neutron diffraction data are shown above. Below is a comparison of the key hydrogen bonding distances.

Looking at the hydrogen atoms from each data set, in some cases the positions are fairly similar, with only small changes to the bond distance or angle, and in other cases the water ligand is greatly rotated. While it is not unreasonable for the water ligands to exhibit some freedom of rotation in the structure, there is no indication in the refinement of positional disorder on the hydrogens. Furthermore, the inter-dimer hydrogen bonding and van der Waals forces may add to the stability of their positions. These positional differences are seen even more clearly in Figure 3 which overlays the hydrogen positions found from each of the three methods on one asymmetrical unit.

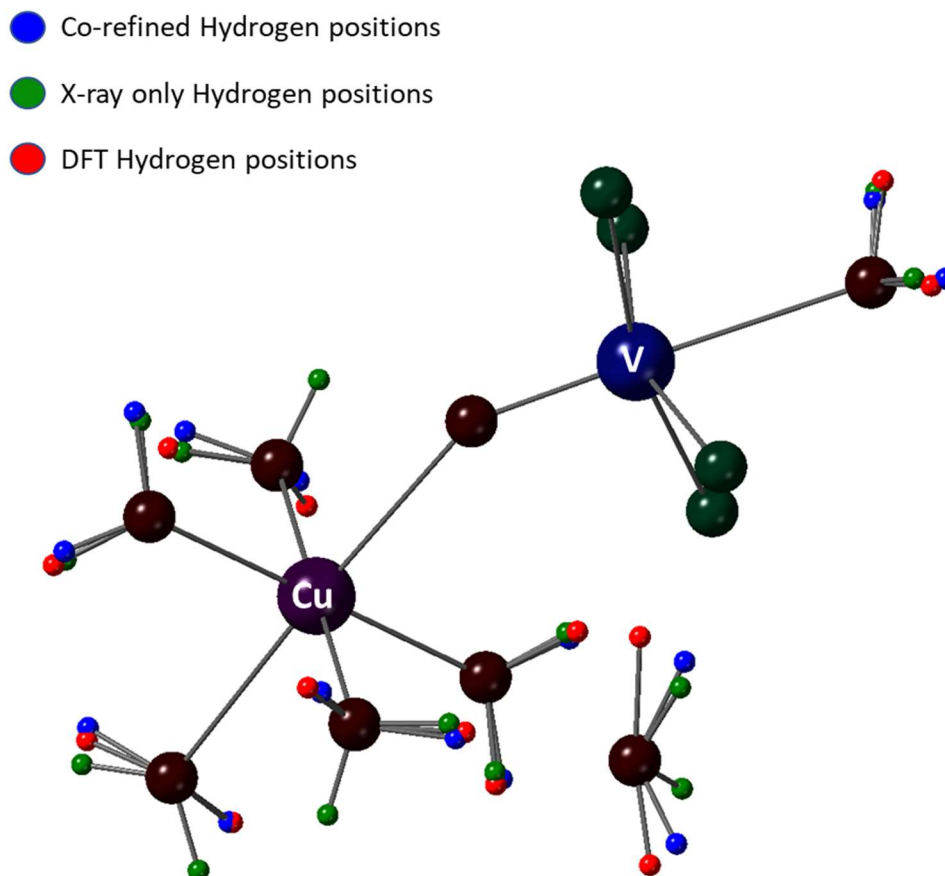


Figure 3. The dimer is shown with an overlay of the hydrogen atoms from each of the three methods of determination; the light blue are from the co-refined structure, the light green are from the x-ray only structure, and the bright red are from the DFT determination. Hydrogen bonding interactions are not shown for simplicity.

There is generally good agreement between the co-refined hydrogen positions and those determined using DFT, but the hydrogens from the x-ray solution are often oriented completely differently. Three of the water ligands, the one attached to the vanadium and the two equatorial copper ligands, are fairly consistent across the three solutions. This may be owing the fact that

the other ligands are involved in hydrogen bonding (either within the dimer, between the dimer and the free water, or weaker inter-dimer interactions). Those hydrogens involved in even weak hydrogen bonding interactions are more likely to be inaccurately positioned by x-ray diffraction. This brings up an interesting point about the hydrogen atom positions: there were visible q-peaks in the x-ray diffraction structure solution that the hydrogen atoms were assigned to, but those positions are incorrect. Recently, Woisnka et al advocated using the Hirshfeld atom refinement (HAR) as a supplement to x-ray diffraction for refining hydrogen positions.¹⁸ However, while HAR shows improved bond lengths for hydrogen atoms, it does not address their spatial position, which is still determined using the q-peaks of x-ray diffraction. For small molecule structures, this works quite well but, as the authors note, for extended networks and for structures like $\text{CuVOF}_4(\text{H}_2\text{O})_7$ with a variety of hydrogen bonds, the accuracy of the refinement is less reliable. Here we can clearly see the limitations we need to be mindful of.

The hydrogen-oxygen bond distances, shown in Table 2, demonstrate the differences in the treatment of hydrogen atoms across the three methods of determination used in this work. In the x-ray only data set, the bond distances are all within a narrow range and the effect of hydrogen bonding is not represented. In the co-refined data, the bond distances are more varied, and as expected, hydrogens involved in hydrogen bonding have longer O-H bonds than hydrogens that are not, as for example O5-H5B (0.9513(205) Å) and O5-H5A (0.6823(82) Å). Hydrogen-oxygen bonds are generally longer when they are part of a hydrogen bonding interaction.¹⁹ The other hydrogen on the water ligand then generally has a shorter bond length, drawn in by the electron density of the oxygen atom. This explains the many O-H bonds in this structure whose lengths are outside the standard range of expected water bond values. While the

DFT calculated structure does not have as much diversity in the bond lengths as the co-refined structure, overall it is a better fit than the x-ray only determination, because the longer bond lengths better reflect the influence of the hydrogen bonding within the structure.

Table 2: Selected O-H Bond Lengths

Atoms		Distance (Å)		
		X-ray only	Co-refined	DFT
O1	H1A	0.8946(21)	1.0470(165)	0.9988(15)
	H1B	0.8931(20)	0.9683(82)	0.9900(16)
O2	H2A	0.8967(20)	0.8437(117)	0.9933(16)
	H2B	0.8958(22)	0.9726(168)	0.9942(15)
O3	H3A	0.8858(21)	0.8218(110)	0.9973(16)
	H3B	0.8849(22)	0.9001(231)	1.0054(16)
O4	H4A	0.8884(22)	0.8709(81)	0.9968(17)
	H4B	0.8868(22)	0.9422(198)	0.9930(15)
O5	H5A	0.8876(21)	0.6823(82)	0.9997(16)
	H5B	0.8888(21)	0.9513(205)	1.0251(15)
O7	H7A	0.9053(20)	0.8240(175)	0.9928(15)
	H7B	0.9048(22)	1.0801(217)	0.9950(15)
O8	H8A	0.8699(25)	1.0911(178)	1.1823(22)
	H8B	0.8706(21)	0.9032(109)	0.9865(22)

While there are many weaker inter-dimer hydrogen bonding interactions throughout the structure, here we will be focusing on the three interactions shown in Figure 2 as they are most likely to be involved in the formation and stabilization of the bent shape of the dimer. The F2...H4A-O4 hydrogen bond was highlighted in the Donakowski et al paper as inducing the distortion of the dimer unit;⁴ based on x-ray diffraction data, this intra-dimer hydrogen bond is shorter and a more direct connection, while the hydrogen bonds between the dimer and the free water molecule are longer and more likely to be contributing to the stabilization rather than

directly affecting the structure. From the co-refined data, we find a different understanding of these interactions. The intra-dimer F2...H4A bond is actually longer than previously determined, whereas the water-dimer hydrogen bonds F3...H8A and O8...H5B are shorter. This indicates that the water-dimer interactions are stronger than we thought, and therefore may be a greater contributing factor than the intra-dimer hydrogen bond. Both are important to the stabilization of the final structure, but these results suggest that the free water molecule is more significant to the development of the distortion of the dimer.

This role reversal is also reflected in the DFT results. The differences between the hydrogen bond distances from the DFT and the x-ray data sets ($\Delta = -0.0901, -0.3252, -0.1513$) support the new understanding of the strength of the water-dimer hydrogen bonding interactions. The shorter distance for the F2...H4A-O4 hydrogen bond is likely more indicative of the DFT-determined distances as a whole than of that bond in particular. Overall, the hydrogen bond distances found in the DFT calculated structure are shorter than both the x-ray only and co-refined distances; however, this is in part due to the somewhat longer hydrogen-oxygen bonds. In the A...H-O interactions, the distances between A and O are the same for both the DFT and the co-refined structures, but DFT assigns more of that distance to the O-H bond rather than the A...H bond.

2.5 Conclusions

Co-refinement of single crystal x-ray and neutron diffraction data was used to look precisely and accurately at the hydrogen bonding of the NCS inorganic structure, $\text{CuVOF}_4(\text{H}_2\text{O})_7$. A comparison of the new hydrogen positions to those previously reported changes the

understanding of the roles of the intra-dimer hydrogen bond and the hydrogen bonds between the dimer and the free water molecule in the structure. The water-dimer hydrogen bonds may be more significant in the formation of the distorted shape of the dimer than was previously realized. Further comparison with DFT calculated hydrogen positions confirms these findings. Accurately determining the hydrogen atom positions and bond lengths gives greater insight into the nature and role of hydrogen bonding in NCS structures.

Chapter 3: Synthesis, Structure, and Pleochroism of $\text{CuMnF}_5(\text{H}_2\text{O})_7$

3.1 Abstract

The structure of the pentafluoromanganate $\text{CuMnF}_5(\text{H}_2\text{O})_7$ is determined for the first time using x-ray crystallography. It crystallizes in the space group $P2_1/c$ with lattice parameters that are consistent with those previously reported ($a = 8.9449(2) \text{ \AA}$, $b = 18.1599(5) \text{ \AA}$, $c = 5.9679(2)$, and $\beta = 96.137(1)^\circ$). $\text{CuMnF}_5(\text{H}_2\text{O})_7$ is however not isostructural with $\text{CoAlF}_5(\text{H}_2\text{O})_7$ as suggested but is instead related to the $\text{CuVOF}_4(\text{H}_2\text{O})_7$ structure by a similar arrangement of the octahedral ionic units. The $\text{CuMnF}_5(\text{H}_2\text{O})_7$ also display strong pleochroism, changing from red to green with the rotation of a polarized light source, and this property is characterized using optical absorption measurements.

3.2 Introduction

$\text{CuMnF}_5(\text{H}_2\text{O})_7$ was first reported by Nunez et al who determined the lattice constants using powder x-ray diffraction and characterized the paramagnetism of the material.¹ $\text{NiMnF}_5(\text{H}_2\text{O})_7$ (reported at the same time) was determined to be isostructural with $\text{CoAlF}_5(\text{H}_2\text{O})_7$ and the differences in the symmetry of $\text{CuMnF}_5(\text{H}_2\text{O})_7$ were assigned to the two Jahn-Teller ions.^{1,2} However, no crystal structure for the $\text{CuMnF}_5(\text{H}_2\text{O})_7$ compound has yet been provided. The $\text{CoAlF}_5(\text{H}_2\text{O})_7$ structure is composed of $[\text{Co}(\text{H}_2\text{O})_6]^{2+}$ and $[\text{AlF}_5(\text{H}_2\text{O})]^{2-}$ octahedral units.² The $\text{MVOF}_4(\text{H}_2\text{O})_7$ ($M = \text{Co}, \text{Ni}, \text{Zn}$) structures similarly contain $[\text{M}(\text{H}_2\text{O})_6]^{2+}$ and $[\text{VOF}_4(\text{H}_2\text{O})]^{2-}$ units, though the Cu analogue has a different structure owing to a bridging oxygen between the two octahedra.³ The similarity of the ionic units of $\text{CoAlF}_5(\text{H}_2\text{O})_7$, $\text{CoVOF}_4(\text{H}_2\text{O})_7$, and $\text{CuMnF}_5(\text{H}_2\text{O})_7$ indicated that there might be a shared structure type.

$\text{Cu}_3\text{Mn}_2\text{F}_{12}(\text{H}_2\text{O})_{12}$, the only other copper manganese fluoride in the ICSD, crystallizes in an anti-perovskite structure, distinctly different from the CsCl-like $\text{CoAlF}_5(\text{H}_2\text{O})_7$ structure.^{1,4}

$\text{CuMnF}_5(\text{H}_2\text{O})_7$ crystals display pleochroism, an optical property in which the color of the crystal varies depending on the viewing direction. Pleochroism is fairly common among inorganic materials, though it is often too weak to be noticeable by eye; strong color variations such as are seen in the tourmalines, iolite, and tanzanite are more rare.⁵ $\text{CuMnF}_5(\text{H}_2\text{O})_7$ crystals change from red to green on rotation of a polarized light. The optical absorption spectrum of this highly pleochroic material is reported along with the crystal structure.

3.3 Experimental

3.3.1 Sample preparation

Caution. Hydrofluoric acid is toxic and corrosive! It must be handled with extreme caution and the appropriate protective gear and training.⁶⁻⁸

Copper (II) oxide (Aldrich 99.99%), manganese (III) oxide (Cerac 99.9%), and 48 wt% hydrofluoric acid (Sigma-Aldrich 99.99%) were used as received. The compound was synthesized by reacting 3 mmol of CuO (0.2386 g) and 1 mmol of Mn_2O_3 (0.1579 g) with 1 mL each of deionized water and 48% HF in a fluoro(ethylenepropylene) (FEP) Teflon pouch as previously described.⁹ The pouch was placed in a 125 mL, Teflon-lined Parr acid digestion vessel with 40 mL of deionized water, which was heated to 150 °C at a rate of 0.1 °C/min, held at temperature for 48 hours, and then cooled to room temperature at a rate of 0.1 °C/min. The reaction was then left undisturbed for 48 hours to allow further crystallization.

3.3.2 *Single crystal x-ray diffraction*

Single crystal x-ray diffraction data were collected at 100 K with a Bruker Kappa APEX 2 CCD diffractometer with monochromated Mo K α radiation ($\lambda = 0.71073 \text{ \AA}$). The crystal-to-detector distance was 50 mm. The data were integrated using the SAINT-V8.34A program.¹⁰ A multi-scan absorption correction was applied in the program SADABS.¹¹ The structure was determined by direct methods with Fourier difference syntheses with XT and refined with XL within the WinGX suite.¹²⁻¹⁴

3.3.3 *Optical Absorption Measurements*

Single crystal optical absorption measurements were performed over the range of 4.5 eV (275 nm) to 1.3 eV (953 nm) at room temperature. A crystal of $\text{CuMnF}_5(\text{H}_2\text{O})_7$ was mounted with oil onto a pulled glass capillary and attached with double-sided tape to a custom-made holder. The crystal was then positioned between a polarization-filtered halogen lamp equipped with a half-wave plate and a Nikon Eclipse-Ti inverted microscope equipped with a Nikon 20x/0.45 Plan Fluor ELWD objective. The transmitted light was then focused through a polarization scrambler onto a 1/3 m imaging spectrograph (SP2300, Princeton Instruments), dispersed (150 groove/mm grating), and focused onto a liquid nitrogen cooled CCD detector (Spec10:400BR, Princeton Instruments) for collection. Absorption measurements were acquired at every 10 polarization degrees (0.1 s exposure time with 200 acquisitions).

3.4 Results and Discussion

$\text{CuMnF}_5(\text{H}_2\text{O})_7$ crystallizes in the monoclinic space group $P2_1/c$ and consists of $[\text{Cu}(\text{H}_2\text{O})_6]^{2+}$ cations and $[\text{MnF}_5(\text{H}_2\text{O})]^{2-}$ anions (see Figure 1). The crystallographic parameters are presented in Table 1. The transition metal atoms are in distorted octahedral coordination environments and all the water and fluoride ligands are crystallographically unique. The complexes are organized into unconnected rows; within a plane, two rows of $[\text{Cu}(\text{H}_2\text{O})_6]^{2+}$ cations alternates with two rows of $[\text{MnF}_5(\text{H}_2\text{O})]^{2-}$ anions. The octahedra are offset from each other such that the octahedra will be adjacent to the spaces between octahedra of neighboring rows. This is true of both the a and b directions. This arrangement of the octahedral BBUs can be seen in Figure 2.

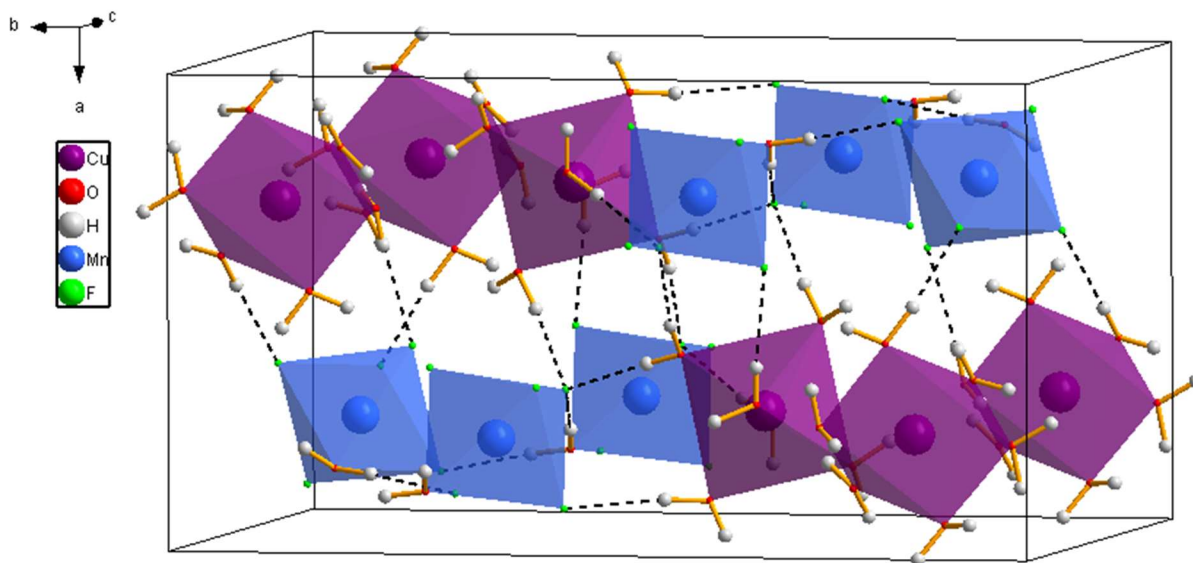
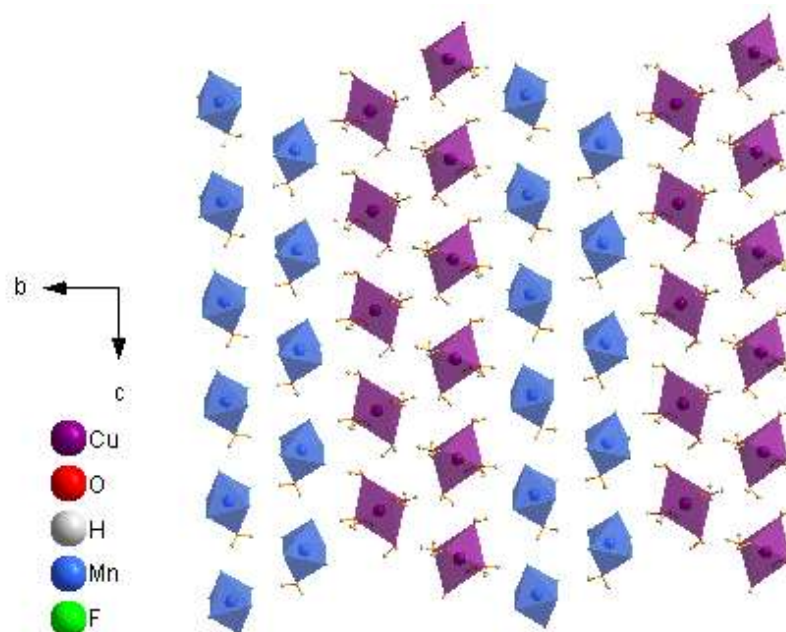


Figure 1: Unit cell of $\text{CuMnF}_5(\text{H}_2\text{O})_7$. The octahedral ionic units are in offset rows, alternating in an $aabb$ pattern.

Table 1: Crystallographic information of $\text{CuMnF}_5(\text{H}_2\text{O})_7$

Chemical formula	$\text{CuMnF}_5(\text{H}_2\text{O})_7$
Formula weight (g/mol)	339.59
Crystal system	monoclinic
Space group	$P2_1/c$
a (Å)	8.9449(2)
b (Å)	18.1599(5)
c (Å)	5.9679(2)
β (°)	96.137(1)
V (Å ³)	963.86(5)
Z	4
Crystal size (mm)	0.236 x 0.217 x 0.106
N_{ref}	2834
ind reflns $>2\sigma$	2748
ρ_{calc} (g/cm ³)	2.34004
R_1	0.0171
wR_2	0.0470
GooF	1.121

**Figure 2:** The octahedral BBUs of $\text{CuMnF}_5(\text{H}_2\text{O})_7$ are arranged in alternating double lines, though they are not connected into chains.

The copper and manganese coordination environments are illustrated in Figure 3, and the metal-ligand bond distances, as well as selected hydrogen bonding distances, are listed in Table 2. The copper octahedra is elongated along the O1–Cu–O4 axis, indicating a Jahn Teller distortion typical of Cu(II) complexes. This is also seen in the Mn(III) octahedra which is elongated along the F1–Mn–O7 axis. Because the $[\text{MnF}_5(\text{H}_2\text{O})]^{2-}$ anion is not a true oxide-fluoride, there is not a preferentially mixing of the manganese d orbitals with the oxygen $2p$ orbitals over those of the fluorine, and thus no second order Jahn Teller distortion is seen. The Mn–F1 bond distance is actually slightly shorter than that of the Mn–O7. The equatorial ligands on both complexes are at roughly 90° angles from the elongated axis (Table 3). The Jahn Teller distortion (in addition to the asymmetrical ligands on the manganese complex) gives rise to two different acentric units in the structure, but this does not ultimately lead to a noncentrosymmetric material.

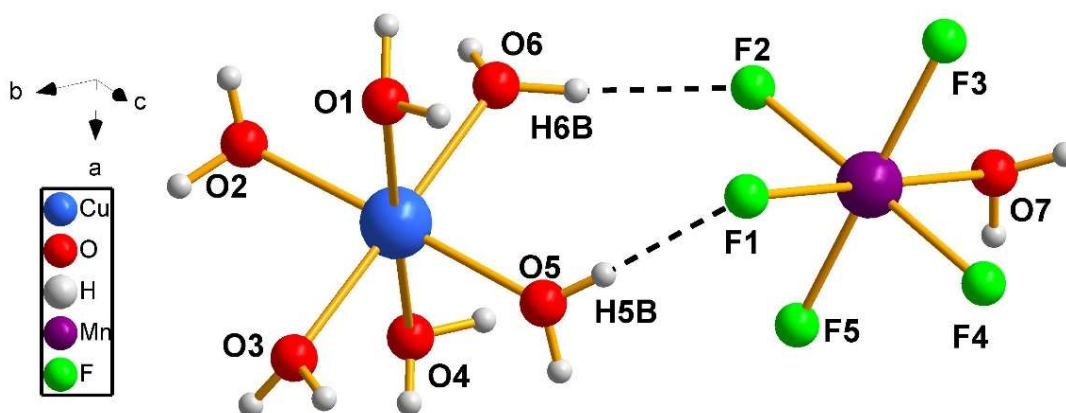


Figure 3: Illustration of $[\text{Cu}(\text{H}_2\text{O})_7]^{2+}$ and $[\text{MnF}_5(\text{H}_2\text{O})]^{2-}$ ions. In conjunction with the bond distances in Table 2, it can be seen that both octahedra exhibit a Jahn Teller distortion.

Table 2: Selected Bond Distances

Bond	Distance (Å)
Cu–O1	2.3542(8)
Cu–O2	1.9534(8)
Cu–O3	1.9920(8)
Cu–O4	2.3294(8)
Cu–O5	1.9251(8)
Cu–O6	1.9827(8)
Mn–F1	2.1046(7)
Mn–F2	1.8526(7)
Mn–F3	1.8528(7)
Mn–F4	1.8410(7)
Mn–F5	1.8545(7)
Mn–O7	2.2405(8)
O5–H5B···F1	1.84(2)
O6–H6B···F2	1.91(2)

Table 3: Selected Bond Angles

	Angle (deg)		Angle (deg)
O1–Cu–O4	178.03(3)	F1–Mn–O7	177.90(3)
O1–Cu–O2	91.19(3)	F1–Mn–F2	89.41(3)
O1–Cu–O3	91.08(3)	F1–Mn–F3	92.13(3)
O1–Cu–O5	88.99(3)	F1–Mn–F4	90.31(3)
O1–Cu–O6	87.69(3)	F1–Mn–F5	91.02(3)
<i>avg</i> O1–Cu–O _{eq}	<i>89.73(6)</i>	<i>avg</i> F1–Mn–F _{eq}	<i>90.72(6)</i>
O2–Cu–O6	89.40(4)	F2–Mn–F3	90.26(3)
O6–Cu–O5	91.85(4)	F3–Mn–F4	90.65(3)
O5–Cu–O3	88.42(4)	F4–Mn–F5	90.97(3)
O3–Cu–O2	90.33(4)	F2–Mn–F5	88.13(3)
<i>avg</i> O _{eq} –Cu–O _{eq}	<i>90.00(8)</i>	<i>avg</i> F _{eq} –Mn–F _{eq}	<i>90.00(6)</i>

In addition to the ionic forces, the units are also connected through a network of hydrogen bonding. Since the hydrogen atoms were determined solely from x-ray diffraction, their positions may be inaccurate, but some insight can be gained from considering the hydrogen bond network

as a whole. The lack of direct connection between the transition metal complexes through a bond may be the reason for the overall centrosymmetry of the material in spite of the presence of two acentric units. Because the octahedra are not restrained by steric or torsion limitations, they are able to rotate into minimal energy orientations which maintain the center of inversion. The plethora of hydrogen bond donor atoms (the oxygens of the water ligands) and acceptor atoms (the fluoride ligands) means that nearly any orientation of the ionic units will result in hydrogen bonding; the hydrogen bonding does not direct a preferential coordination of the octahedra. In short, there is nothing to force or even favor noncentrosymmetric packing, so the structure is centrosymmetric.

The structure of $\text{CuMnF}_5(\text{H}_2\text{O})_7$ was first thought to be a variation of that of $\text{NiMnF}_5(\text{H}_2\text{O})_7$, which has the same structure as $\text{CoAlF}_5(\text{H}_2\text{O})_7$, with allowances for the distortions caused by the inclusion of two Jahn Teller ions in the compound. A comparison of the structure found for $\text{CuMnF}_5(\text{H}_2\text{O})_7$ with that of $\text{CoAlF}_5(\text{H}_2\text{O})_7$ shows that this is not the case. The CsCl-like structure of $\text{CoAlF}_5(\text{H}_2\text{O})_7$ has the octahedral units organized differently than the alternating double-rows seen in $\text{CuMnF}_5(\text{H}_2\text{O})_7$. However, a comparison with the $\text{MVOF}_4(\text{H}_2\text{O})_7$ ($\text{M} = \text{Co}, \text{Cu}$) compounds reveals an interesting relationship. The $\text{CoVOF}_4(\text{H}_2\text{O})_7$ shares the CsCl-type structure of $\text{CoMnF}_5(\text{H}_2\text{O})_7$. The noncentrosymmetric $\text{CuVOF}_4(\text{H}_2\text{O})_7$ however does not have this structure type and instead adopts a configuration not unlike that of $\text{CuMnF}_5(\text{H}_2\text{O})_7$. The lack of bridging oxygen on the ionic units of $\text{CuMnF}_5(\text{H}_2\text{O})_7$ prevents it from forming a dimer like $\text{CuVOF}_4(\text{H}_2\text{O})_7$, but there is a similar pattern of organization. The dimers of $\text{CuVOF}_4(\text{H}_2\text{O})_7$ are formed of joined copper and vanadium octahedral complexes and the arrangement of these two types of octahedra mimics what is seen in the $\text{CuMnF}_5(\text{H}_2\text{O})_7$ structure.

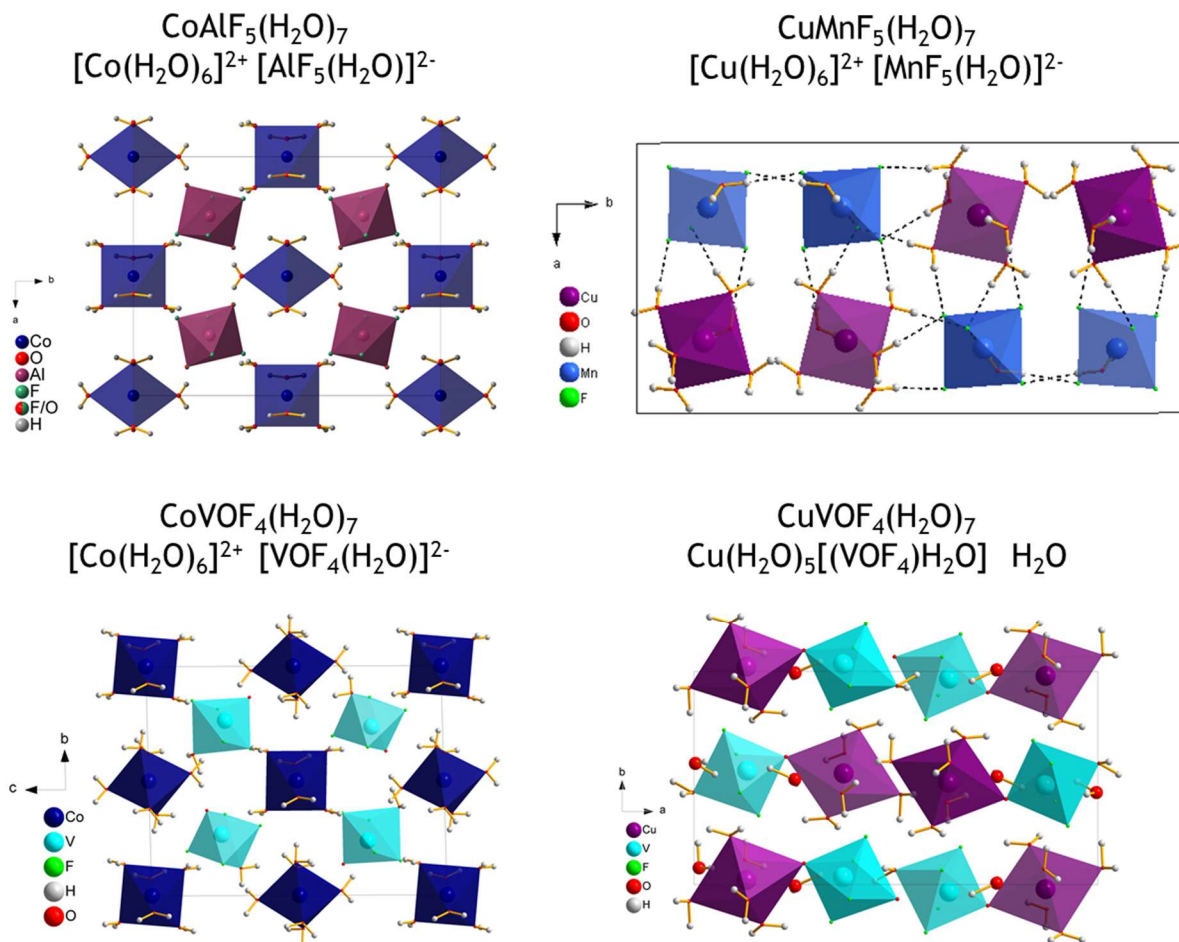


Figure 4: Comparison of the structures of $\text{CoAlF}_5(\text{H}_2\text{O})_7$, $\text{CuMnF}_5(\text{H}_2\text{O})_7$, $\text{CoVOF}_4(\text{H}_2\text{O})_7$, and $\text{CuVOF}_4(\text{H}_2\text{O})_7$. $\text{CuMnF}_5(\text{H}_2\text{O})_7$ was originally thought to be a related structure to $\text{CoAlF}_5(\text{H}_2\text{O})_7$ but it is actually more similar to a version of the $\text{CuVOF}_4(\text{H}_2\text{O})_7$ without the bridging oxygen. The heterotypic $\text{CoVOF}_4(\text{H}_2\text{O})_7$ is a better match for the $\text{CoAlF}_5(\text{H}_2\text{O})_7$ structure.

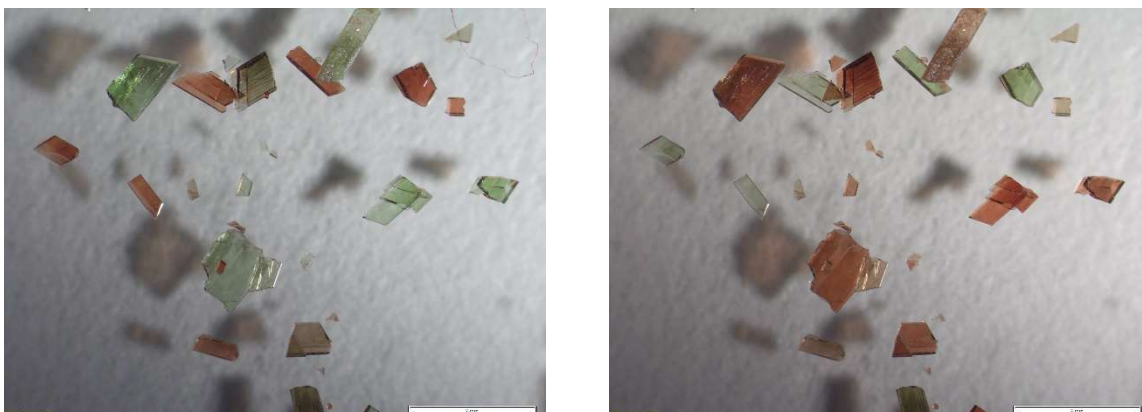


Figure 5: Pictures of $\text{CuMnF}_5(\text{H}_2\text{O})_7$ crystals under a polarized light source. When the light is rotated 90° the color changes from red to green (or vice versa).

While many inorganic materials exhibit some pleochroism, dramatic changes in color are much more rare. $\text{CuMnF}_5(\text{H}_2\text{O})_7$ changes from a bright garnet red to lime green when a light polarizer is rotated 90° , shown in Figure 5. The absorbance spectrum is presented in Figure 6.

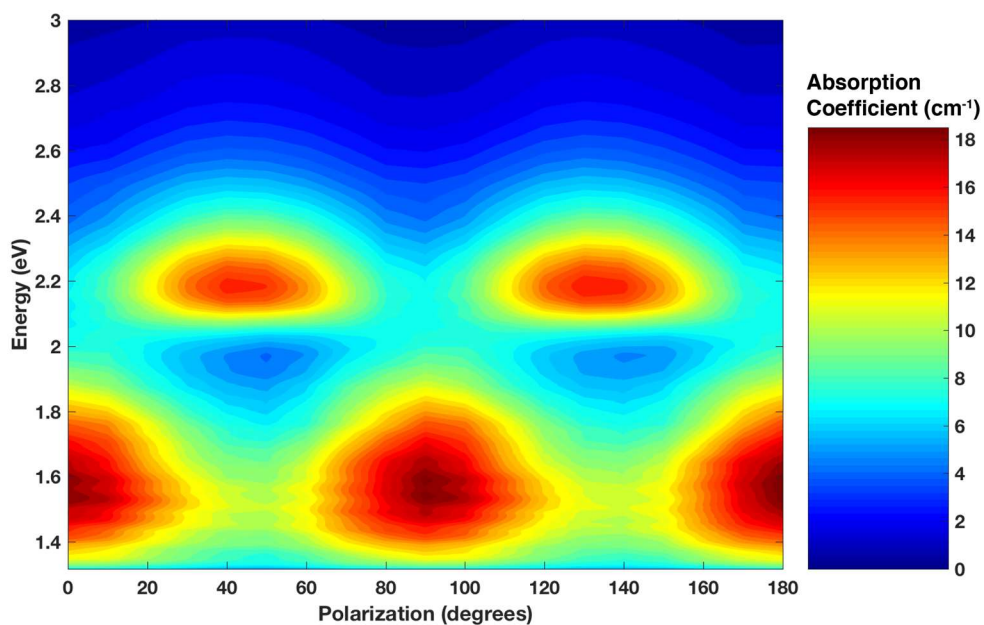


Figure 6: Absorbance spectrum of the $\text{CuMnF}_5(\text{H}_2\text{O})_7$ $(0\bar{1}0)$ face. Two separate absorption peaks are visible, alternating with every 90° of polarization. This matches well with the visible color change.

The peaks of the absorbance spectrum occur at 1.55 eV and 2.15 eV and are likely caused by d-d transitions.⁵ These transitions are between the split energy levels caused by the Jahn Teller distortions of the Cu and Mn atoms. Pleochroism is caused by anisotropic coordination environments around optically active atoms. Both Cu and Mn are in distorted octahedral environments and are probably the sources of the colors seen. The absorption spectrum shows two separate absorption peaks, alternating with every 90° of polarization, which agrees well with the visible color change. It was not possible to collect data on the other planes of the crystal; $\text{CuMnF}_5(\text{H}_2\text{O})_7$ crystallizes in very thin plates that prohibited sufficient absorption for measurement. Crystals with monoclinic symmetry like $\text{CuMnF}_5(\text{H}_2\text{O})_7$ may display trichroism and it is possible that a third optical axis lies along one of the unmeasured directions; however, based on the measurements collected, $\text{CuMnF}_5(\text{H}_2\text{O})_7$ can only be categorized as dichroic.

3.5 Conclusions

$\text{CuMnF}_5(\text{H}_2\text{O})_7$ has been synthesized by the hydrothermal method and its structure has been characterized by x-ray crystallography. It was first reported alongside $\text{NiMnF}_5(\text{H}_2\text{O})_7$ and both were thought to be related to the $\text{CoAlF}_5(\text{H}_2\text{O})_7$ structure. However, the arrangement of the octahedral metal complexes is more comparable to the structure of $\text{CuVOF}_4(\text{H}_2\text{O})_7$, whose connected octahedra are laid out in a similar manner. Optical measurements were used to better understand the dichroism exhibited by $\text{CuMnF}_5(\text{H}_2\text{O})_7$ crystals.

Chapter 4: Crystal Structure and Properties of KNaMnF_5

4.1 Abstract

KNaMnF_5 is a new linear chain pentafluoromanganate of the type $A_2\text{MnF}_5$ and is the first reported in this family of compounds with two different elements on the A site. The crystal structure was determined by x-ray diffraction (space group $Pnma$, $a = 7.6972(2)$, $b = 5.5601(2)$, $c = 10.1973(3)$, $Z = 4$, $R_I = 0.013$ for 1138 reflections). It has a similar Mn–Mn distance ($3.8580(2)$ Å) and bridging angle (133.170°) to those of Na_2MnF_5 , $3.8595(5)$ Å and $132.486(43)^\circ$ respectively. Optical absorbance measurements are used to characterize the red-orange dichroism of the crystals and the spectra show distinct peaks corresponding to the observed color changes.

4.2 Introduction

The family of $A^{(I)}_2\text{MnF}_5 \cdot x\text{H}_2\text{O}$ ($x = 0,1$) and $A^{(II)}\text{MnF}_5 \cdot \text{H}_2\text{O}$ fluoromanganates has been extensively studied, owing to their one-dimensional antiferromagnetic character and their use as model compounds for magnetism studies of more complex systems. Among the $A^{(I)}_2\text{MnF}_5 \cdot x\text{H}_2\text{O}$ ($x = 0,1$) compounds, the Li, Na, K, Rb, Cs, Tl, and NH_4 analogues are known, and the Sr and Ba analogues of $A^{(II)}\text{MnF}_5 \cdot \text{H}_2\text{O}$ have been reported.¹⁻¹⁰ The structures feature infinite 1D chains of $[\text{MnF}_6]^{3-}$ Jahn-Teller distorted octahedra separated by alkali or alkaline earth cations (and water in the case of the hydrates). The angle of the Mn-F-Mn bridge has been shown to be a particularly important factor in the resulting intrachain exchange interactions.³ KNaMnF_5 is a new isostructural compound, the first reported $AA'\text{MnF}_5$ in the series.

The crystals of KNaMnF_5 exhibit pleochroism, like $\text{Tl}_2\text{MnF}_5 \cdot \text{H}_2\text{O}$ and some others in this family.⁸ Pleochroism is a common optical property in inorganic materials in which the color of

the crystal changes according to the axis along which it is viewed. The structure and optical properties of KNaMnF_5 are discussed.

4.3 Experimental

Caution. Hydrofluoric acid is toxic and corrosive! It must be handled with extreme caution and the appropriate protective gear and training.¹¹⁻¹³

4.3.1 Sample preparation

Potassium fluoride (Sigma Aldrich 99.0%), sodium fluoride (Sigma Aldrich 99%), manganese (III) oxide (Cerac 99.9%), and hydrofluoric acid (48% HF_{aq} by weight) were used as received. Crystals of KNaMnF_5 were synthesized by the reaction of 2 mmol of KF, 2 mmol of NaF, 1 mmol of Mn_2O_3 , 1 mL of 48% HF, and 1 mL of deionized water in a Teflon [fluoro(ethylenepropylene), FEP] pouch made using the previously described method.¹⁴ The single pouch was placed in a 125 mL Teflon-lined Parr acid-digestion vessel with 40 mL of deionized water, heated at a rate of 0.1 °C/min to 150 °C, held at that temperature for 48 hours, and then cooled to room temperature at 0.1 °C/min. The vessel was then left undisturbed for an additional 72 hours to allow further crystallization. The crystals were then collected using vacuum filtration in air.

4.3.2 Single crystallography

Single crystal x-ray diffraction data were collected at 100 K with a Bruker Kappa APEX 2 CCD diffractometer with monochromated Mo $\text{K}\alpha$ radiation ($\lambda = 0.71073 \text{ \AA}$). The crystal-to-

detector distance was 50 mm. The data were integrated using the SAINT-V8.34A program.¹⁵ A multi-scan absorption correction was applied in the program SADABS.¹⁶ The structure was determined by direct methods with Fourier difference syntheses with XS and refined with XL within the WinGX suite.¹⁷⁻¹⁹

4.3.3 Optical absorption measurements

Single crystal optical absorption measurements were performed over the range of 4.5 eV (275 nm) to 1.3 eV (953 nm) at room temperature. A crystal of KNaMnF_5 was mounted with oil onto a pulled glass capillary and attached with double-sided tape to a custom-made holder. The crystal was then positioned between a polarization-filtered halogen lamp equipped with a half-wave plate and a Nikon Eclipse-Ti inverted microscope equipped with a Nikon 20x/0.45 Plan Fluor ELWD objective. The transmitted light was then focused through a polarization scrambler onto a 1/3 m imaging spectrograph (SP2300, Princeton Instruments), dispersed (150 groove/mm grating), and focused onto a liquid nitrogen cooled CCD detector (Spec10:400BR, Princeton Instruments) for collection. Absorption measurements were acquired at every 10 polarization degrees (0.1 s exposure time with 200 acquisitions)

4.4 Results and Discussion

KNaMnF_5 has an orthorhombic structure in the space group $Pnma$; the crystallographic information is given in Table 1. The structure (shown in Figure 1) is formed of zigzag chains of vertex-sharing $[\text{MnF}_6]^{3-}$ octahedra. The bridging fluorine atoms that connect the manganese octahedra are located in the axial positions. The chains run along the a axis of the lattice and are

separated by K^+ and Na^+ cations. Figure 2 illustrates the packing of the anionic chains and cations in the structure. The chains are arranged such that the octahedra are offset from their nearest neighbors, owing to both steric and electronic repulsions. In viewing down the a axis, it can be seen that the cations separate the chains along the c axis, alternating between a chain and two columns of cations. This pattern is itself offset along the b direction.

Table 1: Crystallographic information for $KNaMnF_5$

Chemical formula	$KNaMnF_5$
Formula weight (g/mol)	212.03
Crystal system	orthorhombic
Space group	$Pnma$
a (Å)	7.6972(2)
b (Å)	5.5601(2)
c (Å)	10.1973(3)
V (Å ³)	436.42(2)
Z	4
Crystal size (mm)	0.23 x 0.164 x 0.09
N_{ref}	1138
ind reflns $>2\sigma$	1138
ρ_{calc} (g/cm ³)	3.22686
R_1	0.013
wR_2	0.0342
GooF	1.392

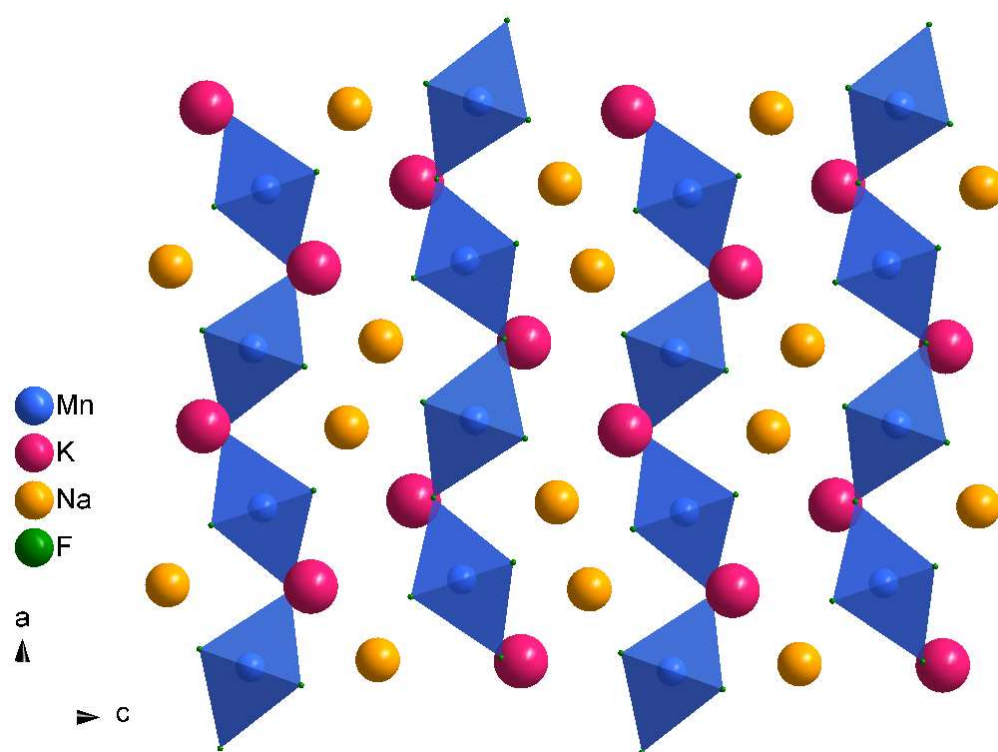


Figure 1: Structure of KNaMnF_5 shown down the b axis. Chains of $[\text{MnF}_6]^{2-}$ octahedra run along the a axis and are separated by K and Na cations.

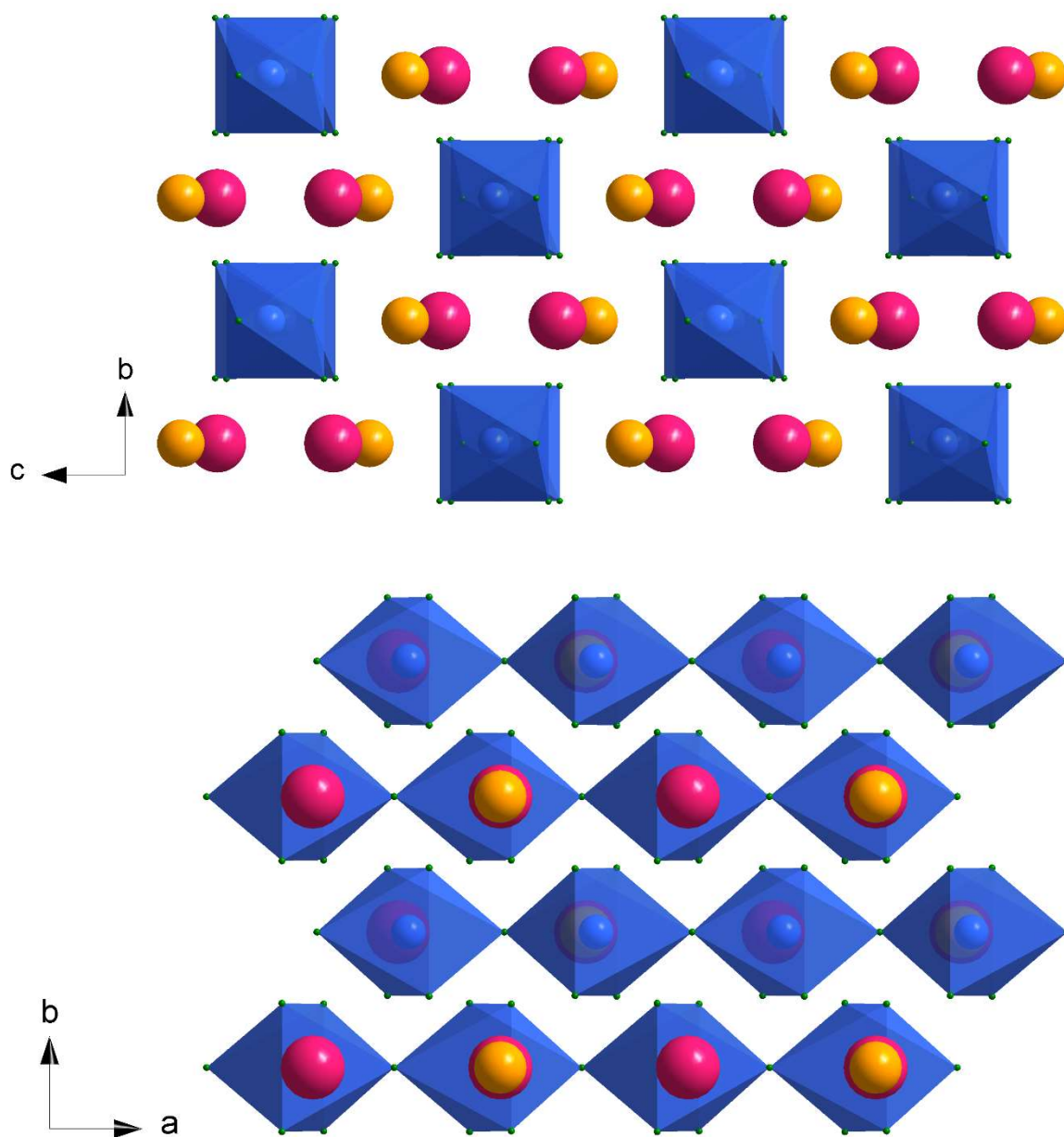


Figure 2: Crystal structure of KNaMnF_5 along the a axis (top) and c axis (bottom). The pictures illustrate the nature of the packing of the manganese fluoride chains. The chains pack together such that the octahedra are offset from their nearest neighbors.

A manganese fluoride chain is illustrated in Figure 3 with atom labels. Selected bond lengths and angles are presented in Table 2. There are three crystallographically unique fluoride atoms, one axial and two equatorial. The octahedral unit is distorted by the Jahn Teller effect, which is expected for a Mn(III) complex in a weak ligand field coordination environment. The axial Mn–F1 bonds are longer than the equatorial Mn–F2 and Mn–F3 bonds. The equatorial ligands are at roughly right angles to each other and to the axial ligands, though the F1–Mn–F1 bond angle is slightly bowed at $172.274(33)^\circ$. This is likely owing to interactions with the nearby cations. The Mn–Mn distance is $3.8580(2) \text{ \AA}$, which is similar to that of Na_2MnF_5 , $3.8595(5) \text{ \AA}$.³ The bridging angle Mn–F–Mn is also similar for KNaMnF_5 and Na_2MnF_5 , $133.170(28)^\circ$ and $132.486(43)^\circ$ respectively.

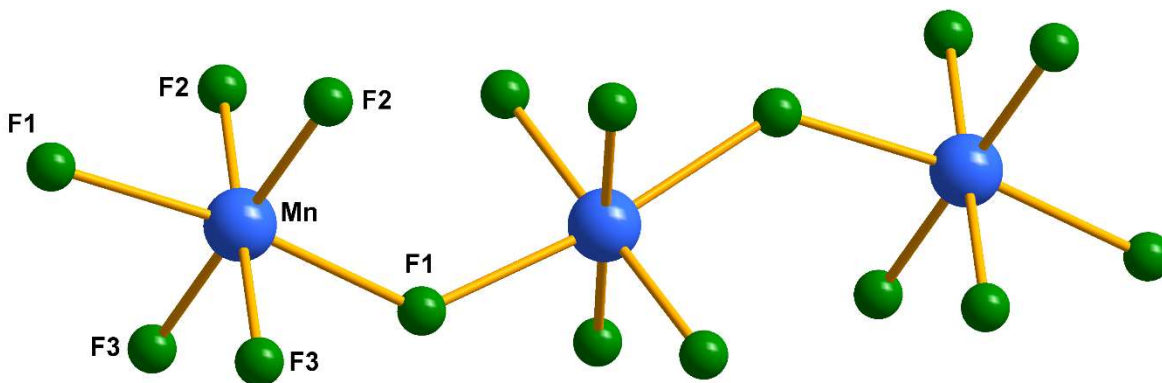


Figure 3: Manganese fluoride octahedra are connected by vertices in chains. The octahedra exhibit the Jahn Teller distortion that is typical of Mn^{III} complexes.

Table 2: Selected bond distances and angles

	Distance (Å)
Mn–F1 ⁱ	2.0909(6)
Mn–F1 ⁱⁱ	2.1133(6)
Mn–F2	1.8437(4)
Mn–F3	1.8598(4)
Mn–K	3.5621(2)
Mn–Na	3.0943(4)
	Angle (°)
F1 ⁱ –Mn–F1 ⁱⁱ	172.274(33)
F1 ⁱ –Mn–F2	89.845(12)
F1 ⁱ –Mn–F3	90.494(12)
F2–Mn–F3	89.897(19)
Mn–F1–Mn	133.170(28)

(i) = $-1+x, y, z$ (ii) = $-1.5+x, -1.5-y, 1.5-z$

When viewed under a polarized light, the crystals of KNaMnF_5 change color from garnet to tangerine orange as the polarizer is rotated. An example of this is shown in Figure 4. While pleochroism is often seen in inorganic compounds, such strong pleochroism is more rare. The optical absorbance spectra of each face are shown in Figures 5-7.

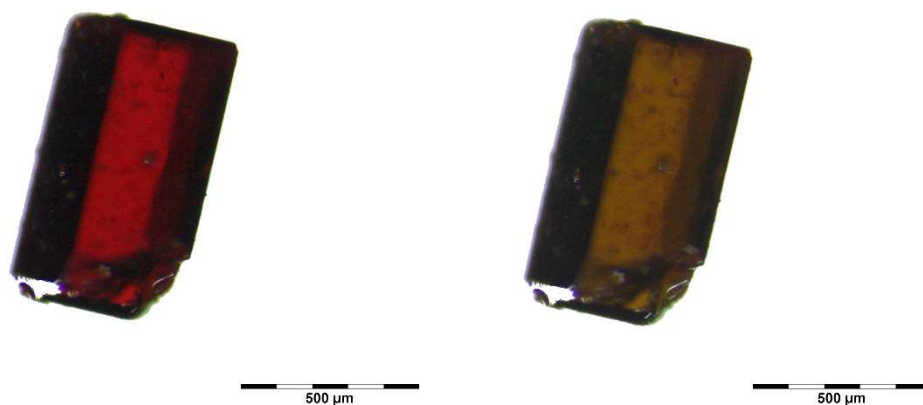


Figure 4: KNaMnF_5 crystal at 8x magnification. The crystal changes from red (left) to orange (right) when a polarized light is rotated.

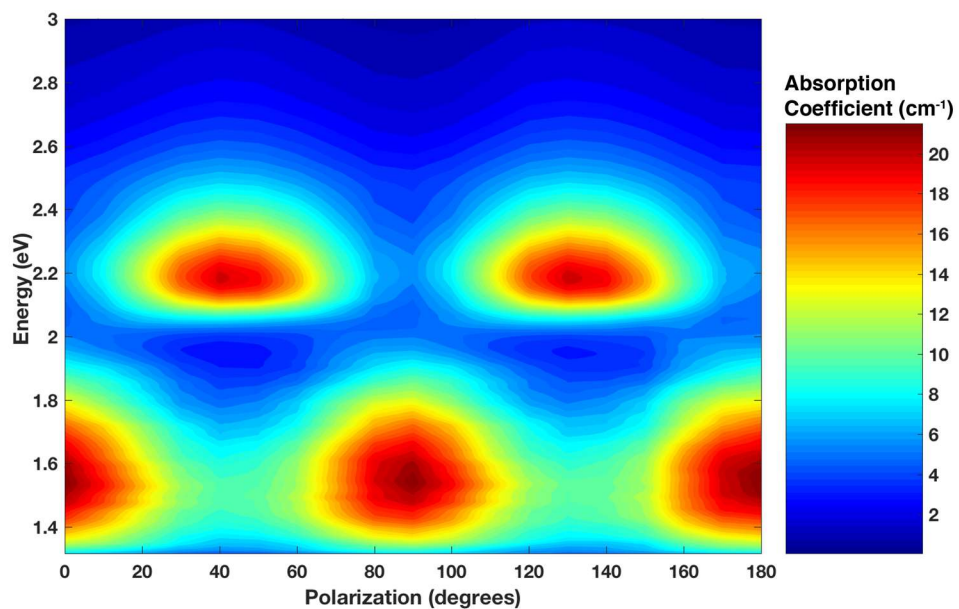


Figure 5: Absorbance spectrum of KNaMnF₅ (001) face. The polarization is linear, and the rotation of colors is seen by the change in absorbance every 90°.

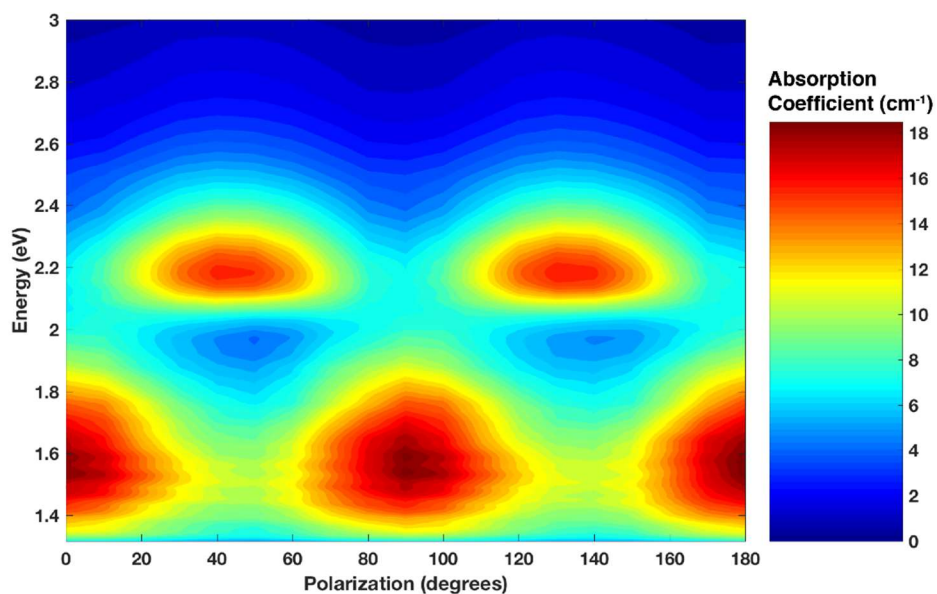


Figure 6: Absorbance spectrum of the KNaMnF₅ ($\bar{1}00$) face. The (001) and ($\bar{1}00$) show similar spectra, indicating that the pleochroism does not greatly differ between these two faces.

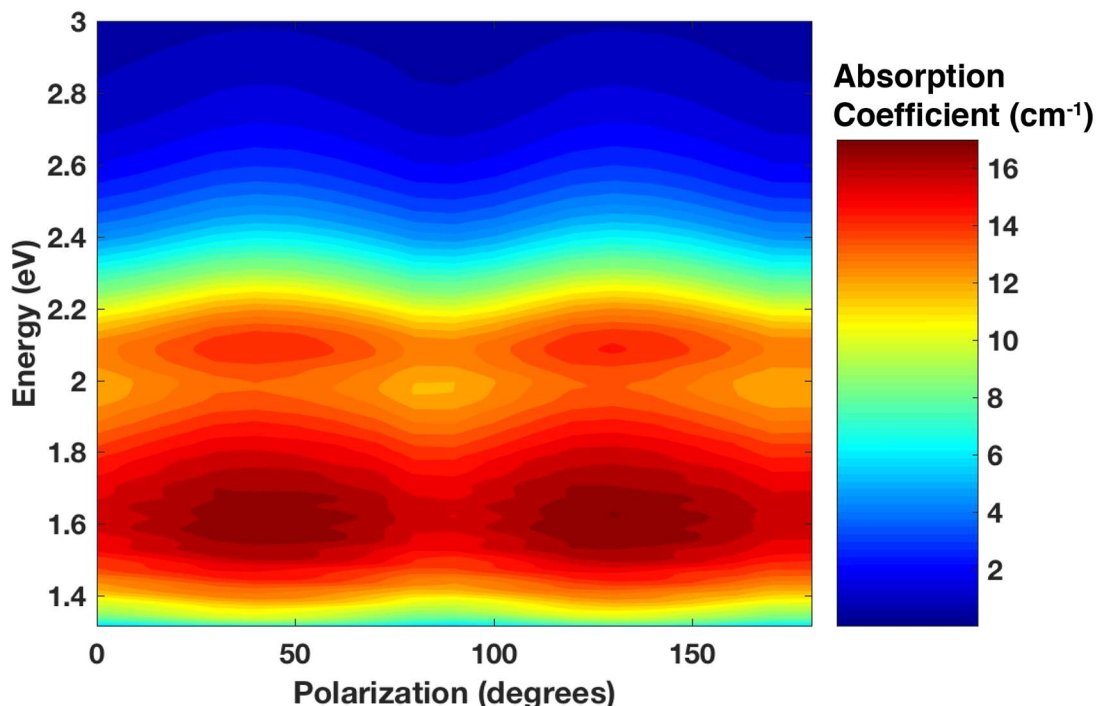


Figure 7: Absorbance spectrum of the KNaMnF_5 (010) face. The absorbance peaks are aligned here, rather than offset. This may imply an overlap of the optical activity, another optical axis entirely, or there may be other effects of the crystal on the absorbance.

In both Figures 5 and 6, two absorbance peaks are seen, which alternate with every 90° of rotation. This matches with what is observed by eye: as the polarized light is rotated, the crystals alternate between red and green. These two spectra are fairly similar, with peaks at 1.55 eV and 2.15 eV. These are likely correlated with d-d transitions of the Mn atom. The third face measured shows a different spectrum. The peaks are at slightly different energies 1.6 eV and 2.1 eV, and instead of being offset from one another, occur at the same polarization. This may be a different optical axis that does not produce a color change discernable by eye. Another possibility is that the transitions seen in the other spectra simply overlap one another in this direction, and the energy changes are due to some artifact of the experiment. It is also interesting to note that while

the absorbance peaks are clearly delineated in the first two spectra, they are more diffuse here. Further studies with higher resolution could elucidate a weak intermediary peak. Orthorhombic crystals like KNaMnF_5 may display trichroism. In addition, because of the orthorhombic symmetry, the optical axes are aligned with the crystallographic axes, providing another way of understanding the source of the different colors. Light traveling down the chains will interact differently with the metal complexes than will light traveling perpendicular to the chains. There is not enough evidence from the current measurements to indicate a definite third optical axis, so for now KNaMnF_5 is classified as dichroic.

4.5 Conclusions

KNaMnF_5 , the first $\text{AA}'\text{MnF}_5$, was synthesized and the structure and properties were characterized. The compound crystallizes in the orthorhombic space group $Pnma$ and like previously reported A_2MnF_5 compounds consists of chains of $[\text{MnF}_6]$ octahedra separated by cations. It has a similar Mn–Mn distance (3.8580(2) Å) and bridging angle (133.170°) to other compounds in the series. Optical absorbance spectra show distinct peaks corresponding to the observed dichroism of the crystals.

Chapter 5: Thermocrystallography of KNaNbOF_5

5.1 Introduction

KNaNbOF_5 is a material that has attracted significant interest and has been studied from many angles. This chapter presents a miniature review of the previous studies of KNaNbOF_5 as well as a new study using thermocrystallography to explore the thermal expansion properties of the compound.

5.1.1 Review of previous studies on KNaNbOF_5

The KNaNbOF_5 system contains both a centrosymmetric (CS) and a noncentrosymmetric (NCS) polymorph and has been studied from a variety of different research interests. The NCS polymorph of KNaNbOF_5 was the first to be discovered and crystallizes in the orthorhombic space group $Pna2_1$ with lattice constants $a = 11.8653(11) \text{ \AA}$, $b = 5.8826(6) \text{ \AA}$, and $c = 8.1258(8) \text{ \AA}$.¹ The structure includes the acentric anion $[\text{NbOF}_5]^{2-}$ which exhibits an out-of-center distortion caused by preferential mixing of the niobium π orbitals with the oxygen π orbitals. The niobium atom is shifted from the center of the octahedron towards the oxide ligand. Previous efforts to use this anion were able to produce compounds containing ordered oxide/fluoride ligands, a key to obtaining NCS structures. However, KNaNbOF_5 was the first instance of the $[\text{NbOF}_5]^{2-}$ anion in a NCS structure that was not an inorganic-organic hybrid.¹ The NCS polymorph's structure is composed of NbOF_5 octahedra edge-shared to NaOF_5 octahedra which form layers of $[\text{NaNbOF}_7]_\infty$. These layers stack to form channels where the K^+ ions are located (see Figure 1). Crucially, the oxide and fluoride ligands are ordered, aided by the different polarizabilities of the

cations in the structure. In addition, the ionic units crystallize acentrically. The K^+ ions occupy positions away from the centers of the channels and toward the axial fluoride ligand. Notably, the related compound $CsNaNbOF_5$ has almost the same structure, except that the larger Cs^+ cation is forced to occupy the center of the channel, resulting in an inversion center. $KNaNbOF_5$ does exhibit second harmonic generation, though it is only around 0.6 x KDP.¹ Studies of the piezoelectricity measured a d_{33} value of $\pm 6.3 \text{ pC/N}^{-1}$.²

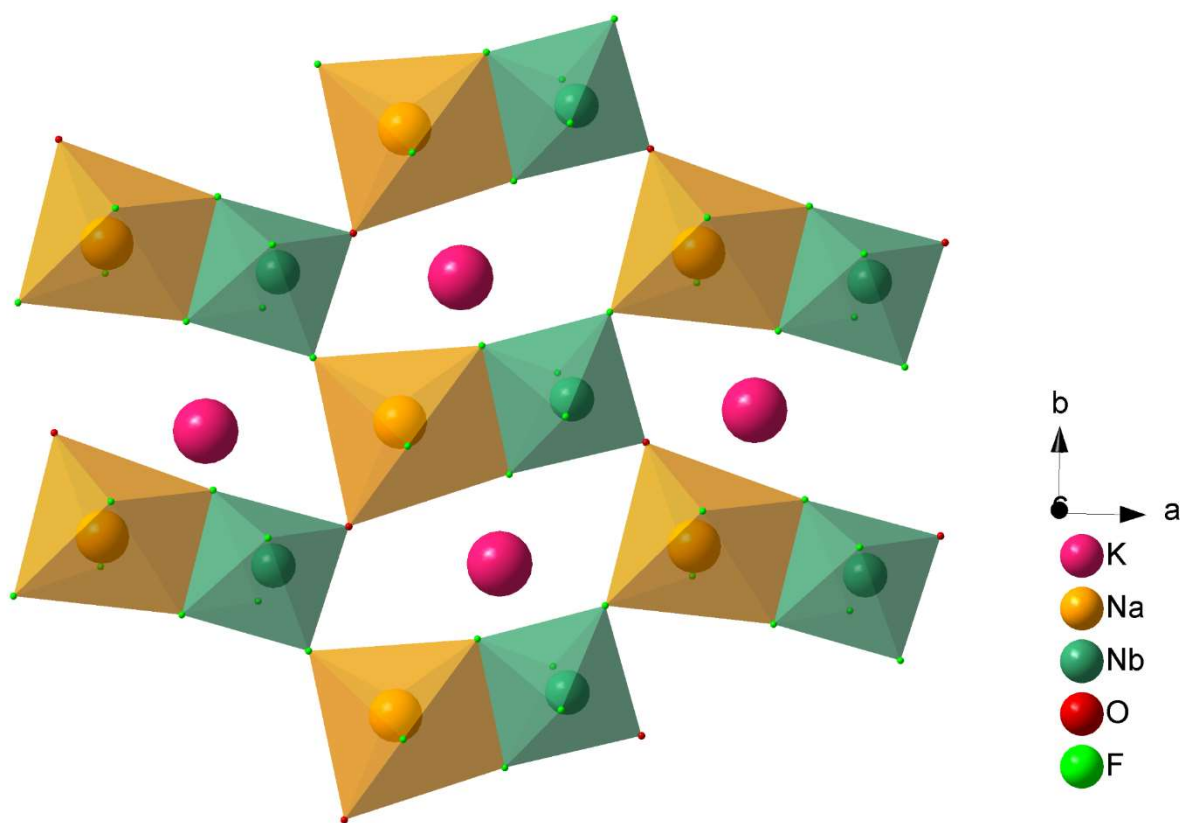


Figure 1: The structure of the NCS polymorph of $KNaNbOF_5$ is composed of layers of $[NaNbOF_7]_\infty$ which stack to form channels that run parallel to the c axis. K^+ ions are located in these channels. Figure adapted from reference ^{a1}

The CS polymorph (first reported by Pinlac et al) has a rock salt double perovskite structure of the general formula $ABB'X_6$ where the Nb^{5+} and Na^+ ions occupy the B and B' sites. K^+ ions occupy half the A sites. The oxide and fluoride ligands are ordered in this compound, with the oxide ligands always in the axial position directed towards the vacant A-site layer. The structure is illustrated in Figure 2. The alternating layers of $[NbOF_5]$ octahedra with the Nb atom shifted in opposite directions compared to the next layer orders the oxide and fluoride ligands, but it also produces a CS arrangement of the anionic units. The dipoles cancel each other completely. Both the CS and NCS polymorphs exhibit triboluminescence, emitting blue sparks when the crystals are crushed. Optical emission spectra and additional testing showed that the mechanism of triboluminescence in these compounds is unassociated with N_2 gas emission or a photoluminescence mechanism; additionally the triboluminescence of the CS polymorph makes it unlikely that this property originates from the piezoelectric effect.²

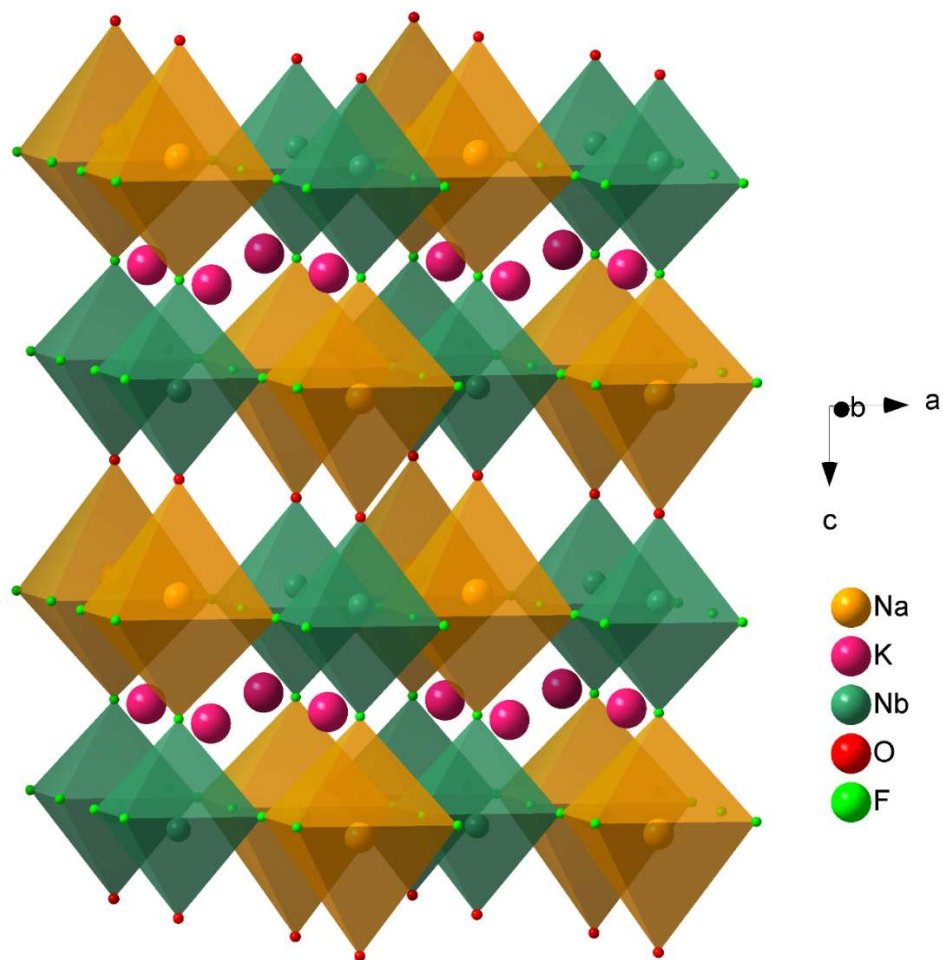


Figure 2: The CS polymorph of KNaNbOF_5 is a rock salt double perovskite. The Na and Nb atoms occupy the B-sites in distorted octahedra. The A-site alternates between layers of K^+ cations and vacancies, which results in the ordering of the oxide and fluoride positions. Figure adapted from reference ^{a2}

The two polymorphs can be controllably synthesized under hydrothermal synthesis by varying the ratio of K to Na in the reagents. While both have been synthesized through a variety of methods, they can be made using the same reactants, reaction conditions, and heating profile, only modifying the K:Na ratio.¹⁻⁶ Using a K:Na ratio of greater than 1:1 produces the NCS polymorph, whereas a lower ratio leads to the CS polymorph.⁴ One study concluded from a

simultaneous growth of both polymorphs that the CS polymorph is a kinetic product, because it crystallizes first, with the NCS polymorph requiring more time.⁶ This is supported by the fact that the NCS polymorph can be synthesized via traditional solid state methods, suggesting that it is the thermodynamic phase.¹

The CS polymorph undergoes an irreversible phase transition to the NCS polymorph upon heating. In situ PXRD studies of the CS KNaNbOF_5 heating to 400 °C and then cooling to room temperature revealed a series of transitions with the NCS polymorph not forming until the last transition upon cooling.⁴ A meta-stable intermediate phase was observed around 360 °C, but direct determination of the phase's lattice parameters was inconclusive based on this data alone. Most transitions in ternary or higher compounds are displacive rather than reconstructive, i.e., involving small changes in atomic position rather than large atomic displacements and chemical bond breaking.⁷ This rendered the transitions of the CS to NCS polymorph particularly interesting to characterize, though more challenging, especially since the frequency and tendency of heteroanionic compounds to undergo reconstructive transitions is not yet well understood.

To understand the transition, it was necessary to determine the structure of the high temperature (HT) phase. This was done through a combination of empirical and theoretical methods. Cryogenic, high-pressure single-crystal diffraction experiments were done using a Diamond Anvil Cell and synchrotron radiation, which minimized the impact of thermal vibrations on the interatomic distances.⁷ The interatomic interaction function parameters were fit to the resulting structures, and the resulting empirical pair potentials were then used to perform molecular dynamics simulations of KNaNbOF_5 .⁷ The HT phase was determined to exhibit dynamic disorder between two phases with almost the same cation sublattice but differing

orientations of the $[\text{NbOF}_5]^{2-}$ units. The pathway of the reconstructive process from the CS to the HT phase was also modelled, the cause of the reconstructive transition was credited to the combination of the polar nature of the heteroanionic units and the vacant cation site.⁷

5.1.2 Thermal Expansion

Most materials exhibit positive thermal expansion (PTE); as temperature increases so does the volume. Negative thermal expansion (NTE), contraction upon heating, is significantly more rare.⁸ Minute variations in the size of small parts can degrade the performance of devices, especially electronic and optical instruments. Controlling thermal expansion is essential to achieving high performances in emerging technologies such as solar cells and thermoelectric converters. Composite materials containing NTE compounds allow tunability of thermal expansion. Research into the mechanism of NTE is on-going in the field.^{8,9}

Change in the lattice volume generally accompany changes in temperature in continuous, smooth curves.¹⁰ This is also usually true for the individual lattice parameters, and one would therefore reasonably expect this to also be true of atomic positions. The trend indicates that in a series of experimentally determined crystal structures, the atom positions and bond lengths would change with temperature in a smooth, continuous manner that mimics the trends of the lattice parameters. However, this is not always the case. Most thermal energy in crystals is in the form of phonon modes which are resonant vibrations that propagate through the lattice.^{11,12} Individual phonon modes are populated unevenly in real crystals, and the distribution changes with temperature.¹³ Phonon mode population distributions may therefore play an important role in the changes to atomic positions at different temperatures.

The ϵ - WO_3 and β - YbV_4O_8 structures both exhibit nonlinear changes to bond distances as temperature increases, though the cell volumes and lattice parameters follow smooth continuous curves.^{14,15} In a neutron powder diffraction study over a temperature range of 5K to 250K, the cell volume and lattice parameters of ϵ - WO_3 follow a smooth continuous curve, but the W-O bond lengths fluctuate nonlinearly for both W^{6+} sites.¹⁴ In β - YbV_4O_8 , a single crystal x-ray diffraction study of a phase transition similarly shows smooth continuous changes in volume and lattice parameters over the temperature range of 100K to 300K (except at the phase boundary).¹⁵ The V-O bond lengths, however, change discontinuously in both phase regions. It is therefore important to consider thermal changes to individual bonds in a structure, rather than just the overall effect of temperature on the lattice parameters.

This is also supported by the recent work of Hu et al in their study of the NTE material cubic ScF_3 which crystallizes in the $Pm\bar{3}m$ space group.⁹ The lattice constant has an average linear thermal expansion coefficient of $-3.1 \times 10^{-6} \text{ K}^{-1}$. Over the temperature range of 300K to 800K, the distance between two neighboring Sc atoms decreases, as expected for a NTE structure; however, the bond length of the Sc-F bond increases in PTE. This has interesting implications for the possible local thermal expansion of units within a structure.

The thermocrystallography study presented here investigates the thermal expansion of individual bonds within the NCS KNaNbOF_5 lattice through a series of single crystal x-ray diffraction (SCXRD) collections over a small temperature range.

5.2 Experimental

5.2.1 *Single crystal x-ray diffraction*

Single crystal x-ray diffraction (SCXRD) data were collected on crystals prepared as previously described¹ with a Bruker Kappa APEX 2 CCD diffractometer with monochromated Mo K α radiation ($\lambda = 0.71073 \text{ \AA}$). The crystal-to-detector distance was 50 mm. The data were integrated using the SAINT-V8.34A program.¹⁶ A multi-scan absorption correction was applied in the program SADABS.¹⁷ The structure was determined by direct methods with Fourier difference syntheses with XS and refined with XL within the WinGX suite.¹⁸⁻²⁰ Data collections were made at 10K intervals across the range 100K to 200K, with each temperature point being measured on two occasions.

5.2.2 *Powder x-ray diffraction*

Powder x-ray diffraction (PXRD) data were collected using a STOE STADI MP diffractometer with Cu K α 1 radiation from $\theta = 6$ to 70° , with a scan width of 0.015° and a scan speed of 480s. The sample was measured at 10K intervals from 100K to 200K, repeating only the 100K measurement.

5.3 Results and Discussion

An overview of the crystallographic refinement parameters for all the data sets included in this study is provided in Table 1. The 150c† data set is the original structure solution reported by Marvel et al.¹ It should be noted that 150c and 100a data sets have noticeably worse R values than the others collected. 150c data set, not being collected on the same crystal, is only shown for

comparison of the unit cell parameters and is not included in the analyses of the atomic positions and bond distances. The R value of the 100a data set compared to all the other sets collected in this study is considerably larger; the application of a Dixon's Q test provides a parameter of 0.743, which when compared to reported values indicates a 99% confidence level for this data set being an outlier.²¹ I have therefore chosen to omit it from this study.

Table 1: Refinement Parameters of the Single Crystal Data Sets

name	100a	100b	110a	110b	120a	120b	130a	130b
temp	100	100	110	110	120	120	130	130
R	0.041	0.0103	0.0179	0.0105	0.0143	0.0108	0.0182	0.0137
wr2	0.117	0.0302	0.0477	0.0302	0.0363	0.0307	0.0455	0.0351
GooF	1.076	1.268	1.258	1.278	1.318	1.283	1.305	1.231
name	140a	140b	150a	150b	150c†	160a	160b	170a
temp	140	140	150	150	150	160	160	170
R	0.0159	0.014	0.0156	0.0134	0.0419	0.0157	0.0154	0.0157
wr2	0.0428	0.0357	0.0419	0.0348	0.1127	0.0411	0.0402	0.0403
GooF	1.284	1.259	1.277	1.265	1.257	1.28	1.235	1.269
name	170b	180a	180b	190a	190b	200a	200b	
temp	170	180	180	190	190	200	200	
R	0.0174	0.0158	0.0151	0.0148	0.0113	0.0151	0.0125	
wr2	0.0439	0.0409	0.0362	0.0386	0.0311	0.0378	0.0324	
GooF	1.149	1.277	1.185	1.306	1.242	1.286	1.307	

† Data from reported CIF from reference^{a1}
All other data sets were collected as part of this study

When comparing the unit cell dimensions of the SCXRD data collections at the same temperatures, there are frequently marked differences in the values obtained. This is especially true of the a parameter. The unit cell lengths are graphed as a function of temperature in Figure 3. A general trend can be seen that as temperature increases, b , and to a lesser extent c , also increases. The graph of the a parameter however is inconclusive at best. Surprisingly, the data does not necessarily become more consistent at lower temperatures. In an effort to obtain more precise unit cell dimensions, PXRD measurements were taken across the temperature range; the average values from a powder sample being thought to provide more accuracy, or at least more consistency, for unit cell parameters than a single SCXRD collection. As can be seen in Figure 4, this did not prove to be an unambiguous solution. Repeated measurements even at lower temperatures are not necessarily similar. It is unclear whether these differences in unit cell length are owing to errors in the measurements or to some inherent flaw in the experiment itself. It should be noted that the differences between many of these parameters is much larger than the reported margin of error. It is not unreasonable therefore to issue a caution to researchers to not assume that the precision of the measurement is exactly what the instrument reports. In acknowledgment of this, throughout this study rather than directly comparing atomic positions or bond lengths, the data points are compared in reference to the appropriate bond length. This will allow the small scale changes to the atom positions and bonds to be appreciable in comparison to the larger changes in lattice parameter.

Using an ANOVA analysis on just the SCXRD unit cell parameters, the correlation of temperature with each of the lattice parameters was tested. Only the p value of b showed a significant correlation ($p = 0.0014$) at the 95% confidence level. The p values of a and c

respectively were 0.678 and 0.112; neither being able to reject the null hypothesis at the 95% confidence level. The correlation between temperature and c must therefore be set aside as statistically insignificant; it is clear that a has no correlation whatsoever. This may be owing to the orientation of the channels to the unit cell. The channels (in which sit the K ions) run along the c axis; this may allow the unit cell more room to stretch perpendicularly along the b axis as temperature increases. It would be interesting to see such motions modelled to better understand the dynamics involved.

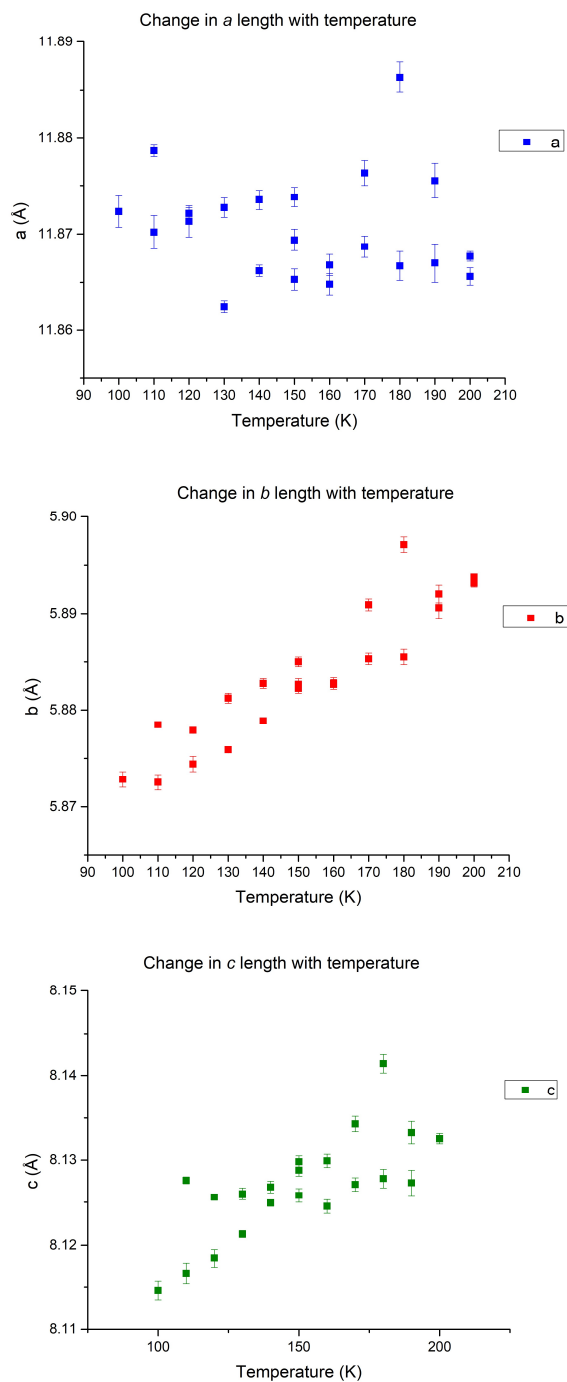


Figure 3: The lattice constants are graphed against temperature. The b and c lattice constants show upward trends, but a is inconclusive. All three show much greater variation than expected.

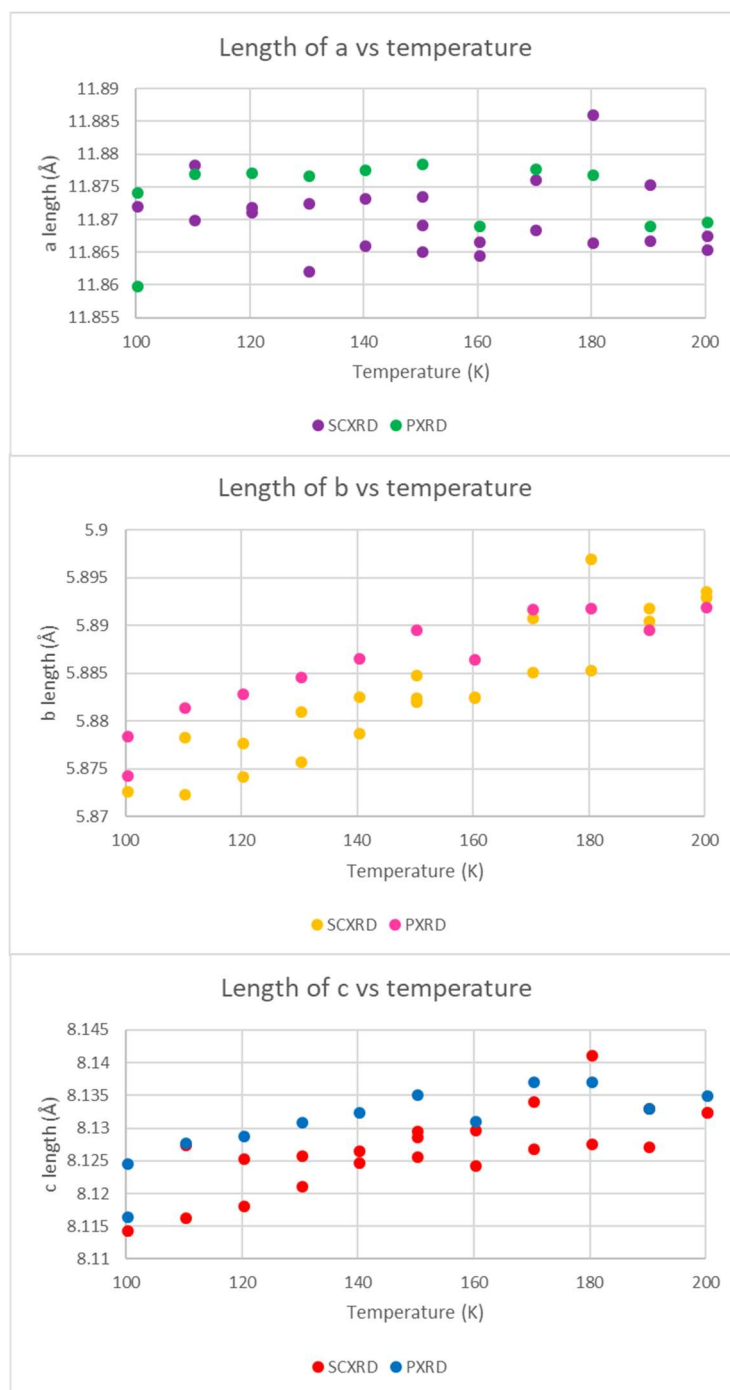


Figure 4: Comparison of lattice parameters measured using single crystal and powder x-ray diffraction (SCXRD and PXRD respectively).

The large variations in unit cell lengths of course translate to the unit cell volume, whose changes with temperature are shown in Figure 5. An upward trend is visible indicative of PTE, which is expected for this compound. ANOVA analysis provides a p value of 0.095, which indicates that there is not a statistically significant correlation between temperature and the unit cell volume at the 95% confidence level. Proceedings from here will assume that the material exhibits PTE, though cautiously, as the quality of the data prevents conclusive determination. The volumetric thermal expansion coefficient can be calculated according the Equation (1):

$$\Delta V = V_0 \beta (t_1 - t_0) \quad (1)$$

in which ΔV is the change in volume, V_0 is the initial volume, β is the volumetric temperature expansion coefficient, and t_1 and t_0 are the final and initial temperatures respectively. For KNaNbOF_5 the values of V_0 and ΔV were extrapolated from the linear trendline. The volumetric thermal expansion coefficient for NCS KNaNbOF_5 across 100K – 200K is $4.38 \times 10^{-5} \text{ K}^{-1}$, which indicates how minute the change is, even given the inconclusive nature of the measurements.

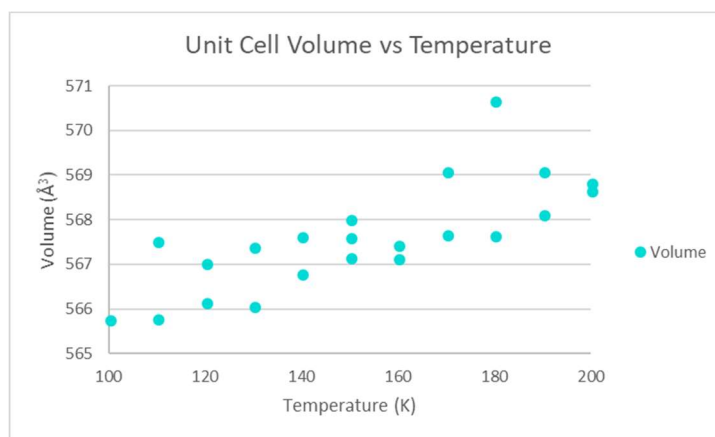


Figure 5: Unit cell volume (from the SCXRD measurements) is graphed against temperature. An upward trend is seen, though with large variation.

Shifts in atomic position were calculated by finding the difference in the x and y coordinates of each data set compared to the 110K and multiplying it by the appropriate unit cell length. The 110K set was chosen so that the 100K set, the low end of the range, could be seen in a visual comparison. Shifts in z could not be reliably determined because there is no crystallographic zero in the z direction. Hence only the shifts in the *ab* plane are considered. Shifts for each of the atoms in the lattice are shown in Figure 6, which mirrors the data across the four quadrants of the graph so as to allow easier comparison of the trends. Each data point on the graph shows the difference in x and y coordinates of that atom for a particular data set. They are not necessarily in order of increasing temperature, but on the whole the larger shifts correspond to higher temperature data sets. The K⁺ ion experiences some of the most displacement, and shifts considerably more than the Nb and Na cations. This is reasonable to expect given the relative freedom of motion the K cations have within the channels. The Nb atoms in fact shift very little as temperature increases. The fluorine and oxygen atoms do shift more, especially F2. This indicates that while the [NbOF₅] units are influenced by thermal expansion effects, it is primarily the ligands rather than the metal atom which respond to the change in temperature. This makes sense given their relative sizes.

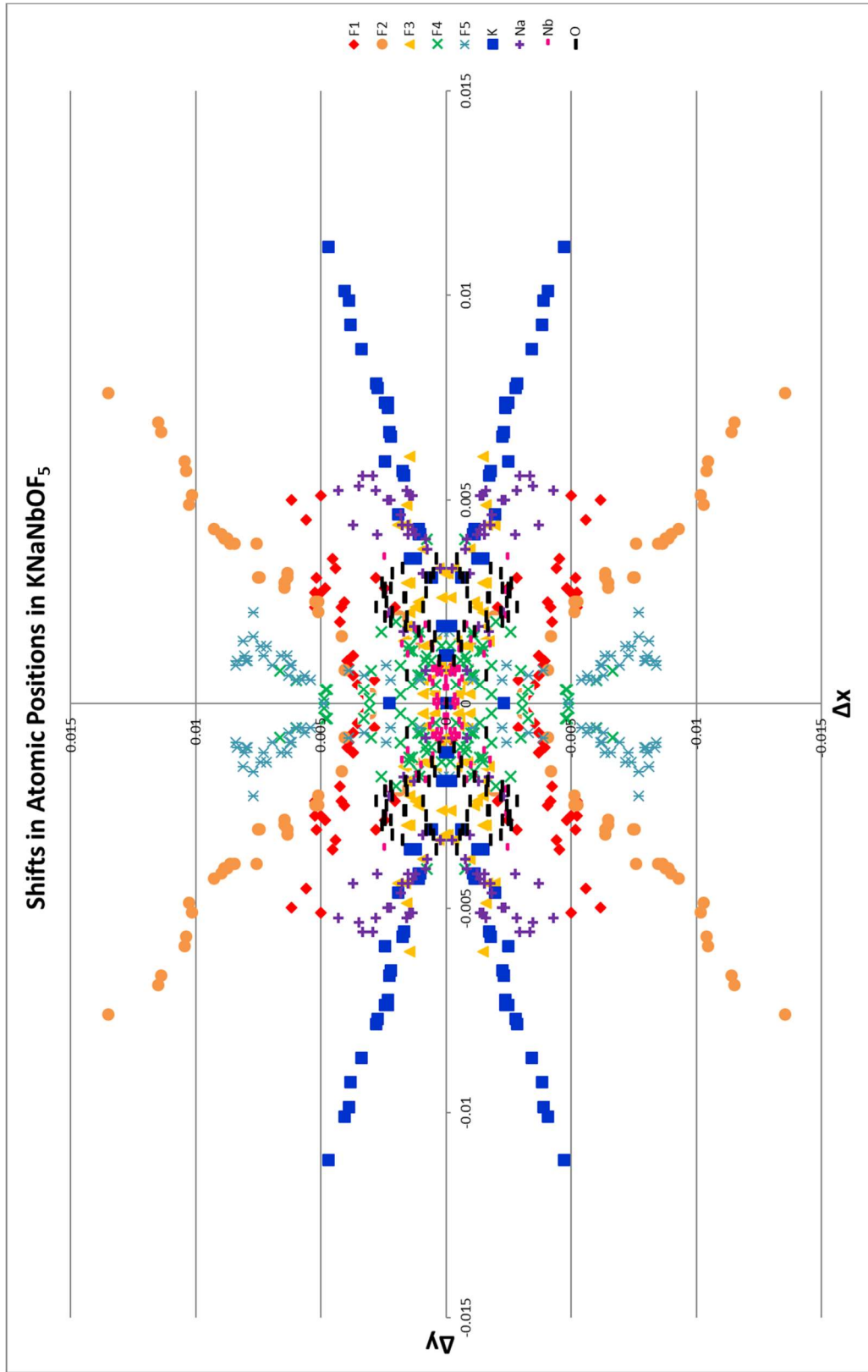


Figure 6: Shifts in atomic position in the ab plane, are shown through the change in the x and y values for each data set compared to those of the 110K data (adjusted to account for changes in lattice size). Because there is no crystallographic zero in the z direction, shifts in z are much less reliable and are not compared. The data has been mirrored across all four quadrants so as to better compare the trends.

Changes in bond distance were calculated by finding the difference between each set and the 100K set for each bond length, and then adding that difference to the bond length from the 100K set to obtain a new 'adjusted' bond length. This was done to minimize the impact of changing lattice constants and focus solely on the effect on the distances between atoms. Twenty different bonds were studied, but most of them show only very slight increases over temperature. The exceptions are some of the K – anion distances and the Nb – ligand distances. A selection of K–F distances and the K–O distance are graphed as a function of temperature in Figure 7. Three of these bonds show PTE and reasonable consistency between data collected at the same temperature, indicating that the results are reliable. Again using a one-way ANOVA analysis, K–F4, K–F5, and K–O have significant p values (4.71×10^{-7} , 2.47×10^{-5} , and 2.37×10^{-6} respectively). K-F3 is neutral (no statistically significant change over temperature). These changes are representative of the K interatomic distances. As previously noted, the K atoms shift noticeably more than other atoms in the lattice, so it is therefore not very surprising that some of the greatest thermal effects should be seen in its bonds. Interestingly, the K–F4 bond lies very nearly along the b axis, which is the only axis to have unambiguous PTE. K–F5 and K–O are perpendicular to the K–F4 bond and are in the ac plane. K–F3 is not aligned along any of the unit cell axes. This may indicate that the changes to the K–F4 bond and the changes to the b axis may be linked, though it is impossible to hypothesize about the nature of that connection; one may cause the other, or they may both be caused by another force entirely.

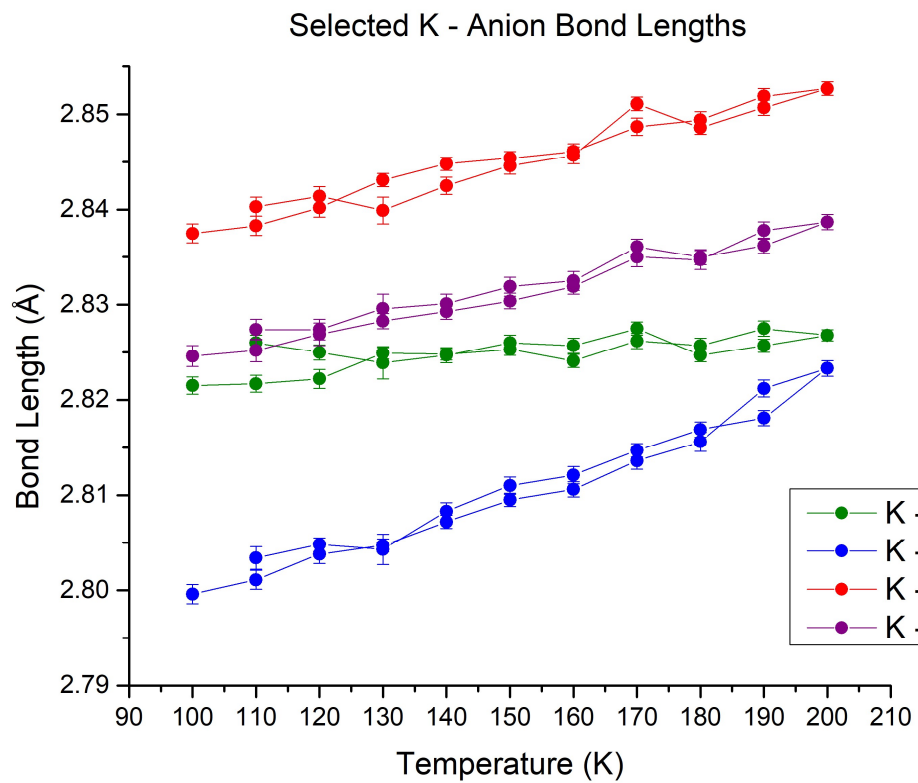


Figure 7: Selected potassium-anion distances as a function of temperature. The positive trends of the data show that these bonds experience PTE.

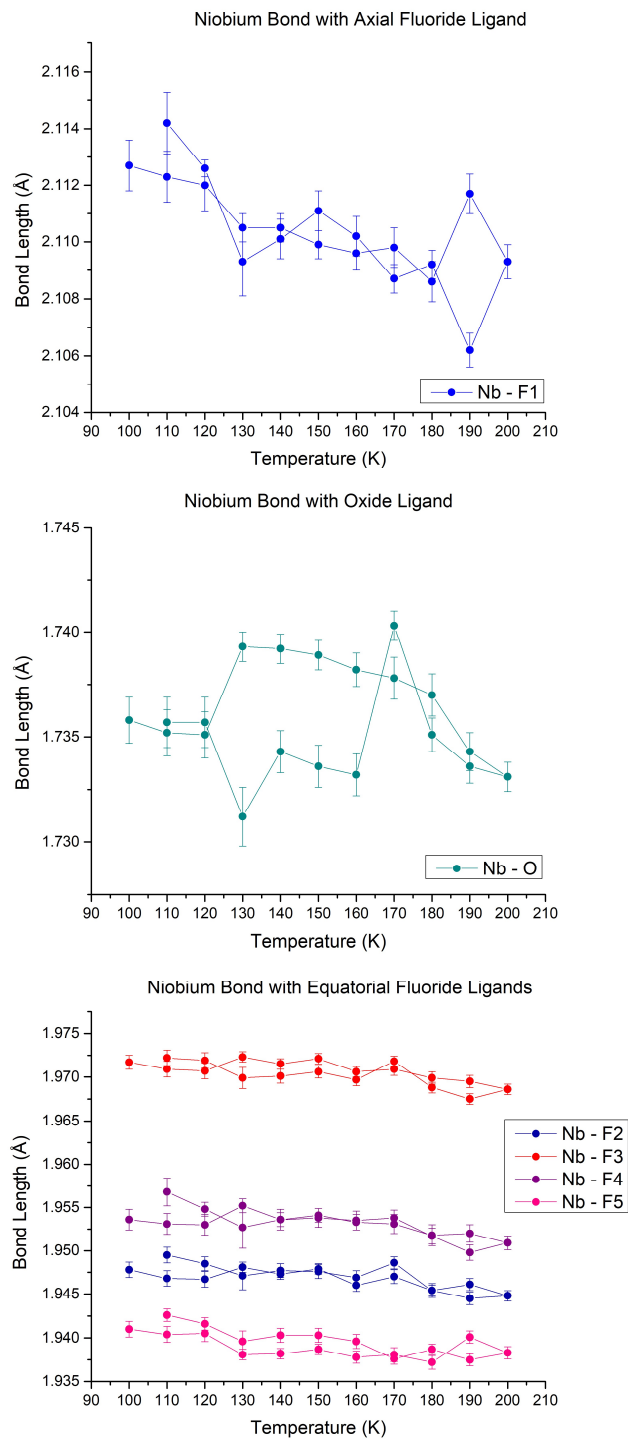


Figure 8: The changes in Niobium – ligand bond length as a function of temperature. In all cases there is a negative slope, indicating NTE for the $[\text{NbOF}_5]$ unit. However, none of these correlations is statistically significant.

The niobium-ligand bonds of the $[\text{NbOF}_5]$ octahedron are also changed by thermal expansion effects, but in the opposite way. As shown in Figure 8, the Nb–F and Nb–O bonds all decrease in length as the temperature increases. These results unfortunately do not stand up to statistical scrutiny; none of them has a p value less than 0.05. The Nb–O bond is especially inconclusive in comparison to the others owing to the greater irregularity in bond lengths. These results therefore serve to indicate a path of inquiry that may yield potentially ground breaking new ways of considering thermal expansion properties. The existence of a NTE anionic unit within a PTE structure would provide a new way of considering the dynamics of NTE as well as open up avenues for new synthetic routes to these desirable materials. It is interesting to point out that none of the Nb–ligand bonds are aligned along a unit cell axis. If a significant NTE of these bonds can be observed, the minor effect the NTE of this unit has on the structure as a whole could be owing to the diffusion of the effect across many directions.

More research is required to understand this phenomenon, but it is possible that changing population distributions of phonon modes affect the thermal expansion properties seen in KNaNbOF_5 . Different phonon modes favored at different temperatures may interact with the structure in ways that cause parts of the structure, like the $[\text{NbOF}_5]$ unit, to expand at lower temperatures, and other parts of the structure like the K^+ ions to occupy more space at higher temperatures. The mechanisms of NTE are still not fully understood, but the knowledge that not all parts of the crystal structure will necessarily mimic the thermal expansion of the unit cell has important implications for future work in the field. Theoretical modelling that includes such considerations could substantially add to the understanding of thermal expansion properties.

Further studies on other compounds that include the $[\text{NbOF}_5]$ anion could elucidate the behavior of this group, and if it is generally NTE, it could become a useful tool in crystal engineering.

5.4 Future Directions

The results presented here offer a tantalizing glimpse into what may be occurring within the KNaNbOF_5 structure, but the data is too ambiguous to draw definite conclusions. One obstacle in conducting this series of experiments was the inability to collect the many data sets continuously. Because the data was obtained using instruments at a shared user facility, it was not possible to collect all of the data in a seamless string of runs. While it would not have been possible to do this without such a facility, the unfortunate downside is that one is obligated to *share* it. This resulted in the data sets being collected in a piecemeal fashion whenever the instrument was available, with the exception of one week during which one diffractometer was generously set aside for this project. Still, at most only about 8 of the twenty sets were collected back to back. This means that the crystal was heated to room temperature and cooled several times at varying intervals throughout the experiment. Ideally, the data sets would be collected one after the other moving from 100 K to 200 K and back, only stopping to allow the temperature to stabilize and to ensure that the crystal was still centered in the beam. Also, given the precision needed, it is important to consider to what degree the temperature is stable and how accurate the temperature reading is. Furthermore, the wide margins of error and large range of values of the unit cell parameters suggest that greater precision is needed overall, especially given the diminutive changes to atomic position that are being examined. Therefore, it may be advisable to consider longer data collections or even synchrotron radiation. Another option for

looking at the changes in the unit cell lengths would be to set up a simple Michelson-Morley experiment which would offer greater precision in observing such minute differences. By measuring the changes to the interference caused by the light moving through subtly different crystal lengths, one could obtain a hopefully clearer idea of the thermal expansion properties of the structure as a whole, which is currently unavailable due to the inconclusive nature of the unit cell parameter measurements from SCXRD. Such an experiment could be done in collaboration with a physics or spectroscopy group.

5.5 Conclusions

NTE is an important property for many commercial applications that involve high-precision electronic and optical components. A series of thermocrystallography experiments on the compound KNaNbOF_5 were used to explore the changes to atomic positions and bond lengths caused by thermal expansion. The volumetric thermal expansion coefficient of KNaNbOF_5 is $4.38 \times 10^{-5} \text{ K}^{-1}$. While some trends can be seen, the data as a whole is inconclusive. Further studies are needed to determine if the $[\text{NbOF}_5]$ unit does indeed exhibit NTE. If this can be achieved, it would suggest that the thermal expansion of individual bonds does not need to follow the trends of the unit cell as a whole. Research on similar systems may bring greater understanding of the mechanism of NTE and guide synthetic efforts to discover new NTE materials.

Chapter 6: Rubidium Copper Chalcogenides

6.1 Source

This work was previously published as part of the following article:

Trimarchi, G.; Zhang, X.; Vermeer, M. J. D.; Cantwell, J.; Poepelmeier, K. R.; Zunger, A.

"Emergence of a few distinct structures from a single formal structure type during high-throughput screening for stable compounds: the case of RbCuS and RbCuSe", *Phys. Rev. B*, **2015**, *92*, 165103.

This chapter will expand on the experimental aspects of the project and go into further detail on the crystallography. This project was a collaboration through the Center for Inverse Design in which my role was the crystallographer of the two compounds reported.

6.2 Background

The goal of the Center for Inverse Design was to use the desired properties to find a suitable structure, rather than the traditional model of materials research which first synthesizes a material and then characterizes the properties it has. A necessary component of this style of investigation is high-throughput screening of candidate structures. To that end, the *ABX* project was designed to provide a feedback loop between screening of compounds based on theoretical modelling and discovering materials through targeted synthesis. The lowest energy structure of an unknown compound is predicted by modelling, and then compared to possible decomposition phases. If it looks like the structure will be stable, a synthesis is attempted. Based on whether the synthesis is successful, and what the resulting structure is (if it exists), the theoretical models are

modified and improved. Future compounds can then, hopefully, be predicted with greater accuracy, and materials discovery can be guided towards those phases most likely to be stable and to have structures likely to produce the desired properties.

The first family of compounds to undergo this treatment was the 18-electron *ABX* compounds. This group includes examples of topological insulators, thermoelectrics and piezoelectrics. Of the 483 possible variations, only 83 were previously reported in the literature. Using first-principles thermodynamics to test the thermal stability of the undocumented compounds, 54 were identified as potentially stable. Of those, 15 were grown and x-ray diffraction verified the predicted crystal structure in all 15 cases.²

The 8-electron *ABX* family is larger, though with more known compounds. Roughly a third of the possible 8-electron *ABX* elemental combinations were known in the literature. Following theoretical modelling, 313 compounds, or approximately 30% of the total 8-electron *ABX* compounds, were predicted to have stable structures, as shown in Figure 1. A more detailed description of the theoretical modelling methods has been previously reported and is not of great concern here.¹

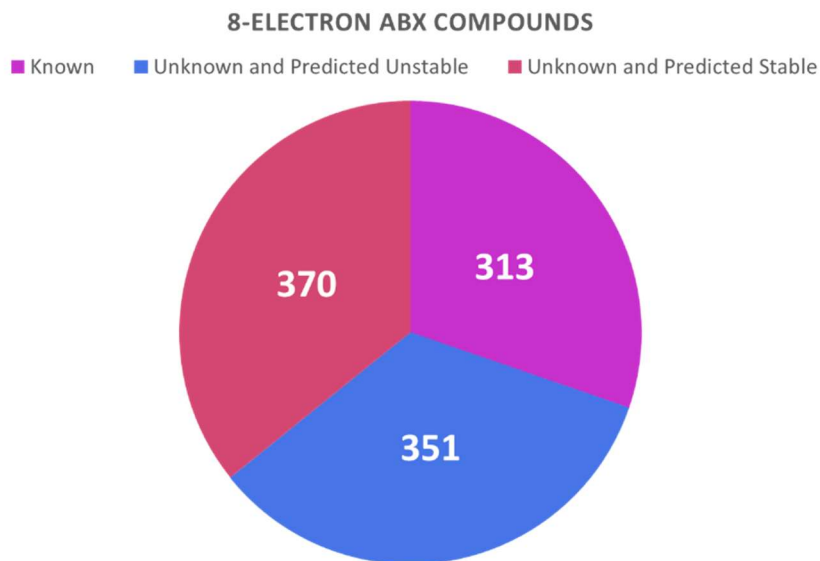


Figure 1. Pie chart illustrating the proportion of 8-electron ABX compounds that are known, unknown and unstable, and unknown and stable. Approximately 30% of the unknown compounds were predicted to have stable structures.

Initial selection from these possible compounds was made by focusing on elements with good relative abundance, low toxicity, and whose melting points were reasonably close. Another factor that quickly limited the scope of experimental synthesis was reactivity with the reaction container. This led to the synthesis of RbCuTe, a MgSrSi-type structure in the space group *Pnma*.³ A chart of the results of the theoretical calculations for the alkali – late transition metal – chalcogenide compounds is given in Figure 2.¹ Upon confirming the predicted structure for RbCuTe, the next compounds to target were the sulfide and selenide analogues. These were also predicted to be stable, with RbCuSe likely to have the same structure. RbCuS was initially predicted to have a CuLiO-type structure. In addition KCuS and KCuSe are known compounds, adding to the likelihood that the rubidium analogues could be made.

		S					
Rb		+	+	✓	✓	✓	✓
K		✓	+	✓	✓	✓	
Na		+	+	✓	✓		
Li		✓	+	✓			
Au		-	✓				
Ag		✓					
Cu							
		Cu	Ag	Au	Li	Na	K Rb

		Se					
Rb		+	+	✓	✓	+	-
K		✓	✓	✓	✓	✓	
Na		✓	+	-	✓		
Li		+	+	-			
Au		-	-				
Ag		✓					
Cu							
		Cu	Ag	Au	Li	Na	K Rb

		Te					
Rb		+	+	✓	+	+	o
K		✓	✓	✓	✓	✓	
Na		✓	+	✓	✓		
Li		+	+	-			
Au		-	-				
Ag		✓					
Cu							
		Cu	Ag	Au	Li	Na	K Rb

+	Missing, predicted stable
-	Missing, predicted unstable
o	Too close to call

Figure 2. A chart of selected I-I-VI ABX compounds and the results of the theoretical modeling. Checkmarks denote compounds already documented in the literature.

6.3 Experimental

6.3.1 Synthesis

In a typical preparation, semi-solid rubidium (Alfa Aesar, 99.75%) was first melted in its vessel on a hot plate, then approximately 3.0 mmol was transferred to the reaction vessel via pipette. Powders of the remaining reagents for each reaction were added to the vessel until the mole ratio of reagents was 1:1:1. Copper powder (Sigma Aldrich, 99.7 %) and selenium powder (Sigma Aldrich, 99.5%) were used in the synthesis of RbCuSe. Due to the likelihood of uncontrolled vigorous reaction between intermixed copper and sulfur powders, the compound CuS (Sigma Aldrich, 99%) was used in place of elemental reagents for the RbCuS synthesis. Reaction vessels were then sealed under vacuum and placed in a furnace for annealing. Reaction temperature ramped up to 650 °C at 5 °C / min. Reactions dwelled at 650 °C for 12 hours, then

were ramped down to 100 °C at 0.1 °C/min, then quickly cooled to room temperature. The synthesis of both compounds was performed by Michael J. DeVries Vermeer.

6.3.2 *Single crystal x-ray diffraction*

Single crystal XRD data were obtained for both structures at 100 K with a Bruker Kappa APEX 2 CCD diffractometer with monochromated Mo K(α) radiation ($\lambda = 0.71073$ Å). The crystal-to-detector distance was 60 mm. The data were integrated using the SAINT-V7.23A program.^{4,5} For the RbCuS data, a numerical absorption correction (Face-indexed absorption correction) was applied to the data in the program XPREP.⁶ For the RbCuSe data, a multiscan absorption correction (SADABS) was applied to the data in the program APEX2.⁹ The structures were determined by direct methods with XS and then refined with the SHELXL algorithm within the OLEX2 suite.^{7,8}

6.4 Structures

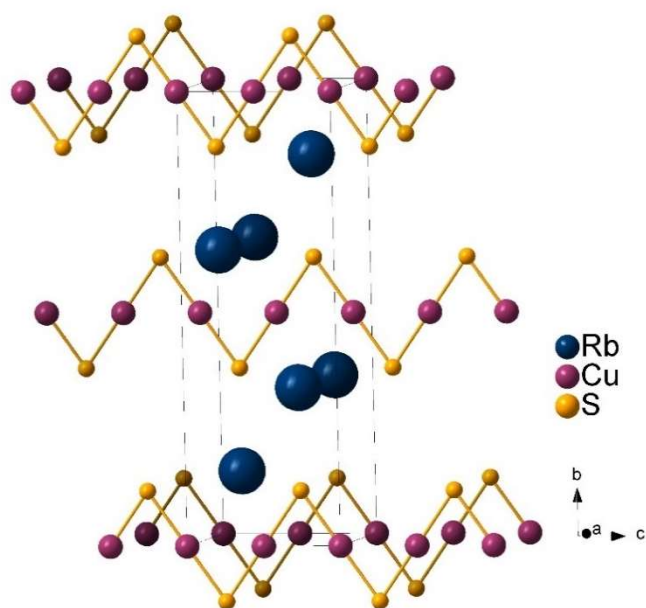


Figure 3. Experimental structure of RbCuS

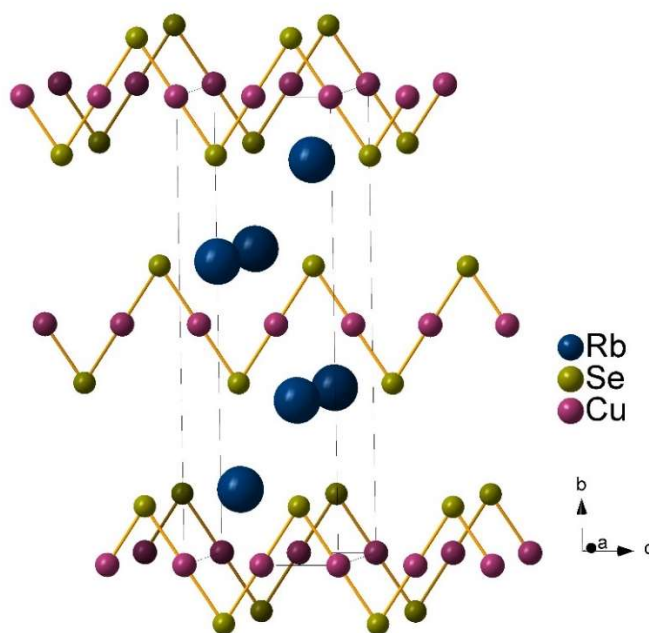


Figure 4. Experimental structure of RbCuSe

Table 1. Crystallographic information for RbCuS and RbCuSe

	<i>RbCuS</i>	<i>RbCuSe</i>
<i>Structure type</i>	RbAuS	RbAuS
<i>Crystal system</i>	orthorhombic	orthorhombic
<i>Space group</i>	<i>Cmcm</i> (63)	<i>Cmcm</i> (63)
<i>a</i> (Å)	4.9007(4)	5.0464(3)
<i>b</i> (Å)	14.4778(9)	15.0388(7)
<i>c</i> (Å)	5.0067(3)	5.0780(3)
α (deg)	90	90
β (deg)	90	90
γ (deg)	90	90
<i>V</i> (Å ³)	355.23(4)	385.38(4)
<i>Z</i>	4	4
<i>N</i> _{ref}	4150	2305
<i>ind reflns</i> > 2 σ	2475	1501
<i>Formula weight</i> (g/mol)	181.07	227.97
ρ_{calc} (g/cm ³)	3.38546	3.92892
<i>R</i> ₁	0.0713	0.0377
<i>wR</i> ₂	.1598	0.0726
<i>Goof</i>	1.073	1.264
<i>Crystal shape</i>	plate	plate
<i>Crystal color</i>	colorless	colorless
<i>Crystal size</i>	0.224x0.103x0.04	0.219x0.177x0.024

Table 2. Copper-Chalcogen Bond Distances and Angles

	<i>RbCuS</i>	<i>RbCuSe</i>
Cu – S or Cu – Se bond length	2.1627(21) Å	2.2711(8) Å
Cu – S – Cu or Cu – Se – Cu bond angle	70.726(2) deg	67.970(2) deg

6.5 Discussion

Collecting single crystal x-ray diffraction data for these two compounds was very difficult for a number of reasons. The first difficulty in working with these samples is that they are both incredibly air-sensitive. The crystals were separated inside the glovebox (using tweezers), covered in zero-background oil, and transported immediately to the diffractometer. While mounting a crystal on the goniometer head for collection, other crystals were visibly degrading, changing color from peach to black, even when submerged in oil. Several crystals degraded too quickly to be used. Once mounted, the sample was still smothered in an excess of oil, far more than would normally be considered necessary or even prudent, and transferred to the instrument where the oil-covered crystal sat under the flow of the nitrogen stream. Once there, the crystal was protected both by the nitrogen stream itself providing an oxygen-poor atmosphere and by the now-frozen oil.

The second difficulty to be overcome to solve the two crystal structures was in finding a sample that was truly a single crystal. Because both compounds form plate-like crystals, they are very prone to twinning. In several cases even four twin laws was not enough to cover all the

twins detected in the data. Untwinned crystals of each compound were eventually found and used for collection. However, with other analogs such as RbAgSe and RbAgTe whose syntheses were attempted no single crystal suitable for x-ray diffraction was found.

RbCuS had previously been reported, though without a crystal structure. RbCuSe was a completely new compound in the literature. Both RbCuS and RbCuSe have a RbAuS-type structure. The copper and chalcogen atoms form zigzag chains separated by Rb cations, as seen in Figures 3 and 4. The Cu-Se-Cu angle is slightly more acute than that Cu-S-Cu angle. This means the chains form a tighter zigzag in the selenide compound than in the sulfide compound. This is principally owing to the greater ionic size of the selenide ion. The Se-Cu-Se and S-Cu-S angles are both 180° . The differences to the sizes of the unit cells are probably largely owing to the differing zigzag angles, as the compounds' structures are otherwise the same. Figure 5 shows the RbCuTe structure for comparison. RbCuTe, which crystallizes in the MgSrSi structure, does not form parallel single chains of copper and tellurium but rather alternating perpendicular double chains.³ RbCuS and RbCuSe were initially predicted to share this structure.

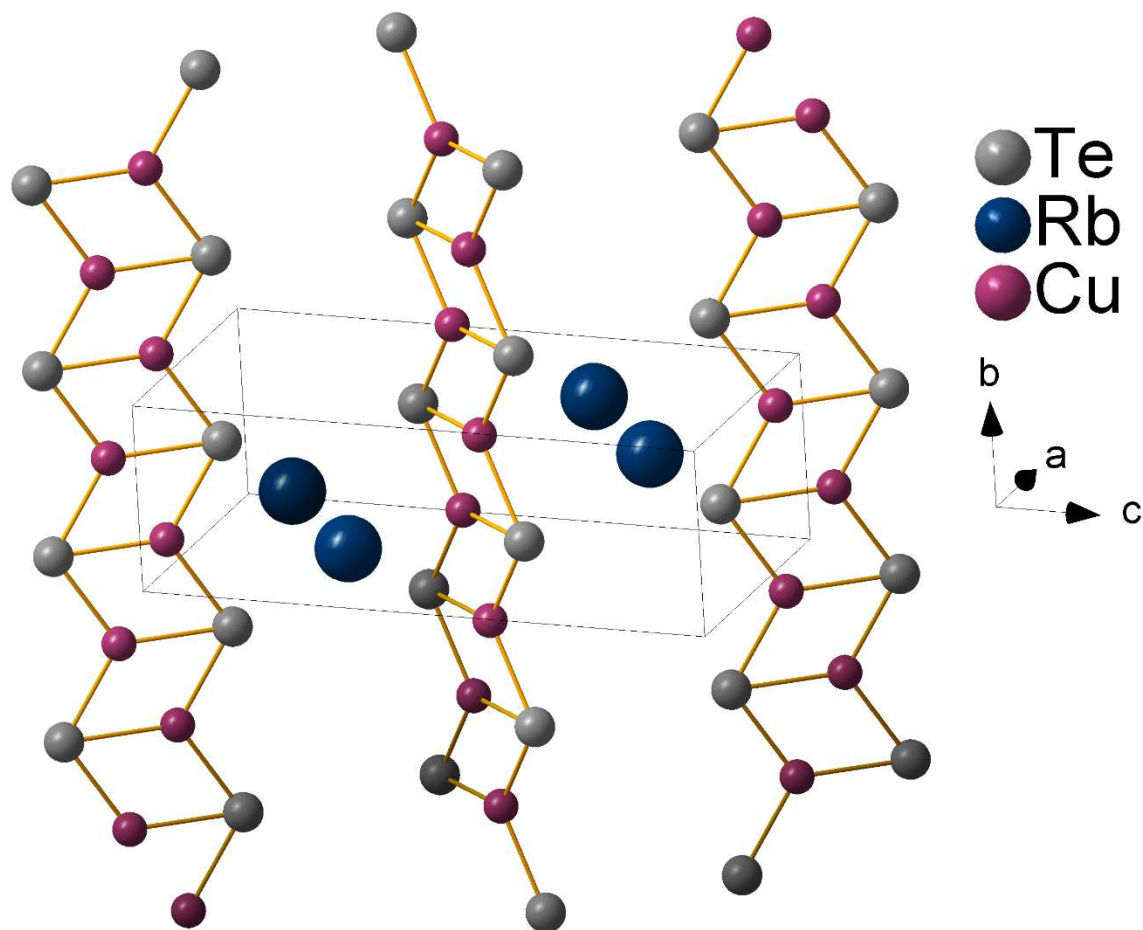


Figure 5. The structure of RbCuTe. There are double chains rather than the single chains seen in the S and Se compounds. The chains are also not parallel but are alternately perpendicular to each other.

Upon finding the empirical structures of RbCuS and RbCuSe to differ from the predicted structures, the models were adapted to better predict the actual structures found. The RbAuS structure is not an ideal, lowest energy structure but one of several local minima for RbCuS and RbCuSe, which is why the original assessment overlooked it. The experimental structures and the predicted structures were “daughter structure types” of the same “formal structure type”.¹ By

considering all the possible daughter structure types equally when determining the structure of a compound, the algorithm can avoid optimizing an unrealistic starting point into an incorrect structure.¹ The new global space group optimization (GSGO) method accurately predicts the correct structures of the two compounds.

6.6 Summary

The structures of RbCuS and RbCuSe were reported for the first time, both in the space group *Cmcm*. Although both compounds are thermally stable as predicted by algorithmic modelling, their structures differ from RbCuTe, whose structure they were predicted to mimic. The high-throughput model was adapted to take an unbiased assessment of all the daughter structure types to find the correct structures for these compounds. This is an example of the kind of mutually helpful feedback loop between experimental synthesis and theoretical modelling. Identification of likely stable phases directs synthetic efforts, and knowledge of empirically determined structures refines modelling algorithms.

Chapter 7: Rocking Curves of Large Single Crystals

7.1 Preface

Rocking curve measurements were performed on several crystals in collaboration with the P. S. Halasyamani group at the University of Houston. The goal of these experiments was to quantify the quality of large single crystals grown in their lab. This chapter is designed to give an overview of the measurement, basic instructions, and a summary of the results to date of the collaboration, in the hopes that it will be helpful to future students who may be unfamiliar with the technique.

7.2 Introduction

Rocking curves, also called ω scans, have a variety of uses in crystallography. Rocking curve measurements are able to quantify the mosaicity of a crystal, along with other defects. For an ideal crystal, the peak width is determined by the width of the source and the geometry of the beam. Real crystals contain dislocation defects, strain, mosaic domains, and point defects which broaden the peak. The full-width half maximum (FWHM) of the rocking curve peak can be compared to the theoretical quality or to other similar samples as a measure of its overall quality. Larger crystals are often more desirable for industrial and commercial applications, as the intensity of optical and electronic properties is often stronger. However, larger crystals are more prone to defects which increase the extinction effects. In addition to single crystal measurements, rocking curves are used by the thin film community to study layer thickness, strain, lattice mismatch, and relaxation, among many other characteristics.

Mosaicity is a concept that traces back to a mathematical model by C. G. Darwin who used it as the basis for an explanation of the differences between theoretical ideal crystals and real (and therefore imperfect) crystals.¹ The term ‘crystal mosaic’ was dubbed by P. P. Ewald.² A simple definition of crystal mosaicity is the degree to which the crystal planes are parallel to one another. The mosaic model of the crystal considers the crystal as consisting of blocks, or mosaic domains, which are slightly tilted relative to one another. This effect is greatly exaggerated in Figure 1, which illustrates the metaphor to tile mosaics that the model is named for. It should be noted that these blocks are not real structures within the crystal, but rather a way of conceptualizing the slight differences in angle between the crystal planes.² The greater the mosaicity, the more domains in the crystal, and therefore the lower quality the crystal.



Figure 1 Mosaic model of a crystal. The tilting of the mosaic domains is exaggerated for clarity.

A schematic of the instrument geometry for rocking curve measurement is shown in Figure 2.³ The incident angle ω is the angle between the x-ray source and the sample. 2θ is the angle between the incident beam and the detector. Rocking curve measurements plot the x-ray intensity as ω is changed. The x-ray diffraction scans that are ordinarily use for sample analysis are a measure of the change in x-ray intensity as 2θ is changed, while ω is held constant. In a rocking curve measurement, the detector is set to a specific Bragg angle and the sample is tilted across a range of ω angles. Even a perfect crystal will have a peak with some width owing to the intrinsic width of the material and the broadening from the instrument itself. For real crystals, a sharp peak represents a high quality crystal with low mosaicity. Broader peaks indicate that the crystal has many defects. Curvature also affects the broadening of the peak, so caution should be exercised when cutting and polishing crystals for analysis.

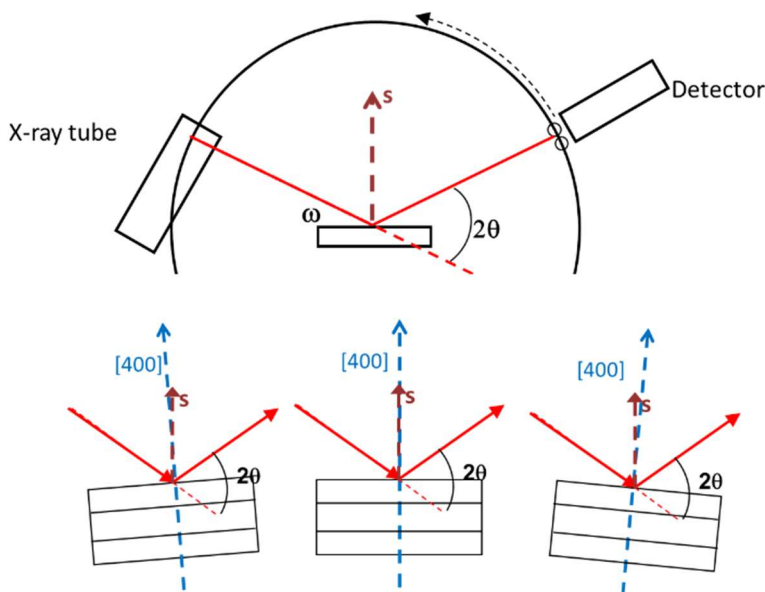


Figure 2: Schematic of rocking curve measurement³

The Advanced Thin film X-ray system – Grazing incidence in-plane diffractometer, or ATX-G, was the instrument used for the rocking curve measurements performed at Northwestern. A diagram of its components is shown in Figure 3. It has a vertical sample stage, to which samples are attached using double sided tape. The ω rotation is the key difference between this system and other x-ray diffraction instruments, which do not include enable this motion. Single crystal diffractometers such as the Bruker KAPPA APEX II can do measure rocking curves, but these are usually only sufficient for a quick analysis of crystal quality before collecting a dataset. If the peaks have a FWHM of 1 or less and do not show splitting (a sign of twinning) then one considers the crystal ‘good’ and moves forward. The ATX-G provides a more holistic look at the crystal and a more precise quantification of its quality. In addition, there are practical upper limits to the size of crystal which can be mounted on traditional single crystal diffractometers. The ATX-G is better suited for large crystals. Single crystals for x-ray crystallography are typically on the order of μm 's whereas the large crystals investigated in the studies at hand were several mm's long on each side.

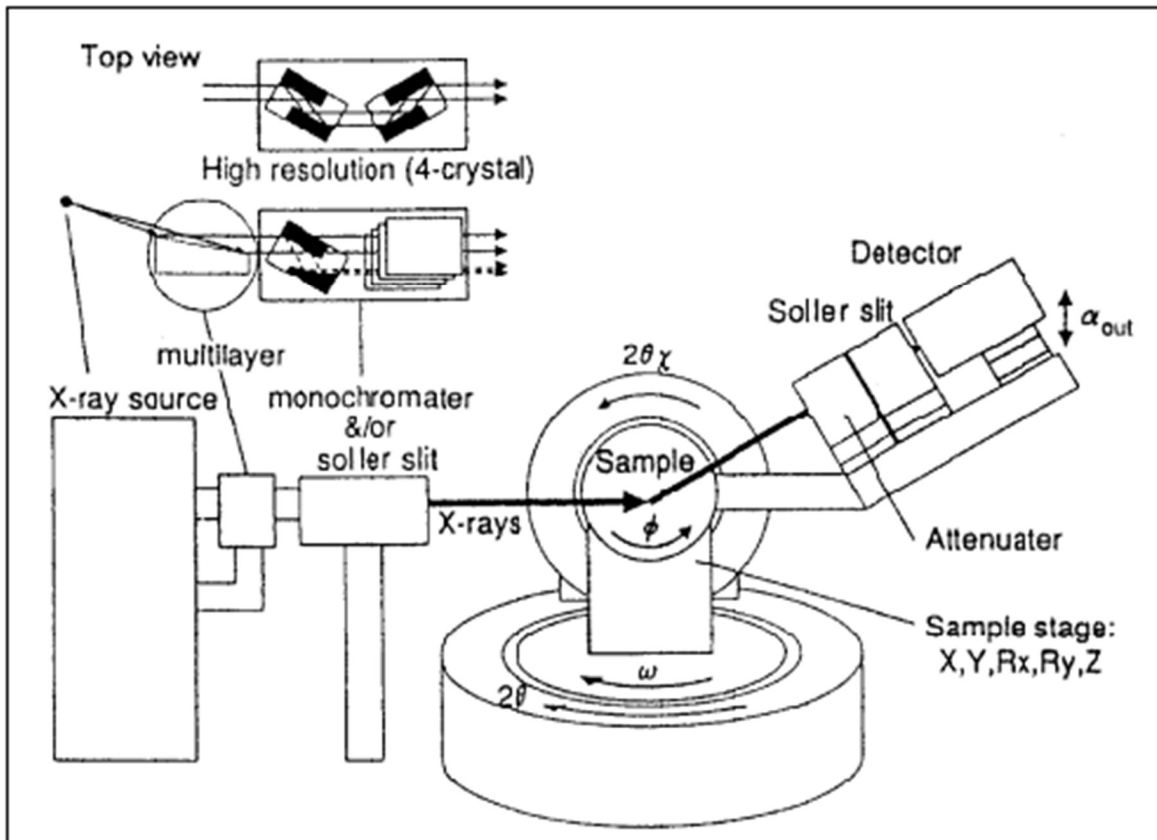


Figure 3: Diagram of ATX-G optical system.⁴

7.3 Instrument Details

The measurements were made on a Rigaku ATX-G with a 4-bounce Ge-220 crystal system, a Cu rotating anode generator ($\lambda = 1.54056 \text{ \AA}$), and a multilayer optic. The $K\alpha_2$ radiation is eliminated by a slit. The rocking curve measurements were made by changing the angle between the X-ray beam and the sample surface (the ω scan) around the Bragg diffraction peak position θ .

7.4 Instructions for rocking curve measurement

Note: the following instructions are specific to the ATX-G system in the Jerome B. Cohen X-ray Diffraction Facility at Northwestern University. Training is required before use.

I. Calibration

Calibrating the instrument is vital to obtaining accurate rocking curves, or even rocking curves at all. If the calibration is off, it is possible to completely miss the sample or to be unable to find the Bragg peak. Under x-ray>monochromator>sample>slits>detector, adjust the slits to $S2_h = 0.1$ mm, $S2_v = 5$ mm, $S3_h = 0.2$ mm, $S3_v = 10$ mm, and $R_h = 0.2$ mm. The instrument should start at 20 kV and 10 mA; ramp up to 50 kV and 240 mA. Check that the correct monochromator is attached. Change the attenuator to 1/800 and uncheck the auto-attenuator. Clicking 'Set' will apply changes.

Set $Z = -3$ mm to move the sample holder out of the beam area. Read position will give the current position and move axis will change the position to the desired value. Set everything else (angles, etc) to 0 using the same method. Choose the 2theta axis; run an absolute scan starting at -0.1 and stopping at 0.1, using width 0.001 deg and scan speed 0.5 deg/min. 'Execute' will begin the run; 'abort' will stop the run. Use the peak finder to find the peak height. For the Ge111 crystal system, the value should be around 1×10^7 cps. The 2theta position should be within 0.01 deg of 0. If it is not, consult an expert.

II. Alignment

In order to measure the rocking curve the sample needs to be in the middle of and parallel to the beam. Move to the 2theta = 0 value that the calibration step found to have a

maximum intensity. Perform an absolute scan of Z from -3mm to 0mm, 0.005 deg, 6mm/min, and move the axis to where the peak finder is at 20% intensity. Perform an absolute scan of Ry from -1mm to 1mm, 0.01 deg, 4 mm/min, and move the axis to the center of the intensity peak. Perform another absolute scan of Z and move the axis to half intensity. Write down the value of the Z axis for reference. More than one alignment step may be required.

III. Measurement

Rocking curve measurements are of a particular Bragg angle; the Bragg angle of a real crystal may deviate slightly from the calculated value, so the peak to be measured must be *found*. Set 2theta to the calculated Bragg angle. Run a relative omega scan from -0.1 to 0.1 deg, 0.001 deg, 0.2 deg/min. It should be further off than that, but if the crystal was cut at an angle or if the crystal face has curvature, it might be really off. The alignment or calibration may be off as well, so consult an expert if you don't find the peak quickly. Move the axis to the center of the peak. Throughout this section, write down each value that an axis is moved to. Run a 2theta relative scan with the same parameters. Move the axis. Repeat this process until you no longer need to move the axis. Run a final, slow omega relative scan from -0.1 to 0.1, width = 0.001 deg, and scan speed 0.2 deg/min (this is pretty much the best this instrument can do and still deliver good results). Once plotted, the FWHM can be found. Remember to bring the instrument power back down to normal so as not to waste energy or burn out the x-ray source.

7.5 Results

All of the crystals discussed in this chapter were grown by the Halasyamani group of the University of Houston, usually using the top-seeded solution growth method, in which a seed crystal is dipped into a melt and then slowly pulled as the melt is cooled. This method can be used to grow comparatively large single crystals, some on the order of centimeters across. The compounds studied in this project are all potential non-linear optical (NLO) materials and crystals of this size are necessary for characterizing NLO properties which often have weak signals. Furthermore, commercial applications often require large crystals, so it is important to consider the ‘practical’ properties of crystals on this scale such as laser damage threshold, thermal properties, and the quality of the crystal. As mentioned earlier, inclusions, poor crystallinity, and other defects can negatively affect the desirable properties of a material. Rocking curves were used to assess the quality of the sample crystals.

The samples studied were $\text{Ba}_3\text{ZnB}_5\text{PO}_{14}$, $\text{Zn}_2\text{TeMoO}_7$, $\text{CaBaZn}_2\text{Fe}_2\text{O}_7$, $\text{Ba}_4\text{B}_{11}\text{O}_{20}\text{F}$, $\text{LiNa}_5\text{Mo}_9\text{O}_{30}$, and $\text{KIO}_3 \cdot \text{Te}(\text{OH})_6$. The rocking curve measurement of each as well as the FWHM is shown in Figure 4. $\text{CaBaZn}_2\text{Fe}_2\text{O}_7$ is clearly of much lower quality than the other crystals, which all have roughly similar FWHMs. In fact, the data collection required a smaller width and faster speed as it became difficult to obtain a well-defined peak with the conditions used for the other samples. Using the smaller width and slower speed resulted in peak splitting. There was not a distinct visible difference between this sample and the others.

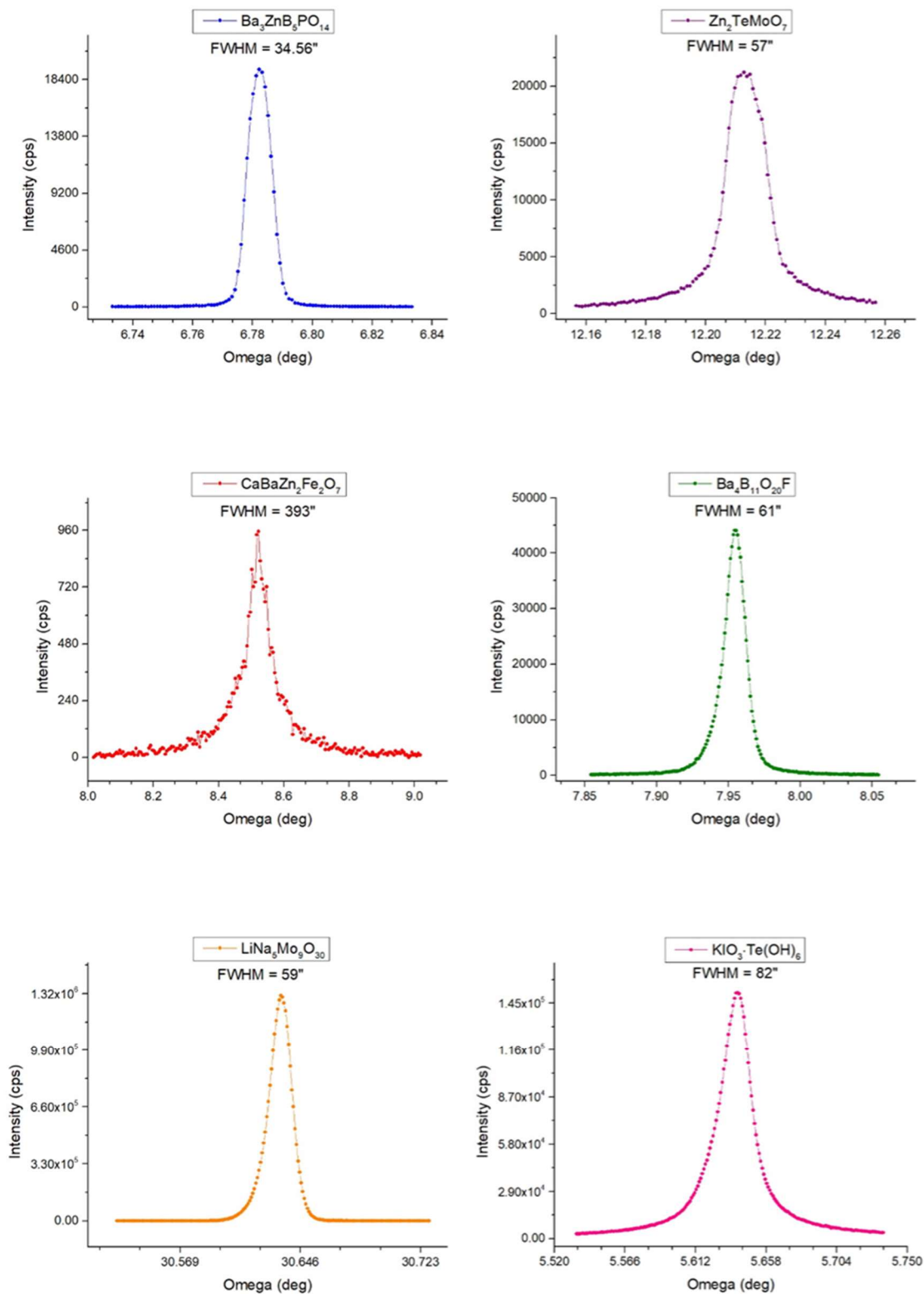


Figure 4 Rocking curves of large single crystal NLO materials with FWHMs labelled

Table 1 summarizes the rocking curve measurements of the samples from the Halasyamani group as well as some found for other NLO materials. The entries in purple (the first six) were measured at Northwestern as part of this study; the others are examples from the literature. $\text{Zn}_2\text{TeMoO}_7$ did not include the rocking curve measurements in the final manuscript. The crystal growth of $\text{CaBaZn}_2\text{Fe}_2\text{O}_7$ has not yet been published, as its structure is already known and the growth process is still undergoing optimization. The crystals have been placed in four categories based on their FWHM: very good ($< 25''$), good ($< 60''$), fair ($< 100''$), and poor ($> 100''$). $\text{Ba}_3\text{ZnB}_5\text{PO}_{14}$ was the best quality crystal measured in this study and compares well to other NLO materials in use. $\alpha\text{-BaTeMo}_2\text{O}_9$ and $\text{Cs}_2\text{TeMo}_3\text{O}_{12}$ have considerably better FWHMs, but of course crystal quality is one of many characteristics to consider. Though $\text{Ba}_4\text{B}_{11}\text{O}_{20}\text{F}$ technically falls in the 'fair' region, it is still well within the range of what would be considered a commercially viable quality.

Compound	Space group	Measured Plane	FWHM (")	Measure Condition		Crystal Quality	Ref
				Width (°)	Speed (°/s)		
Ba ₃ ZnB ₅ PO ₁₄	Pmn2 ₁	(101)	35	0.001	0.2	good	5
Zn ₂ TeMoO ₇	P2 ₁	(020)	57	0.001	0.2	good	6
CaBaZn ₂ Fe ₂ O ₇	P6 ₃ mc	(002)	393	0.01	2	poor	n/a
Ba ₄ B ₁₁ O ₂₀ F	Cmc2 ₁	(010)	61	0.001	0.2	fair	7
LiNa ₅ Mo ₉ O ₃₀	Fdd2	(001)	59	0.001	0.2	good	8
KIO ₃ ·Te(OH) ₆	Pna2 ₁	(010)	82	0.001	0.2	fair	9
Si	Fd3-m	(111)	21	0.001	0.2	very good	n/a
Cs ₂ TeW ₃ O ₁₂	P6 ₃	(002)	33	0.0005	0.0005	good	10
MnTeMoO ₆	P2 ₁ 2 ₁ 2	(110)	472	Not given	Not given	poor	11
KBe ₂ BO ₃ F ₂	R32	(001)	25	Not given	Not given	very good	12
CdSiP ₂	I4-2d	(200)	33	Not given	Not given	good	13
α-BaTeMo ₂ O ₉	Pca2 ₁	(400)	16.55	0.0005	0.0005	very good	14
Cs ₂ TeMo ₃ O ₁₂	P6 ₃	(002)	18.96	0.0005	0.0005	very good	15

Table 1. Rocking curve measurements: comparison of NLO samples

As a comparison point, a standard silicon (111) wafer was also measured. This crystal is kept in the x-ray diffraction facility as a calibration standard; its origins are no longer known. The rocking curve is shown below (Figure 5). Its FWHM of 20.9'' is clearly much better than the laboratory-grown crystals measured. One aspect that should be considered in light of this is the importance of obtaining a perfectly flat crystal face that is exactly parallel to the lattice. Since the crystal samples that were measured were cut and polished for analysis, it is possible that the faces were slightly angled or had some small amount of curvature which would broaden the rocking curve peak. The measured 2θ position for $\text{Ba}_4\text{B}_{11}\text{O}_{20}\text{F}$ was off by 0.2° from the calculated Bragg angle, for example. This material has a high hardness value and therefore it is possible that when it was polished a slight deviation from true normal was introduced, affecting not only the 2θ peak position but also adding to the width of the rocking curve peak.

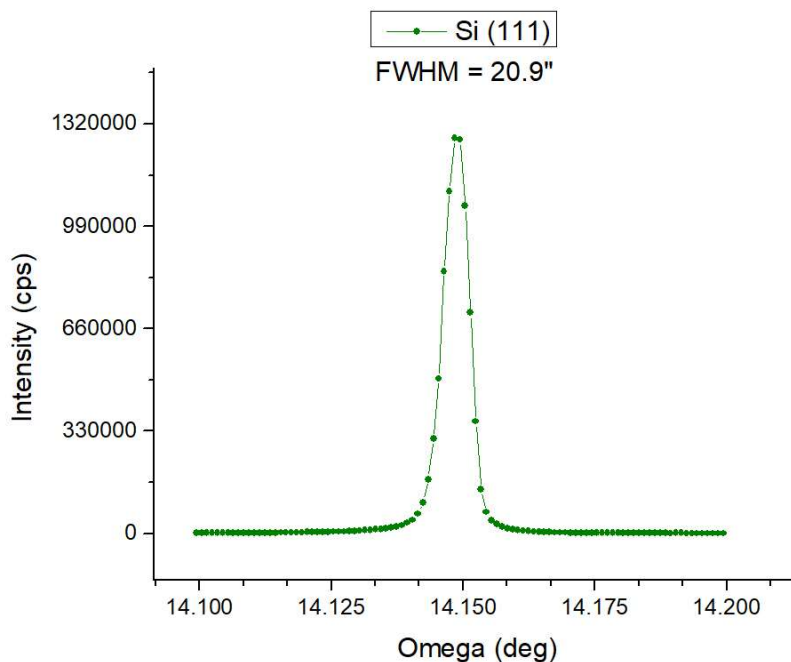


Figure 5: Rocking curve of Si(111) crystal

7.6 Summary

Six compounds were analyzed for crystal quality using rocking curve measurements. The ATX-G at the J. B. Cohen X-ray Diffraction Facility was used for the experiments. Although most of the crystals showed reasonable crystal quality, $\text{Ba}_3\text{ZnB}_5\text{PO}_{14}$ was the best of the samples measured, as determined by FWHM. $\text{CaBaZn}_2\text{Fe}_2\text{O}_7$ was the only crystal whose quality was not of an acceptable standard. As such, attempts at optimizing its growth conditions are on-going. These results show that these NLO-active materials have potential in commercial applications.

Chapter 8: Conclusions and Future Directions

Discovery and targeted synthesis of NCS materials remains an important goal for inorganic chemistry owing to the desirability of the symmetry-dependent physical properties of piezoelectricity, pyroelectricity, and nonlinear optical properties such as second harmonic generation which have numerous commercial applications. The strategy of using oxyfluoride metal complexes as BBUs for NCS materials has been used successfully, though forming NCS BBUs does not always lead to a NCS structure. Understanding more of the structural characteristics and interactions between groups within structures, both NCS and CS, adds to the knowledge of how to successfully design and synthesis NCS materials.

$\text{CuVOF}_4(\text{H}_2\text{O})_7$ is a NCS material with several related CS heterotypes. The key features of $\text{CuVOF}_4(\text{H}_2\text{O})_7$ that set it apart from these family members, are the bridging oxygen between the Cu and V octahedra and the presence of a free water molecule in the compound. These two features allow the Cu and V octahedra to form a bent Λ -shaped dimer which stacks noncentrosymmetrically. Previous studies using x-ray crystallography focused on the intra-dimer hydrogen bonding. As the shortest (and ergo strongest) hydrogen bond in that solution, it was identified as the most impactful in the formation and stabilization of the bent Λ -shape of the dimer. However, the refinement of the hydrogen positions using solely x-ray diffraction left some questions unanswered. A co-refinement of single crystal x-ray and neutron diffraction was used to create a holistic structure solution through which to study the hydrogen bonding in $\text{CuVOF}_4(\text{H}_2\text{O})_7$. The hydrogen positions found frequently deviated greatly from what was determined using x-ray diffraction alone, both in terms of bond length and spatial position. Most

interestingly, the hydrogen bonds between the free water molecule and the dimer were stronger than the intra-dimer hydrogen bond. This suggests that these interactions are actually much more important to the NCS of the structure than previously realized.

The importance of hydrogen bonding in the formation of NCS structures should not be overlooked and further research into the effects of hydrogen bonds could reveal new insights into its role in NCS materials. It is not practical to obtain neutron diffraction for every hydrogen-containing structure, but it is also frequently unnecessary. DFT is able to locate and refine hydrogen atoms at a comparable accuracy, and provides a convenient, low-cost replacement. More knowledge is needed to reach a point where hydrogen bonding can be deliberately used towards crystal engineering. There are still many as yet unknown compounds in the $\text{MVOF}_4(\text{H}_2\text{O})_7$ system that could be synthesized and studied.

Two new pleochroic compounds were discovered: $\text{CuMnF}_5(\text{H}_2\text{O})_7$ and KNaMnF_5 . $\text{CuMnF}_5(\text{H}_2\text{O})_7$ had been previously reported without a structure solution, but was assumed to share the same structure type ($\text{CoAlF}_5(\text{H}_2\text{O})_7$) as its synthetic kin, $\text{NiMnF}_5(\text{H}_2\text{O})_7$. $\text{CoAlF}_5(\text{H}_2\text{O})_7$ has a structure related to the centrosymmetric $\text{MVOF}_5(\text{H}_2\text{O})_7$ structures. However, single crystal x-ray diffraction showed that while $\text{CuMnF}_5(\text{H}_2\text{O})_7$ forms similar ionic octahedral groups to $\text{CoAlF}_5(\text{H}_2\text{O})_7$, their arrangement is very different. The arrangement of the BBUs of $\text{CuMnF}_5(\text{H}_2\text{O})_7$ actually has more in common with the layout of $\text{CuVOF}_4(\text{H}_2\text{O})_7$, though of course the octahedra are not connected through a bond. KNaMnF_5 is the first $\text{AA}'\text{MnF}_5$ member of the large $\text{A}^{(I)}_2\text{MnF}_5 \cdot x\text{H}_2\text{O}$ ($x = 0,1$) family, which has been extensively studied. Its structure mirrors that of isotypes with similarly sized cations. It would be interesting to attempt to synthesize oxyfluoride analogues of these two compounds to see how that would affect the

structure. The mixture of oxide and fluoride ligands might be enough to push $\text{CuMnF}_5(\text{H}_2\text{O})_7$ towards the $\text{CuVOF}_4(\text{H}_2\text{O})_7$ structure.

Pleochroism is not uncommon among inorganic compounds, though it is usually undetectable by eye. The dramatic pleochroism of $\text{CuMnF}_5(\text{H}_2\text{O})_7$ and KNaMnF_5 is much more rare; $\text{CuMnF}_5(\text{H}_2\text{O})_7$ changes from red to green and KNaMnF_5 from red to orange. The pleochroism of both compounds were examined through optical absorption measurements. The plates of $\text{CuMnF}_5(\text{H}_2\text{O})_7$ were too thin to be measured on all but the flat face, which showed two absorption peaks which alternate with every 90° of polarization, directly corresponding to the observed color changes. KNaMnF_5 shows similar spectra for two faces, but a third face shows two peaks which occur in parallel. Further studies are needed to better understand the relationship between the optical absorption and the crystal structure.

NTE materials are used for many commercial applications that involve high-precision electronic and optical components where it is necessary to dampen the PTE of components to the greatest extent possible. Thermocrystallography experiments were conducted on the compound KNaNbOF_5 , a PTE material, to investigate the thermal expansion effects on atomic positions and bond lengths. The volumetric thermal expansion coefficient of KNaNbOF_5 is $4.38 \times 10^{-5} \text{ K}^{-1}$. While the K^+ ions predictably displayed PTE, the octahedral NbOF_5 units were not as conclusive. This shows that the thermal expansion of individual bonds does not necessarily follow the trends of the unit cell as a whole, which has important implications for the understanding of NTE materials and their synthesis. The compounds $\text{KNaMoO}_2\text{F}_4$ and KNaWO_2F_4 which have structures related to KNaNbOF_5 and which are predicted to have similar phase transitions, would make an interesting comparison study. $\text{Cd}(3\text{-apy})_4\text{-NbOF}_5$ would be a

good candidate for examining the thermal expansion properties of the NbOF₅ group more broadly. Such studies could contribute to better modelling of thermal effects in crystal structures.

As part of joint effort between theoretical and synthetic research groups, a series of 8-electron ABX compounds were first modelled to predict structural stability. Two such previously unreported but predicted stable compounds, RbCuS and RbCuSe, were both synthesized and found to crystallize in the space group *Cmcm*. Modelling predicted their structures would be related to RbCuTe, but this was not the case. The high-throughput model was adapted to take an unbiased assessment of all the daughter structure types to find the correct structures for these compounds. This is an example of the kind of mutually helpful feedback loop between experimental synthesis and theoretical modelling. Identification of likely stable phases directed synthetic efforts, and knowledge of empirically determined structures refined the modelling algorithms.

In collaboration with the Halasyamani group of the University of Houston, the rocking curves were measured for several large single crystals as a quantitative assessment of their quality. Although most of the crystals showed reasonably good crystal quality, Ba₃ZnB₅PO₁₄ was the best of the samples measured, with a FWHM of 35". CaBaZn₂Fe₂O₇ was the only crystal whose quality was not of an acceptable standard for commercial applications, and because of this is still undergoing growth optimization. This technique could be applied to the large single crystals grown using the Optical Floating Zone furnaces to quantify the crystal quality of the samples. This would provide a method of investigating the effects of different growth conditions more minutely.

References

Chapter 1

1. Halasyamani, P. S.; Poeppelmeier, K. R. "Noncentrosymmetric oxides" *Chem. Mater.* **1998**, *10*, 2753.
2. Hollingsworth, M. D. "Crystal engineering: from structure to function". *Science*. **2002**, *295*, 2410.
3. Bloembergen, N.; Pershan, P. S. "Light waves at the boundary of nonlinear media". *Phys Rev* **1962**, *128*, 606-622.
4. Lu, H.; Gautier, R.; Donakowski, M. D.; Tran, T. T.; Edwards, B. W.; Nino, J. C.; Halasyamani, P. S.; Liu, Z.; Poeppelmeier, K. R. "Nonlinear active materials: an illustration of controllable phase matchability". *J. Amer. Chem. Soc.* **2013**, *135*, 11942-11950.
5. Ye, N.; Chen, Q.; Wu, B.; Chen, C. "Searching for new nonlinear optical materials on the basis of the anionic group theory". *J Appl Phys* **1998**, *84*, 555-558.
6. Abrahams, S. C.; Reddy, J. M.; Bernstein, J. L. "Ferroelectric lithium niobate. 3. Single crystal x-ray diffraction study at 24 °C". *J. Phys. Chem. Solids*. **1966**, *27*, 997.
7. Holland, M.; Donakowski, M. D.; Pozzi, E. A.; Rasmussen, A. M.; Tran, T. T.; Pease-Dodson, S. E.; Halasyamani, P. S.; Seideman, T.; Van Duyne, R. P.; Poeppelmeier, K. R. "Polar Alignment of Λ -Shaped Basic Building Units within Transition Metal Oxide Fluoride Materials" *Inorg Chem.* **2014**, *53*, 221.

8. Donakowski, M. D.; Gautier, R.; Yeon, J.; Moore, D. T.; Nino, J. C.; Halasyamani, P. S.; Poeppelmeier, K. R. "The role of polar, lambda-shaped building units in noncentrosymmetric inorganic structures" *J. Am. Chem. Soc.* **2012**, *134*, 7679.
9. Gautier, R.; Donakowski, M. D.; Poeppelmeier, K. R. "Orientational Order of $[\text{VOF}_5]^{2-}$ and $[\text{NbOF}_5]^{2-}$ Polar Units in Chains" *J. Solid State Chem.* **2012**, *195*, 132.
10. Pinlac, R. A. F.; Stern, C. L.; Poeppelmeier, K. R. "New Layered Oxide-Fluoride Perovskites: KNaNbOF_5 and KNaMO_2F_4 ($M = \text{Mo}^{6+}$, W^{6+})" *Crystals* **2011**, *1*, 3.
11. Chang, K. B.; Vinokur, A.; Pinlac, R. A. F.; Suchomel, M. R.; Marvel, M. R.; Poeppelmeier, K. R. "How Lewis Acidity of the Cationic Framework Affects KNaNbOF_5 " *Inorg. Chem.* **2014**, *53*, 6979.
12. Kageyama, H.; Hayashi, K.; Maeda, K.; Attfield, J. P.; Hiroi, Z.; Rondinelli, J. M.; Poeppelmeier, K. R. "Expanding frontiers in materials chemistry and physics with multiple anions" *Nat Comm.* **2018**, *9*, 772.
13. Yamanaka, S. "Intercalation of superconductivity in ternary layer structured metal nitride halides ($M\text{NX}$: $M = \text{Ti, Zr, Hf}$; $X = \text{Cl, Br, I}$)". *J. Mater. Chem.* **2010**, *20*, 2922.
14. Yajima, T.; Koshiko, M.; Zhang, Y.; Oguchi, T.; Yu, W.; Kato, D.; Kobayashi, Y.; Orikasa, Y.; Yamamoto, T.; Uchimoto, Y.; Green, M.; Kageyama, H. "Selective and low temperature transition metal intercalation in layered tellurides". *Nat Comm* **2016**, *7*, 13809.
15. Lingampalli, S. R., Manjunath, K., Shenoy, S., Waghmare, U. V.; Rao, C. N. R. "Zn₂NF and related analogues of ZnO." *J. Am. Chem. Soc.* **2016**, *138*, 8228.

16. Sathiya, M.; Rouse, G.; Ramesha, K.; Laisa, C. P.; Vezin, H.; Sougrati, M. T.; Doublet, M-L.; Foix, D.; Gonbeau, D.; Walker, W.; Prakash, A. S.; Hassine, M. B.; Dupont, L.; Tarascon, J-M. "Reversible anionic redox chemistry in high-capacity layered oxide electrodes". *Nat Mat* **2013**, *12*, 827.
17. Maggard, P. A.; Stern, C. L.; Poeppelmeier, K. R. "Understanding the Role of Helical Chains in the Formation of Noncentrosymmetric Solids." *Journal of the American Chemical Society* **2001**, *123*, 7742-7743.
18. Maggard, P. A.; Nault, T. S.; Stern, C. L.; Poeppelmeier, K. R. "Alignment of acentric $[\text{MoO}_3\text{F}_3]^{3-}$ anions in a polar material: $(\text{Ag}_3\text{MoO}_3\text{F}_3)(\text{Ag}_3\text{MoO}_4)\text{Cl}$." *Journal of Solid State Chemistry* **2003**, *175*, 27-33.
19. Pearson, R. G. "Hard and soft acids and bases." *J. Amer Chem Soc.* **1963**, *85*, 3533.
20. Parr, R. G.; Pearson, R. G. "Absolute hardness: companion parameter to absolute electronegativity". *J Amer Chem Soc*, **1983**, *105*, 7512.
21. Donakowski, M. D.; Görne, A.; Vaughey, J. T.; Poeppelmeier, K. R. "AgNa(VO₂F₂)₂: A Trioxovanadium Fluoride with Unconventional Electrochemical Properties" *J Amer Chem Soc*, **2013**, *135*, 9898.
22. Latimer, W. M.; Rodebush, W. H. "Polarity and ionization from the standpoint of the Lewis theory of valence". *J Am Chem Soc.* **1920**, *42*, 1419.
23. Hamilton, W. C.; Ibers, J. A. *Hydrogen Bonding in Solids: Methods of Molecular Structure Determination*. W. A. Benjamin, Inc., New York, **1968**.
24. Jablonski, M.; Paluciak, M. "Divalent carbon atom as the proton acceptor in hydrogen bonding". *Phys. Chem. Chem. Phys.* **2009**, *11*, 5711.

25. Hodgkinson, P.; Widdifield, C. M. "Perspectives: In crystallography we trust". *C&EN*. **2016**, *94*, 30.
26. Sears, V. F. "Neutron scattering lengths and cross sections" *Neutron News* **1992**, *3*, 29-37.
27. Deringer, V. L.; George, J.; Dronskowski, R.; Englert, U. "Plane-Wave Density Functional Theory meets molecular crystals: thermal ellipsoids and intermolecular interactions" *Accts. Chem. Res.* **2017**, *50*, 1231-1239.
28. Deringer, V. L.; Hoepfner, V.; Dronskowski, R. "Accurate hydrogen positions in organic crystals: assessing a quantum-chemical aide" *Cryst. Growth Des.* **2012**, *12*, 1014-1021.
29. Woinska, M.; Grabowsky, S.; Dominiak, P. M.; Wozniak, K.; Jayatilaka, D. "Hydrogen atoms can be located accurately and precisely by x-ray crystallography". *Sci. Adv.* **2016**, *2*, e1600192.
30. Rabeneau, A. "The role of hydrothermal synthesis in preparative chemistry". *Angew. Chem. Int. Ed.* **1985**, *24*, 1026.
31. Tressaud, A.; Poepfelmeier, K. R. *Photonic and Electronic Properties of Fluoride Materials: Progress in Fluorine Science Series*. Elsevier, Amsterdam, **2016**.
32. Harrison, W. T. A.; Nenoff, T. M.; Gier, T. E.; Stucky, G. D. "Tetrahedral-atom 3-ring groupings in 1-dimensional inorganic chains: beryllium arsenate hydroxide hydrate ($\text{Be}_2\text{AsO}_4\text{OH}\cdot 4\text{H}_2\text{O}$) and sodium zinc hydroxide phosphate hydrate ($\text{Na}_2\text{ZnPO}_4\text{OH}\cdot 7\text{H}_2\text{O}$)." *Inorg Chem* **1993**, *32*, 2437.
33. Bertolini, J. C. "Hydrofluoric acid: a review of toxicity" *J. Emerg. Med.* **1991**, *10*, 163.

34. Peters, D.; Miethchen, R. "Symptoms and treatment of hydrogen fluoride injuries" *J. Fluorine Chem.* **1996**, *79*, 161.
35. Segal, E. B. "First aid for a unique acid, HF: a sequel" *Chem. Health Saf.* **2000**, *7*, 18.
36. *Parr Acid Digestion Vessels: Operating Instruction Manual*. Parr Instrument Company, No. 249M, revision 3/23/10.

Chapter 2

1. Lippman, G. "Principe de la conservation de l'electricite" *Ann. Chim. Phys.* **1881**, *24*, 145.
2. Valasek, J. "Piezoelectric and allied phenomena in rochelle salt" *Phys. Rev.* **1920**, *15*, 537.
3. Franken, P. A.; Hill, A. E.; Peters, C. W.; Weinreich, G. "Generation of optical harmonics" *Phys. Rev. Lett.* **1961**, *7*, 118.
4. Donakowski, M. D.; Gautier, R.; Yeon, J.; Moore, D. T.; Nino, J. C.; Halasyamani, P. S.; Poepelmeier, K. R. "The role of polar, lambda-shaped building units in noncentrosymmetric inorganic structures" *J. Am. Chem. Soc.* **2012**, *134*, 7679 – 7689.
5. Sears, V. F. "Neutron scattering lengths and cross sections" *Neutron News* **1992**, *3*, 29-37.
6. Deringer, V. L.; George, J.; Dronskowski, R.; Englert, U. "Plane-Wave Density Functional Theory meets molecular crystals: thermal ellipsoids and intermolecular interactions" *Accts. Chem. Res.* **2017**, *50*, 1231-1239.

7. Deringer, V. L.; Hoepfner, V.; Dronskowski, R. "Accurate hydrogen positions in organic crystals: assessing a quantum-chemical aide" *Cryst. Growth Des.* **2012**, *12*, 1014-1021.
8. Lee, J-H.; Bristowe, N. C.; Bristowe, P. D.; Cheetham, A. K. "Role of hydrogen-bonding and its interplay with octahedral tilting in $\text{CH}_3\text{NH}_3\text{PbI}_3$ " *Chem. Commun.* **2015**, *51*, 6434-6437.
9. Lebernegg, S.; Tsirlin, A. A.; Janson, O.; Rosner, H. "Spin gap in malachite $\text{Cu}_2(\text{OH})_2\text{CO}_3$ and its evolution under pressure" *Phys. Rev. B* **2013**, *88*, 224406.
10. Lebernegg, S.; Tsirlin, A.A.; Janson, O.; Rosner, H. "Two energy scales of spin dimers in clinoclase $\text{Cu}_3(\text{AsO}_4)(\text{OH})_3$ " *Phys. Rev. B* **2013**, *87*, 235117.
11. 7.23A ed.; Bruker Analytical X-ray Instruments, Inc.; Madison, WI, 2005.
12. Sheldrick, G. M.; Bruker Analytical X-ray Instruments, Inc.; Madison, WI, 1997.
13. Altomare, A.; Burla, M. C.; Camalli, M.; Cascarano, G. L.; Giacovazzo, C.; Guagliardi, A.; Moliterni, A. G. G.; Polidori, G.; Spagna, R. "SIR97: a new tool for crystal structure determination and refinement" *J. Appl. Crystallogr.* **1999**, *32*, 115.
14. Farrugia, L. J. "WinGX suite for small-molecule single-crystal crystallography" *J. Appl. Crystallogr.* **1999**, *32*, 837.
15. Sheldrick, G. "A short history of SHELX" *Acta Crystallogr., Sect. A* **2008**, *64*, 112.
16. Rodriguez-Carvajal, J. "Recent advances in magnetic structure determination by neutron powder diffraction" *Phys B.* **1993**, *192*, 55.
17. Roisnel, T.; Rodriguez-Carvajal, J. "WinPLOTR: a Windows tool for powder diffraction patterns analysis Materials Science Forum" *Proc. of the Seventh Euro. Powder Diff. Conf.* **2000**, 118.

18. Woinska, M.; Grabowsky, S.; Dominiak, P. M.; Wozniak, K.; Jayatilaka, D. "Hydrogen atoms can be located accurately and precisely by x-ray crystallography". *Sci. Adv.* **2016**, *2*, e1600192.
19. Hamilton, W. C.; Ibers, J. A. *Hydrogen Bonding in Solids: Methods of Molecular Structure Determination*. W. A. Benjamin, Inc., New York, **1968**.

Chapter 3

1. Nunez, P.; Tressaud, A.; Darriet, J.; Hagenmuller, P.; Massa, W.; Kummer, S.; Babel, D. "On new hydrated fluorides of trivalent manganese". *J Solid State Chem* **1988**, *77*, 240.
2. Massa, W. "Structural studies on some fluoromanganates(III)" *J Fluorine Chem* **1980**, *16*, 634.
3. Donakowski, M. D.; Gautier, R.; Yeon, J.; Moore, D. T.; Nino, J. C.; Halasyamani, P. S.; Poepelmeier, K. R. "The role of polar, lambda-shaped building units in noncentrosymmetric inorganic structures" *J. Am. Chem. Soc.* **2012**, *134*, 7679 – 7689.
4. Felder, J. B.; Yeon, J.; Smith, M. D.; zur Loye, H.-C. "Compositional and Structural Versatility in an Unusual Family of *anti*-Perovskite Fluorides: [Cu(H₂O)₄]₃[(MF₆)(M'F₆)]". *Inorg Chem* **2016**, *55*, 7167.
5. Nassau, K. *The Physics and Chemistry of Color: The Fifteen Causes of Color*. **2001**. 2nd Ed. John Wiley & Sons, Inc., New York.
6. Bertolini, J. C. "Hydrofluoric acid: a review of toxicity" *J. Emerg. Med.* **1991**, *10*, 163.

7. Peters, D.; Miethchen, R. "Symptoms and treatment of hydrogen fluoride injuries" *J. Fluorine Chem.* **1996**, *79*, 161.
8. Segal, E. B. "First aid for a unique acid, HF: a sequel" *Chem. Health Saf.* **2000**, *7*, 18.
9. Harrison, W. T. A.; Nenoff, T. M.; Gier, T. E.; Stucky, G. D. "Tetrahedral-atom 3-ring groupings in 1-dimensional inorganic chains: beryllium arsenate hydroxide hydrate ($\text{Na}_2\text{ZnPO}_4\text{OH}\cdot 4\text{H}_2\text{O}$) and sodium zinc hydroxide phosphate hydrate ($\text{Na}_2\text{ZnPO}_4\text{OH}\cdot 7\text{H}_2\text{O}$)" *Inorg. Chem.* **1993**, *32*, 2437.
10. 8.34A ed.; Bruker Analytical X-ray Instruments, Inc.; Madison, WI, 2005.
11. Bruker (2001). *SADABS*. Bruker AXS Inc., Madison, Wisconsin, USA.
12. Altomare, A.; Burla, M. C.; Camalli, M.; Cascarano, G. L.; Giacovazzo, C.; Guagliardi, A.; Moliterni, A. G. G.; Polidori, G.; Spagna, R. "SIR97: a new tool for crystal structure determination and refinement" *J. Appl. Crystallogr.* **1999**, *32*, 115.
13. Sheldrick, G. M. *Acta Cryst.* **2015**, *C71*, 3-8.
14. Sheldrick, G. M. *Acta Cryst.* **2015**, *A71*, 3-8.

Chapter 4

1. Massa, W. "Struktur von Natrium-pentafluoromanganat(III)" *Acta Cryst.* **1986**, *C42*, 644.
2. Roisnel, T.; Nunez, P.; Tressaud, A.; Molins, E.; Rodriguez-Carvajal, J. "Investigation of $\text{K}_2\text{MnF}_5\cdot\text{H}_2\text{O}$ by Neutron Diffraction" *J. Solid State Chem.* **2000**, *150*, 104.
3. Pebler, J.; Massa, W.; Lass, H.; Ziegler, B. "Intrachain exchange energies in 1-dimensional magnetic fluoromanganates(III) as a function of Mn-F-Mn bridge angle and

- crystal structure of Li_2MnF_5 ” *J. Solid State Chem.* **1987**, 71, 87.
4. Palacia, F.; Andres, M.; Esteban-Calderon, C.; Martinez-Ripoll, M.; Gracia-Blanco, S. “Crystal structure and magnetic properties of linear chain potassium aquotetrafluoromanganate(III)” *J. Solid State Chem.* **1988**, 76, 33.
 5. Nunez, P.; Darriet, J.; Bukovec, P.; Tressaud, A.; Hagemuller, P. “Etude magnetique de fluorures a chaines a base de manganese (III)” *Mat. Res. Bull.* **1987**, 22, 661.
 6. Massa, W.; Burk, V. “Erdalkali-Fluoromanganate(III): $\text{BaMnF}_5 \cdot \text{H}_2\text{O}$ und $\text{SrMnF}_5 \cdot \text{H}_2\text{O}$ ” *Z. Anorg. Allg. Chem.*, **1984**, 516, 119.
 7. Nunez, P.; Tressaud, A.; Massa, W.; Babel, D.; Boireau, A.; Soubeyroux, J. L. “A new 1D-antiferromagnet: Crystal and magnetic structures of $\text{TlMnF}_4 \cdot \text{H}_2\text{O}$ ” *Phys. Status Solidi* **1991**, A127, 505.
 8. Sears, D. R.; Hoard, J. L. “Crystal Structure of $(\text{NH}_4)_2\text{MnF}_5$ ” *J Chem Phys* **1969**, 50, 1066.
 9. Molinier, M.; Frommen, C.; Massa, W.; Pebler, J.; Roisnel, T. “Magnetism of Alkalitetrafluoromanganates (III) AMnF_4 (A = K, Rb, Cs): Neutron Diffraction, Mössbauer and Magnetization Investigations” *Z. Naturf.* **1993**, 48a, 1054.
 10. Rodriguez, F.; Nunez, P.; Marco de Lucas, M. C. “Polarized Optical Absorption Spectroscopy of the $\text{Tl}_2\text{MnF}_5 \cdot \text{H}_2\text{O}$ 1D Manganese (III) Single Crystal” *J. Solid State Chem* **1994**, 110, 370.
 11. Bertolini, J. C. “Hydrofluoric acid: a review of toxicity” *J. Emerg. Med.* **1991**, 10, 163.
 12. Peters, D.; Miethchen, R. “Symptoms and treatment of hydrogen fluoride injuries” *J. Fluorine Chem.* **1996**, 79, 161.

13. Segal, E. B. "First aid for a unique acid, HF: a sequel" *Chem, Health Saf.* **2000**, 7, 18.
14. Harrison, W. T. A.; Nenoff, T. M.; Gier, T. E.; Stucky, G. D. "Tetrahedral-atom 3-ring groupings in 1-dimensional inorganic chains: beryllium arsenate hydroxide hydrate ($\text{Na}_2\text{ZnPO}_4\text{OH}\cdot 4\text{H}_2\text{O}$) and sodium zinc hydroxide phosphate hydrate ($\text{Na}_2\text{ZnPO}_4\text{OH}\cdot 7\text{H}_2\text{O}$)" *Inorg. Chem.* **1993**, 32, 2437.
15. 8.37A ed.; Bruker Analytical X-ray Instruments, Inc.; Madison, WI, 2005.
16. Bruker (2001). *SADABS*. Bruker AXS Inc., Madison, Wisconsin, USA.
17. Altomare, A.; Burla, M. C.; Camalli, M.; Casciarano, G. L.; Giacovazzo, C.; Guagliardi, A.; Moliterni, A. G. G.; Polidori, G.; Spagna, R. "SIR97: a new tool for crystal structure determination and refinement" *J. Appl. Crystallogr.* **1999**, 32, 115.
18. Farrugia, L. J. "WinGX suite for small-molecule single-crystal crystallography" *J. Appl. Crystallogr.* **1999**, 32, 837.
19. Sheldrick, G. "A short history of SHELX" *Acta Crystallogr., Sect. A* **2008**, 64, 112.
20. Nassau, K. *The Physics and Chemistry of Color: The Fifteen Causes of Color*. **2001**. 2nd Ed. John Wiley & Sons, Inc., New York.

Chapter 5

1. Marvel, M. R.; Lesage, J.; Baek, J.; Halasyamani, P. S.; Stern, C. L.; Poeppelemeier, K. R. "Cation-Anion Interactions and Polar Structures in the Solid State" *J. Am. Chem. Soc.* **2007**, 129, 13963.

2. Chang, K.B.; Edwards, B. W.; Frazer, L.; Lenferink, E. J.; Stanev, T. K.; Stern, N. P.; Nino, J. C.; Poeppelmeier, K. R. "Hydrothermal crystal growth, piezoelectricity, and triboluminescence of KNaNbOF_5 " *J Solid State Chem* **2016**, *236*, 78.
3. Pinlac, R. A. F.; Stern, C. L.; Poeppelmeier, K. R. "New Layered Oxide-Fluoride Perovskites: KNaNbOF_5 and KNaMO_2F_4 ($M = \text{Mo}^{6+}$, W^{6+})" *Crystals* **2011**, *1*, 3.
4. Chang, K. B.; Vinokur, A.; Pinlac, R. A. F.; Suchomel, M. R.; Marvel, M. R.; Poeppelmeier, K. R. "How Lewis Acidity of the Cationic Framework Affects KNaNbOF_5 Polymorphism" *Inorg Chem* **2014**, *53*, 6979.
5. Antokhina, T. F.; Ignat'eva, L. N.; Savchenko, N. N.; Tkachenko, I. A.; Kaidalova, T. A. "Synthesis and physicochemical properties of new niobium fluoro complexes with mixed alkali-metal cations" *Zh. Neorg. Khim.* **2003**, *48*, 551.
6. Vasiliev, A. D.; Laptash, N. M. "Polymorphism of KNaNbOF_5 crystals" *J. Struct. Chem.* **2012**, *53*, 902.
7. Holland, M.; Charles, N.; Rondinelli, J. M.; Poeppelmeier, K. R. "Reconstructive transitions from rotations of rigid heteroanionic polyhedra" *J. Am. Chem. Soc.* **2016**, *138*, 11882.
8. Takenaka, K. "Negative thermal expansion materials: technological key for control of thermal expansion" *Sci Tech Adv Mat* **2012**, *13*, 013001.
9. Hu, L.; Chen, J.; Sanson, A.; Wu, H.; Rodriguez, C. G.; Olivi, L.; Ren, Y.; Fan, L.; Deng, J.; Xing, X. "New insights into the negative thermal expansion: direct experimental evidence for the 'guitar-string' effect in cubic ScF_3 " *J. Am. Chem. Soc.* **2016**, *138*, 8320.

10. Zhao, Y.; Weidner, D. J. "Thermal expansion of SrZrO₃ and BaZrO₃ perovskites" *Phys Chem Minerals* **1991**, *18*, 294.
11. Hornig, D. F. "The Vibrational Spectra of Molecules and Complex Ions in Crystals. I. General Theory" *J of Chem Phys* **1948**, *16*, 1063.
12. Tamm, I. "Über eine mögliche Art der Elektronenbindung an Kristalloberflächen" *Zeit. für Phys.* **1932**, *76*, 849.
13. Compaan, A.; Lee, M.; Trott, G. "Phonon populations by nanosecond-pulsed Raman scattering in Si" *Phys Rev B.* **1985** *32*, 6731.
14. Salje, E. K.; Rehmman, S.; Pobell, F.; Morris, D.; Knight, K. S.; Herrmannsdorfer, T.; Dove, M. T. "Crystal structure and paramagnetic behavior of ϵ -WO_{3-x}" *J Phys: Cond Matter* **1997**, *9*, 6563.
15. Friese, K.; Kanke, Y.; Fitch, A. N.; Grzechnik, A. "Isosymmetrical Phase Transition and Charge Ordering in the Mixed Valence Vanadate β -YbV₄O₈" *Chem Mater.* **2007**, *19*, 4882.
16. 8.37A ed.; Bruker Analytical X-ray Instruments, Inc.; Madison, WI, 2005.
17. Bruker (2001). *SADABS*. Bruker AXS Inc., Madison, Wisconsin, USA.
18. Altomare, A.; Burla, M. C.; Camalli, M.; Cascarano, G. L.; Giacovazzo, C.; Guagliardi, A.; Moliterni, A. G. G.; Polidori, G.; Spagna, R. "SIR97: a new tool for crystal structure determination and refinement" *J. Appl. Crystallogr.* **1999**, *32*, 115.
19. Farrugia, L. J. "WinGX suite for small-molecule single-crystal crystallography" *J. Appl. Crystallogr.* **1999**, *32*, 837.
20. Sheldrick, G. "A short history of SHELX" *Acta Crystallogr., Sect. A* **2008**, *64*, 112.

21. Rorabacher, D. B. "Statistical treatment for rejection of deviant values: critical values of Dixon's 'Q' parameter and related subrange ratios at the 95% confidence level" *Anal Chem*, **1981**, *63*, 139.

Chapter 6

1. Trimarchi, G.; Zhang, X.; Vermeer, M. J. D.; Cantwell, J.; Poepelmeier, K. R.; Zunger, A. "Emergence of a few distinct structures from a single formal structure type during high-throughput screening for stable compounds: the case of RbCuS and RbCuSe", *Phys. Rev. B*, **2015**, *92*, 165103.
2. Gautier, R.; Zhang, X.; Hu, L.; Yu, L.; Lin, Y.; Sunde, T. O. L.; Chon, D.; Poepelmeier, K. R.; Zunger, A. "Prediction and accelerated laboratory discovery of previously unknown 18-electron ABX compounds" *Nat Chem* **2015**, *7*, 308.
3. Vermeer, M. J. D.; Zhang, X.; Trimarchi, G.; Donakowski, M. D.; Chupas, P. J.; Poepelmeier, K. R.; Zunger, A. "Prediction and Synthesis of Strain Tolerant RbCuTe Crystals Based on Rotation of One-Dimensional Nano Ribbons within a Three-Dimensional Inorganic Network", *J. Am. Chem. Soc.*, **2015**, *137*, 11383.
4. 7.23A ed.; Bruker Analytical X-ray Instruments, Inc.; Madison, WI, **2005**.
5. Sheldrick, G. M.; Bruker Analytical X-ray Instruments, Inc.; Madison, WI, **1997**.
6. Sheldrick, G.M. XPREP Version 2008/2. Bruker AXS Inc., Madison, WI, **2008**.
7. Farrugia, L. J. "WinGX suite for small-molecule single-crystal crystallography" *J. Appl. Crystallogr.* **1999**, *32*, 837.

8. Sheldrick, G. M. SHELXL. *Acta Cryst.* **2005** C71, 3-8.
9. Bruker. SADABS. Bruker AXS Inc., Madison, Wisconsin, USA, **2001**.

Chapter 7

1. Darwin C.G. “The reflexion of x-rays from imperfect crystals”. *Phil. Mag.* **1922** 43, 800.
2. Azaroff, L. V. *Elements of X-ray Crystallography*. McGraw-Hill Book Company, New York, **1968**.
3. Speakman, S. A. *Introduction to high resolution x-ray diffraction of epitaxial thin films* [powerpoint slides]. Retrieved from <http://prism.mit.edu/xray>. Accessed March 12, 2018.
4. “Product Information: Advanced Thin film X-ray system-Grazing incidence in-plane diffractometer”. *The Rigaku Journal.* **1999**, 16, 53.
5. Yu, H.; Cantwell, J.; Wu, H.; Zhang, W.; Poeppelmeier, K. R.; Halasyamani, P. S. “Top-seeded solution crystal growth, morphology, optical and thermal properties of Ba₃(ZnB₅O₁₀)PO₄” *Cryst Growth Des* **2016**, 16, 3976.
6. Zhang, W.; Halasyamani, P. S. “Top-seeded solution crystal growth of noncentrosymmetric and polar Zn₂TeMoO₇ (ZTM)” *J Sol State Chem.* **2016**, 236, 32.
7. Wu, H.; Yu, H.; Zhang, W.; Cantwell, J.; Poeppelmeier, K. R.; Pan, S.; Halasyamani, P. S. “Top-seeded solution crystal growth and linear and nonlinear optical properties of Ba₄B₁₁O₂₀F” *Cryst Growth Des* **2017**, 17, 1404.

8. Zhang, W.; Yu, H.; Cantwell, J.; Wu, H.; Poeppelmeier, K. R.; Halasyamani, P. S. “LiNa₅Mo₉O₃₀: Crystal growth, linear, and nonlinear optical properties”. *Chem Mater.* **2016**, *28*, 4483.
9. Wu, H.; Yu, H.; Zhang, W.; Cantwell, J.; Poeppelmeier, K. R.; Pan, S.; Halasyamani, P. S. “Crystal growth and linear and nonlinear optical properties of KIO₃.Te(OH)₆” *Cryst Growth Des.* **2017**, *17*, 4405.
10. Zhao, P., Cong, H.; Tian, X.; Sun, Y.; Zhang, C.; Xia, S.; Gao, Z.; Tao, X. “Top-Seeded Solution Growth, Structure, Morphology, and Functional Properties of a New Polar Crystal — Cs₂TeW₃O₁₂”. *Cryst Gro & Des.* **2015**. *15*, 4484.
11. Jin, C.G.; Li, Z.; Huang, L. X.; He, M. Z. “Top-seeded solution growth and characterization of a novel nonlinear optical crystal MnTeMoO₆”. *J Cryst Growth*, **2013**. *369*, 43.
12. Yu, J.; Liu, L.; Wang, X.; Zhou, H.; He, X.; Zhang, C.; Zhou, W.; Chen, C. “Study on defects in hydrothermal-grown KBe₂BO₃F₂ crystals”. *J Cryst Growth*, **2011**. *318*. 621
13. Zhang, G.; Tao, X.; Ruan, H.; Wang, S.; Shi, Q. “Growth of CdSiP₂ single crystals by self-seeding vertical Bridgman method”. *J Cryst Growth*, **2012**. *340*, 197.
14. Zhang, J.; Zhang, Z.; Zhang, W.; Zhang, Q.; Sun, Y.; Zhang, C.; Tao, X. “Polymorphism of BaTeMo₂O₉: a new polar polymorph and the phase transformation”. *Chem Mater.* **2011**, *23*, 3752.
15. Zhang, J.; Tao, X.; Sun, Y.; Zhang, Z.; Zhang, C.; Gao, Z.; Xia, H.; Xia, S. “Top-Seeded Solution Growth, Morphology, and Properties of a Polar Crystal Cs₂TeMo₃O₁₂.” *Cryst Growth Des.* **2011**. *11*. 1863.

Appendix: Curriculum Vitae

Vita

May 2018

Jacqueline R. Cantwell
Doctoral Candidate

1570 Oak Avenue
Apt 714
Evanston, IL 60201

Tel: (678) 910-6379
jcantwell@u.northwestern.edu
cantwelljr@gmail.com

Education

Ph.D. in Chemistry – June 2018

Department of Chemistry, Northwestern University, Evanston, IL.
Field: Solid State and Materials. GPA: 3.44.

B.S. in Chemistry (ACS-certified degree) – May 2012

Department of Chemistry and Biochemistry, University of South Carolina, Columbia, SC. *Magna cum laude* with Honors from the South Carolina Honors College. French Minor. GPA: 3.85. May 2012.

Research Experiences

Graduate Research, Dr. K. Poeppelmeier, Dept. of Chemistry, Northwestern University. Solid state synthesis of noncentrosymmetric oxides and oxyfluorides for technology applications using hydrothermal synthesis.
December 2013 – present.

Fulbright Research Grant to France, Dr. Christine Martin, Laboratoire de Cristallographie et Sciences des Matériaux (CRISMAT), Ecole Nationale Supérieure d'Ingénieurs de Caen (ENSICAen), Caen, France. Researched multiferroic transition metal oxides using traditional solid state synthesis techniques as well as the optical floating zone method.
October 2012 – June 2013.

Undergraduate Research, Dr. H.-C. zur Loye, Dept. of Chemistry and Biochemistry, University of South Carolina. Synthesized novel rare earth-containing metal oxides using the hydroxide flux method. Characterized the structural and optical properties using powder x-ray diffraction, scanning electron microscopy, and fluorescence spectroscopy. Researched gallium and lithium oxides. Fall 2009 – May 2012.

Research Internship for Science and Engineering scholarship awarded by Deutscher Akademischer Austausch Dienst. Dr. Michael Tiemann, Dept. of Chemistry, Universität Paderborn, Paderborn, Germany. Researched novel multiferroic nanoporous materials using nanocasting method. Summer 2011.

Publications

- “Empirical and Theoretical Approaches to Understanding Hydrogen Bonding in $\text{CuVOF}_4(\text{H}_2\text{O})_7$ ”, J. Cantwell, H. Rosner, K. R. Poeppelmeier, *In Preparation*, (2018).
- “Synthesis, Structure, and Pleochroism of $\text{CuMnF}_5(\text{H}_2\text{O})_7$ ”, J. Cantwell, E. Vander Ende, R. Van Duyne, K. R. Poeppelmeier. *In Preparation*. (2018).
- “Crystal Structure and Properties of KNaMnF_5 ”, J. Cantwell, E. Vander Ende, R. Van Duyne, K. R. Poeppelmeier. *In Preparation*. (2018).
- “Crystal Growth and Linear and Nonlinear Optical Properties of $\text{KIO}_3 \cdot \text{Te}(\text{OH})_6$ ”, H. Wu, H. Yu, J. Cantwell, K. R. Poeppelmeier, S. Pan, and P. S. Halasyamani, *Cryst. Growth & Des.*, **17(8)**, 4405-4412 (2017).
- “Top-Seeded Solution Crystal Growth and Linear and Nonlinear Optical Properties of $\text{Ba}_4\text{B}_{11}\text{O}_{20}\text{F}$ ”, H. Wu, H. Yu, J. Cantwell, K. R. Poeppelmeier, S. Pan, and P. S. Halasyamani, *Cryst. Growth & Des.*, **17 (3)**, 1404-1410 (2017).
- “ $\text{LiNa}_5\text{Mo}_9\text{O}_{30}$: Crystal Growth, Linear, and Nonlinear Optical Properties”, W. Zhang, H. Yu, J. Cantwell, H. Wu, K. R. Poeppelmeier, and P. S. Halasyamani, *Chem. Mater.* **28 (12)**, 4483-4491 (2016).
- “Top-Seeded Solution Crystal Growth, Morphology, Optical and Thermal Properties of $\text{Ba}_3(\text{ZnB}_5\text{O}_{10})\text{PO}_4$ (BZBP)”, H. Yu, J. Cantwell, W. Zhang, K. R. Poeppelmeier, and P. S. Halasyamani, *Cryst. Growth & Des.*, **16 (7)**, 3976-3982 (2016).
- "Emergence of a few distinct structures from a single formal structure type during high-throughput screening for stable compounds: the case of RbCuS and RbCuSe ", G. Trimarchi, X. Zhang, M. J. D. Vermeer, J. Cantwell, K. R. Poeppelmeier, and A. Zunger, *Phys. Rev. B*, **92**, 165103 (2015).
- "Synthesis of Two Vanadium Oxide-Fluoride Materials that Differ in Phase Matchability", M.D. Donakowski, R. Gautier, H. Lu, T. T. Tran, J. R. Cantwell, P. S. Halasyamani, and K. R. Poeppelmeier, *Inorg. Chem.*, **54**, 765-772 (2015).
- “Crystal Growth and Optical Properties of Lithium Lanthanide Oxides: LiLnO_2 ($\text{Ln} = \text{Nd, Sm, Eu, Gd, and Dy}$)”. Jacqueline R. Cantwell, Irina P. Roof, Mark D. Smith and Hans-Conrad zur Loye. *Solid State Sciences.*, **13 (5)**, 1006-1012 (2011).

Presentations

“Structural Studies of Hydrogen Bonding in Transition Metal Oxide Fluorides”. Oral presentation at IMRC 2017, Cancun, Mexico.

“Cristallogenèse d'oxydes à base de lithium et de lanthanides LiLnO_2 ($\text{Ln} = \text{Nd}, \text{Sm}, \text{Eu}, \text{Gd}, \text{et Dy}$)”. Poster presented at CRISTECH 2012, Carry Le Rouet, France.

Honors and Awards

Iota Sigma Pi National Honor Society for Women in Chemistry, inducted 2018

Phi Lambda Upsilon Honorary Chemical Society, inducted 2015

National Science Foundation Graduate Research Fellowship Honorable Mention, 2012, 2014, 2015

US Fulbright Student Study/Research Grant Fellow, 2012

South Carolina Section of the American Chemical Society Outstanding Undergraduate Award, 2012

Phi Beta Kappa National Honor Society, inducted 2011

Organizations

Women in Science and Engineering Research

Member of a graduate student organization aimed at supporting women in across scientific disciplines through providing networking events, mentorship relationships, and professional development opportunities. September 2013 – present.

American Chemical Society

Student member, Inorganic Chemistry Division. December 2010 – present.

Teaching Experience

General Chemistry – Chem 121, 122, 123-CN, 141

Fall 2013, Winter 2013, Spring 2016, Winter 2018

Led weekly lab sessions for ~30 students each quarter, graded lab reports and term papers, offered weekly office hours, proctored quizzes and exams for the lecture courses.

Advanced Laboratory – Chem 350

Winter 2013, Winter 2014

Led upperclassmen undergraduate students in inorganic synthesis experiments on MOFs/zeolites and on superconductors; designed and graded final report for project

Inorganic Chemistry – Chem 333

Fall 2014, Fall 2015

Teaching assistant for undergraduate inorganic lecture course; led problem solving sessions during office hours and review sessions; wrote and graded weekly quizzes, two midterms, and final exam, made and updated website on course management system

Science Outreach**Science in the Classroom**

Volunteers as a science leader for monthly in-class experiments at a local elementary school. This program is designed and run entirely by Northwestern Chemistry graduate students in order to inspire a love of chemistry in a younger generation. 2013 – present.

Carolina Science Outreach

Presented on current scientific topics of interest to both adult and young audiences to promote scientific awareness in the general public. Organized poster session to introduce local teachers to the group's offerings and analyzed feedback to develop new presentations to fit school curricula. 2010-2012.

Science Fair Judge

Volunteers as a judge for a variety of local science fairs for students from elementary, middle, and high school, including fairs from the school level up to the city-wide Chicago Science Fair. 2013 – present.